UNIVERSIDAD NACIONAL AUTÓNOMA DE MÉXICO

POSGRADO EN CIENCIAS FÍSICAS
INSTITUTO DE FÍSICA
FÍSICA CUÁNTICA ATÓMICA Y MOLECULAR

Pattern formation in Bose-Einstein condensates: collective excitations and parametric modulation

TESIS
QUE PARA OPTAR POR EL GRADO DE:
DOCTORA EN CIENCIAS FÍSICA

PRESENTA:

Alejandra del Río Lima

TUTOR PRINCIPAL
Dr. Freddy Jackson Poveda Cuevas
Instituto de Física

MIEMBROS DEL COMITÉ TUTOR
Dra. Rocío Jáuregui Renaud
Instituto de Física

Dra. Rosario Paredes Gutiérrez
Instituto de Física

Ciudad Universitaria, CD. MX., abril de 2025

PROTESTA UNIVERSITARIA DE INTEGRIDAD Y HONESTIDAD ACADÉMICA Y PROFESIONAL
(Graduación con trabajo escrito)

De conformidad con lo dispuesto en los artículos 87, fracción V, del Estatuto General, 68, primer párrafo, del Reglamento General de Estudios Universitarios y 26, fracción I, y 35 del Reglamento General de Exámenes, me comprometo en todo tiempo a honrar a la Institución y a cumplir con los principios establecidos en el Código de Ética de la Universidad Nacional Autónoma de México, especialmente con los de integridad y honestidad académica.

De acuerdo con lo anterior, manifiesto que el trabajo escrito titulado:

Pattern formation in Bose-Einstein condensates:
collective excitations and parametric modulation

que presenté para obtener el grado de ----Doctorado---- es original, de mi autoría y lo realicé con el rigor metodológico exigido por mi programa de posgrado, citando las fuentes de ideas, textos, imágenes, gráficos u otro tipo de obras empleadas para su desarrollo.

En consecuencia, acepto que la falta de cumplimiento de las disposiciones reglamentarias y normativas de la Universidad, en particular las ya referidas en el Código de Ética, llevará a la nulidad de los actos de carácter académico administrativo del proceso de graduación.

Atentamente

Alejandra del Río Lima
Número de cuenta 311228782

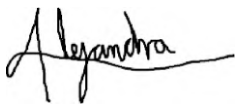

(Nombre, firma y Número de cuenta de la persona alumna)

COORDINACIÓN GENERAL DE ESTUDIOS DE POSGRADO

CARTA AVAL PARA DAR INICIO A LOS TRÁMITES DE GRADUACIÓN

Universidad Nacional Autónoma de México
Secretaría General
Coordinación General de Estudios de Posgrado

Dr. Alberto Güijosa Hidalgo
Programa de Posgrado en Ciencias Físicas
Presente

Quien suscribe, **Dr. Freddy Jackson Poveda Cuevas**, tutor(a) principal de **Alejandra del Río Lima**, con número de cuenta **311228782**, integrante del alumnado de **Doctorado en Ciencias (Física)** de ese programa, manifiesto bajo protesta de decir verdad que conozco el trabajo escrito de graduación elaborado por dicha persona, cuyo título es:

Pattern formation in Bose-Einstein condensates: collective excitations and parametric modulation

, así como el reporte que contiene el resultado emitido por la herramienta tecnológica de identificación de coincidencias y similitudes con la que se analizó ese trabajo, para la prevención de faltas de integridad académica.

De esta manera, con fundamento en lo previsto por los artículos 96, fracción III del Estatuto General de la UNAM; 21, primero y segundo párrafos, 32, 33 y 34 del Reglamento General de Exámenes y; 22, 49, primer párrafo y 52, fracción II del Reglamento General de Estudios de Posgrado, **AVALO** que el trabajo de graduación presentado se envíe al jurado para su revisión y emisión de votos, por considerar que cumple con las exigencias de rigurosidad académica previstas en la legislación universitaria.

Protesto lo necesario,

Ciudad Universitaria, Cd. Mx., a 21 de abril de 2025

Dr. Freddy Jackson Poveda Cuevas

Tutor(a) principal

Agradecimientos

Este trabajo doctoral recibió financiamiento de la UNAM y del SECIHTI (CONAHCyT) a través de diferentes proyectos. Por lo tanto, agradezco al SECIHTI por la beca doctoral No. 868202 que recibí durante este periodo y por el financiamiento recibido a través de los proyectos No. A1-S-39242 y No. CF-2023-I-72. Asimismo, agradezco a la UNAM por el financiamiento otorgado a través del proyecto DGAPA-UNAM-PAPIIT No. IN109021.

Para comenzar los agradecimientos personales, quisiera iniciar asegurando que las palabras escritas aquí no logran representar correctamente lo afortunada y agradecida que me siento con ustedes por el tiempo, apoyo, cariño, experiencias, vivencias y aprendizajes que me llevo de este periodo. Quizá lo más cercano a la realidad es que, sin ustedes, esta tesis no podría haber sido y tampoco tendría sentido, ya que este trabajo es el resultado de diferentes aportaciones, tanto académicas como no académicas.

Comenzaré agradeciendo mucho y con mucho cariño a Jackson por haberme permitido iniciar el doctorado. Por su indudable apoyo en cualquier momento, por su empatía, comprensión, amistad, sinceridad, pasión y empeño al hacer las cosas. Por sus enseñanzas de la física y de la vida. Siempre estaré agradecida contigo.

Agradezco mucho y con mucho cariño a mi mamá y hermano que siempre están dispuestos a ayudar y a escuchar. Muchas gracias por estar conmigo y apoyarme. Gracias por alentarme a seguir y por calmarme cuando no veo con claridad.

Agradezco a mi papá por todas las enseñanzas y palabras de aliento que perduran con el paso de los años. De alguna forma, a través de ellas, siempre estarás cerca.

Agradezco al LMU, a Jorge y a todos los integrantes del lab con los que pude convivir y aprender: Diego, Lalo, Sebastián, Viani, Patricio, Juan Pablo, Fer, Natalia y José Luis. Aunque con algunos conviví más que con otros, definitivamente con todos hubo risas y, al menos, un láser que anclar (a cada rato).

Agradezco a los técnicos académicos Carlos Gardea, Rodrigo Gutiérrez y Maira Pérez por su apoyo y ayuda en los experimentos en los que participé.

Agradezco al Opto-Atomic group por las tardes de convivencia y reuniones eternas en la biblioteca.

Agradezco a mi comité tutor: a la Dra. Rocío Jáuregui y a la Dra. Rosario Paredes. Muchas gracias por sus revisiones, consejos y reuniones. Agradezco haber podido aprender de ustedes. Son un gran ejemplo para mí, como mujeres y como físicas.

Agradezco mucho a todos mis sinodales, Dr. Eduardo Ibarra, Dr. Francisco Soto, Dr. Ricardo Méndez, Dra. Rosario Paredes y Dr. Santiago Caballero, por tomarse el tiempo de revisar esta tesis y de reunirse conmigo. Sus aportaciones enriquecieron este trabajo y me ayudaron a concluirlo.

Resumen

Entender los fenómenos observados en los sistemas cuánticos de muchos cuerpos resulta aún un desafío fundamental con intereses en la investigación básica, así como en aplicaciones tecnológicas. Existen preguntas abiertas relacionadas con estos sistemas. Por ejemplo, la prueba de la existencia de un condensado de Bose-Einstein (BEC) en presencia de interacciones, el entendimiento del mecanismo asociado a la superconductividad y la superfluidez en gases cuánticos son fenómenos que aún no tienen una explicación satisfactoria.

Las excitaciones colectivas, las cuales describen el movimiento correlacionado de partículas interactuantes, son una herramienta importante para acceder al entendimiento de los sistemas de muchos cuerpos. Por ejemplo, como consecuencia de estas excitaciones, se ha observado la formación de patrones característicos sobre la densidad de gases cuánticos, como lo son los condensados de Bose-Einstein y los gases de Fermi degenerados.

El estudio de la formación de patrones es de interés, ya que ocurren en distintos sistemas físicos y biológicos. En los fluidos cuánticos, existe un alto grado de control en los parámetros del sistema, como en la geometría del potencial de confinamiento y la intensidad de interacción. Esto posibilita la creación de diversas configuraciones para un sistema de interés. Por lo tanto, un campo de estudio actual es la creación de patrones en sistemas cuánticos con diferentes configuraciones, lo que resulta en la observación de patrones con diferentes simetrías.

Dentro de este marco, la tesis doctoral se centra en la creación de patrones en condensados de Bose-Einstein encerrados en potenciales externos con geometrías oblata y prolata. El mecanismo de excitacion considerado es la modulacion paramétrica. Esta puede ser introducida mediante las frecuencias de la trampa exterior o mediante la intensidad de la interacción atómica. La modulación de la frecuencia axial en las trampas oblatas y la frecuencia radial en las trampas prolatas producen patrones de densidad similares a las ondas de Faraday en un fluido convencional, las cuales se distinguen por su comportamiento oscilatorio con la mitad de la frecuencia de excitación. Estas observaciones ofrecen información sobre las interacciones entre los átomos, la disipación de energía y la estabilidad del sistema.

En resumen, la tesis doctoral ayuda a comprender la formación de patrones en la densidad de condensados de Bose-Einstein. Además, resulta interesante para investigaciones futuras en dinámica no lineal y comportamientos emergentes en gases cuánticos ultrafríos.

Abstract

Understanding the phenomena observed in many-body quantum systems remains a fundamental challenge with interests in both basic research and technological applications. Open questions persist regarding these systems. For instance, proving the existence of a Bose-Einstein Condensate (BEC) in the presence of interactions, and comprehending the mechanisms associated with superconductivity and superfluidity in quantum gases, are phenomena that still lack a satisfactory explanation.

Collective excitations, which describe the correlated motion of interacting particles, are an important tool for gaining insight into many-body systems. For example, as a consequence of these excitations, the formation of characteristic patterns on the density of quantum gases, such as Bose-Einstein condensates and degenerate Fermi gases, has been observed.

The study of pattern formation is of interest because it occurs in diverse physical and biological systems. In quantum fluids, there's a high degree of control over system parameters, such as the geometry of the confinement potential and the interaction strength. This allows for the creation of various configurations for a system of interest. Therefore, a current field of study is the creation of patterns in quantum systems with different configurations, resulting in the observation of patterns with varying symmetries.

Within this framework, this doctoral thesis focuses on the creation of patterns in Bose-Einstein condensates confined in external potentials with oblate and prolate geometries. The excitation mechanism considered is parametric modulation. This can be introduced either through the frequencies of the external trap or through the atomic interaction strength. Modulating the axial frequency in oblate traps and the radial frequency in prolate traps produces density patterns similar to Faraday waves in a conventional fluid. These are distinguished by their oscillatory behavior at half the excitation frequency. These observations offer insights into interatomic interactions, energy dissipation, and system stability.

In summary, this doctoral thesis contributes to understanding pattern formation in the density of Bose-Einstein condensates. Furthermore, it holds interest for future research in nonlinear dynamics and emergent behaviors in ultracold quantum gases.

Contents

Introduction

The challenge of understanding quantum many-body systems has become a problem of general relevance since it finds technological applications and fundamental basic research interests. For example, there are some unsolved problems regarding many-body systems, such as the proof of the existence of a Bose-Einstein condensate in the presence of interactions [1], the understanding of the mechanism that causes superconductivity at temperatures higher than 25 K [2], and the analog mechanism that generates superfluidity [3]. Also, understanding some universal behaviors, such as the liquid crystal phase transition and the unitary regime, is still missing.

In this sense, collective excitations are important in understanding many-body systems since they describe correlated motion among multiple constituents of a system, which result in emergent phenomena that cannot be understood by considering individual particles. For example, the coordinate movement of many interacting particles leads to large-scale pattern formation, where structured arrangements emerge spontaneously.

Pattern formation is a phenomenon observed across different scales in natural systems. It occurs in diverse domains such as biological and chemical systems, condensed matter physics, hydrodynamics, and nonlinear optics, among others [4–6]. In physics, the study of pattern formation has been present in understanding non-equilibrium processes, such as those occurring during phase transitions and within the framework of nonlinear dynamics. Many mechanical systems change from simple to complex behavior in response to modifications in their control parameters and thus to a continuously injected energy that often results in a complex pattern formation. In this sense, nonlinear dynamics theory allows a better comprehension of biological and chemical systems by simulating them with analog physical systems with a simpler structure [7].

Spatial and temporal patterns arise when a homogeneous system is driven into an unstable regime, wherein infinitesimally small perturbations can induce significant deformations. Thus, in-

stability is at the center of understanding pattern formation. Some of the most well-known instabilities in fluid dynamics include Rayleigh-Benard convection [8], Taylor-Couette flow [9], and parametric excitations [10]. The latter has been extensively investigated, particularly in classical fluids subjected to a single mode of parametric excitation. In this single mode case and within the linear regime, such systems are commonly described by the Mathieu equation [11, 12]. However, beyond the linear approximation, the analysis becomes substantially more complex due to the inherent hydrodynamic nonlinearity, and the mechanisms through which these instabilities transition into chaotic dynamics and turbulence remain an open question.

The experimental realization and theoretical modeling of quantum fluids have opened a new path for investigating pattern formation, offering the advantage of precise control over system parameters. In classical fluids, spatial boundary conditions are dictated by the geometry of the container, while viscosity significantly influences pattern development [13–17]. In contrast, quantum fluids composed of ultracold atomic gases allow for external control of confinement geometry via optical or magneto-optical trapping potentials [18]. Furthermore, the conservative interaction strength between the atoms can be modified via Feshbach resonances [19–21], which will be discussed in Chapter 1.

A mechanism to generate patterns in quantum fluids is the excitation of the collective modes. For example, in harmonically trapped quantum gases, the quasi-stationary collective modes, which are characterized by changes in the sample's position, orientation, or shape with no significant variation in volume, are classified as surface modes. These excitations have been employed to probe the transition from hydrodynamic to collisionless regimes in ultracold atomic gases [22–24]. Conversely, oscillations involving substantial changes in volume, and consequently in fluid density, are classified as compression or breathing modes [25–27].

Due to the importance of this area, in the last years, various forms of parametric modulation have been applied to different types of quantum fluids, allowing the study of emergent density patterns [28–34]. For example, nonlinear parametric excitations known as Faraday waves were first observed in a weakly interacting Bose-Einstein condensate (BEC) of ^{87}Rb confined in a cigar-shaped trap [35], as well as in a ^{23}Na BEC [36]. These patterns were later shown to transition into a granulated regime in a ^{7}Li BEC [37].

Currently, various studies on pattern formation in quantum gases have been conducted under different conditions, yielding diverse pattern observations. For instance, Fujii et al. demonstrated

that the suppression of boundary can reproduce dynamics similar to an infinitely extended system, leading to the spontaneous formation of a square lattice in a two-dimensional BEC subject to absorptive boundary conditions [38, 39]. Similarly, Kwon et al. observed the formation of star-shaped density patterns in a pancake-shaped BEC when the scattering length is modulated at frequencies resonant with the radial trap confinement [40]. Additionally, pattern formation has been generated in a strongly superfluid of ^{6}Li via parametric modulation of the radial trapping frequency [41], creating a fringe pattern. Thus, the high degree of control in quantum fluids permits the generation of distinct pattern types depending on the geometry of the system and on the nature and frequency of the external excitation.

Therefore, it has been shown that the geometry of the trapping potential, the specific form of parametric excitation, and the modulation frequency are all important factors influencing the formation, evolution, and stability of patterns in quantum fluids. Moreover, the high degree of control over the parameters of quantum fluids makes these systems particularly interesting and rich, offering the possibility of generating different parameters depending on the system's conditions.

Among the various excitation schemes, a distinct pattern emerges when the system is modulated precisely at the breathing mode frequency of the atomic cloud, leading to a pronounced oscillatory behavior. These spatio-temporal structures are referred to as Faraday waves, drawing an analogy with classical systems originally described by Michael Faraday [42], where waves emerge in the plane perpendicular to the modulation direction, and the pattern frequency corresponds to half that of the driving frequency [13].

Despite the various works in this area, an explanation for the emergence of density patterns is still lacking.

In this context, this work is framed among the last type of excitation scheme discussed, i.e., a modulation with exactly the breathing mode frequency of the atomic cloud. A set of numerical simulations was conducted for a molecular Bose-Einstein condensate that resembles the experimental system at the *Laboratorio de Materia Ultrafría* (LMU) of the *Instituto de Física* at the *Universidad Nacional Autónoma de México* (UNAM). Thus, the considered system is a Fermi gas of ^{6}Li, which pairs to form diatomic and bosonic molecules that can be cooled to generate a molecular Bose-Einstein condensate (BEC). The experimental details are provided in Chapter 3. The presence of a Feshbach resonance enables the interaction between particles to be modified. Thus, it is possible

to study the Fermi gas in three different interacting regimes: BEC, BCS, and the unitary regime. However, it is essential to clarify that this work only considers the BEC limit, where the Gross-Pitaevskii equation, as a mean-field approach to the system, is suitable for description.

To delimit the geometry of the system and to resemble the experiments of the LMU, an atomic cloud confined in a pancake-shaped and a cigar-shaped trap is considered. This selection enables the study of the role of dimensionality in the system, as both selected geometries are characterized by a direction of greater confinement, suggesting that a 2D system may be suitable for description. However, this work maintains the analysis in a 3D space and explains why this approach is appropriate.

The considered excitation mechanism is a parametric modulation that can be introduced through one of the trap frequencies or the scattering length. When the modulation is introduced through the trap, then the axial frequency is modulated for the pancake-shaped configuration, and the radial trap is modulated for the cigar-shaped geometry.

This work was motivated by the results reported in reference [41], where the experimental observation of Faraday Waves in a cigar-shaped molecular BEC at the LMU was reported. Giving continuity to the initial work, the results and analysis obtained through this thesis aim to serve as a guide for future experimental realizations at the LMU in various geometries and parametric modulation schemes. The complete and detailed analysis of the results can be found in reference [43]. Furthermore, complementary work realized during the PhD is cited in references [44] and [45] and will be briefly discussed in Chapter 6.

The discussion of the work and results presented in this thesis is structured as follows:

- Chapter 1 begins with a theoretical description of a Bose-Einstein Condensate (BEC) and the effective interactions between the particles.

- Chapter 2 discusses how interactions give rise to collective excitations, which can be studied within a hydrodynamic frame or through the variational method for fields. This chapter presents analytical and numerical results obtained through the variational method for the collective excitations of a BEC in different spatial configurations and coordinates.

- Chapter 3 presents the collective modes observed experimentally for a molecular BEC of ^{6}Li pairing atoms. Also, it briefly discusses the experimental setup needed to generate a degenerate Fermi gas and a molecular BEC.

- Chapter 4 shows how the excitation of particular collective modes generates a pattern over the BEC density. These results are obtained through a numerical simulation of the Gross-Pitaevskii equation. The external potential determines the symmetry of the generated patterns, which gives insight into the dissipation of the introduced energy and, thus, the system's stability.

- Chapter 5 gives further discussion about the extension of the problem and the conclusions of the work.

- Chapter 6 gives a resume of other work realized during the PhD period but not related to the problem studied in this thesis.

Chapter 1

Theoretical Description of a BEC

1.1 Overview

Bose-Einstein condensation is a quantum phenomenon that occurs in a system of N bosons at extremely low temperatures, approaching absolute zero, where a macroscopic number of particles occupy the lowest energy state. This matter phase was predicted to exist in the absence of interactions by Nath Bose and Albert Einstein, and their study was developed in the frame of statistical mechanics.

Due to the advancement of laser technology, which enabled the experimental realization of a Bose-Einstein condensate (BEC), it is now known that interactions are crucial in the rethermalization process that allows a condensate to be achieved from an atomic gas, enabling it to reach the critical temperature. Additionally, interactions are responsible for introducing other quantum phenomena, including superfluidity, coherence, and collective modes.

Since the objective of this thesis is to comprehend the arising of patterns over the density of an interacting molecular Bose-Einstein condensate, as previously stated in the Introduction, this chapter presents the basis for understanding the theoretical frame that describes the BEC limit of a Fermi gas, the interactions present on the system, and how they can be modulated through the mechanism of Feshbach resonances.

This chapter begins with a brief discussion of an ideal BEC (without interactions), within the framework of statistical thermodynamics. Then, effective interactions, considered as contact interactions, are introduced as the main contribution for dilute and low-energy systems. Lately, these effective interactions are taken into account in a mean-field approximation that allows the construction of the Gross-Pitaevskii-equations, which is the equation of motion describing a BEC. Finally, Feshbach resonances are discussed as a mechanism for understanding the BEC-BCS crossover, which

allows the condensation of a Fermi gas through the formation of bosonic diatomic molecules.

1.2 Ideal Bose-Einstein Condensate

For a system of non-interacting bosons, the occupation number of a quantum state with energy ϵ is given by the Bose-Einstein distribution:

$$n(\epsilon) = \frac{1}{\exp\left[\frac{\epsilon-\mu}{k_B T}\right] - 1}, \tag{1.1}$$

where μ is the chemical potential, k_B is the Boltzmann constant and T is the temperature..

As T approaches zero, the lowest energy level becomes macroscopically occupied, and the chemical potential goes to lower negative values. When a zero chemical potential is reached, $\mu = 0$, the system undergoes a phase transition: a Bose-Einstein condensate arises. Since all the bosons in a BEC are in the same single quantum state, the complete system can be described by a single wave function. As it will be discussed in Section (1.4), this macroscopic wave function characterizing a condensate follows the mean-field Gross-Pitaevskii equation, which is valid for a dilute and weakly-interacting gas.

The critical temperature T_c at which the phase transition occurs depends on the external potential that confines the particles. For a harmonic trap, commonly used in ultracold experiments, the temperature at which the BEC arises is given by,

$$T_c = \frac{\hbar\bar{\omega}}{k_B}\left(\frac{N}{\zeta(3)}\right)^{1/3}, \tag{1.2}$$

where $\bar{\omega}$ is the geometric mean of the trap frequencies and $\zeta(3) \approx 1.202$ is the Riemann zeta function.

Below T_c, the fraction of particles in the ground state is given by:

$$\frac{N_0}{N} = 1 - \left(\frac{T}{T_c}\right)^3, \tag{1.3}$$

where N_0 is the number of particles in the ground state.

In summary, Bose-Einstein condensation in a non-interacting gas arises purely from quantum statistical effects without the need for interactions. The transition occurs at a well-defined critical temperature, below which a macroscopic fraction of bosons occupy the ground state. It is important to add that the critical temperature at which the condensation is reached depends on the characteristics of the external potential. Since most experiments use a harmonic trap, this text presents only this case.

1.3 Effective interactions

Collisional phenomena, which are the scattering of particles, are at the center of all the interactions in physics. These collisional phenomena could be treated in a classical or quantum approach. In order to determine which behavior describes the best the system, it is important to define some characteristic lengths:

- Interaction range r_0: defines the distant for which for values $r > r_0$, the interaction between particles can be neglected.
- Interatomic space $n_0^{-1/3}$: gives the average distance between the particles of the system with density n_0.
- System size $V^{1/3}$: is related to the volume in which the system is confined.

In general, atomic physics experiments are developed in the condition $r_0 \ll n_0^{-1/3} \ll V^{1/3}$. The classical and quantum regimes can be defined by comparing the characteristic lengths with the thermal wavelength [46, 47], which is defined as:

$$\Lambda = \sqrt{\frac{2\pi\hbar^2}{mk_BT}}. \tag{1.4}$$

Depending on the comparison, it is possible to define different cases:

- When the thermal wavelength is much less than the interaction range, $\Lambda \ll r_0$, which can also be represented as $k\,r_0 \gg 1$ with $k \sim 1/\Lambda$, the wave behavior of the particles is not representative in the interaction. Thus, this regime is defined as the **quasi-classical collisions**.
- When the thermal wavelength is greater than the interaction range, $\Lambda \gg r_0 \rightarrow k\,r_0 \ll 1$, the wave behavior of the particles predominates in all the distance for which the interaction is defined. Thus, the correct description is by quantum mechanics, and this regime is known as a **quantum gas**.
- If in a quantum gas, the thermal wavelength is of the order of the interparticle spacing, $n_0\Lambda^3 \gg 1$, the gas formed by the ultracold collisions is called to be a **quantum degenerate gas**.

Besides the different classical o quantum regimes that can be defined through the comparison of the characteristic lengths, it is also possible to classify the system as a **dilute gas** if it satisfies the $n_0\, r_0^3 \ll 1$ condition, which means that the interparticle distance is much greater than the interaction range. In this case, the interaction between particles is mostly dominated by binary interactions since the contribution of three-body or higher-order interactions is less probable. This condition is important to be defined since the ultracold experiments realized happen to satisfy the condition of a dilute gas.

Now that the different classifications of the system have been set, it is time to discuss how the interactions are studied. As always, the description of the system is obtained by solving the Schrödinger equation. Since central potentials give interactions between particles, it is possible to separate the angular variables described by Spherical Harmonic functions and just solve for the radial equation,

$$\chi_\ell''(\mathbf{r}) + [\varepsilon - U_{eff}(r)]\, \chi_\ell = 0, \tag{1.5}$$

with $\chi(r) = rR_\ell(r)$ and $\varepsilon = \frac{2\mu E}{\hbar^2}$. In general, the interaction of atoms through a central potential is given by,

$$U_{eff}(\mathbf{r}) = U(\mathbf{r}) + \frac{\ell(\ell+1)}{r^2},$$

where the second term is the centrifugal barrier, which acts like a repulsive barrier that particles with higher angular momentum must overcome to reach the inner, attractive (or repulsive) part of the potential. For a given energy E, as l increases, the centrifugal barrier becomes higher and wider. At very low energies, as is the case for ultracold systems [48, 49], the kinetic energy of the particles is so small that they do not have enough energy to overcome the centrifugal barrier for $l > 0$. Only particles with $l = 0$ (s-wave) can effectively penetrate the potential and interact. The centrifugal barrier for $l = 0$ is zero, so there is no classical barrier to overcome. Thus, it is said that in many cases, s-wave collision ($\ell = 0$) dominates the interactions in ultracold systems.

The solution to equation (1.5) for indistinguishable particles is given by

$$\psi = \left[\mathrm{e}^{\imath kz} \pm \mathrm{e}^{-\imath kz}\right] + [f(\theta) \pm f(\pi - \theta)]\, \frac{\mathrm{e}^{\imath kr}}{r}, \tag{1.6}$$

where the first term represents an incoming plane wave in the z direction, while the second term is the scattered wave [49]. The plus sign applies to bosons so that the total wave function remains symmetric under the interchange of two variables. Similar, the minus sign applies to fermions for

considering an anti-symmetric wave function. In solution (1.6), k is the wave vector of the scattered wave, $f(k)$ is the scattering amplitude, and it is assumed that the potential vanishes at $r \to \infty$.

The scattering amplitude and the scattering cross section $\sigma(k)$ are related through the relation,

$$\sigma(\mathbf{k}) = \int |f(\mathbf{k})|^2 \, d\Omega. \tag{1.7}$$

Furthermore, if the interaction has spherical symmetry, the scattering amplitude can be written in terms of the scattering angle θ,

$$f(\theta) = \frac{1}{2\imath k} \sum_{\ell=0}^{\infty} (2\ell + 1)(\mathrm{e}^{\imath 2\delta_\ell} - 1) P_\ell(\cos\theta), \tag{1.8}$$

where P_ℓ are Legendre polynomials and $\ell = 0, 1, 2, \cdots$ denotes the contribution of the partial waves $s, p, d, \cdots$ to the total scattering length. For each partial wave, there is a phase shift δ_ℓ associated.

After substituting expression (1.8) in (1.7) and integrating over half the angular variables, $0 \leq \theta \leq \pi/2$ and $0 \leq \phi \leq \pi$, it is found,

$$\sigma(k, \delta_l) = \frac{8\pi}{k^2} \sum_{\ell=0}^{\infty} (2\ell + 1) \sin^2 \delta_\ell. \tag{1.9}$$

As a restriction of considering indistinguishable particles, only even-ℓ partial waves contribute to the total scattering cross section for a system of N-bosons. For fermions, only odd-ℓ partial waves contribute and due to the Pauli Exclusion Principle, for achieving interactions of s partial waves a spin mixture is needed, so that the indistinguishable property is lost (particles are in different states). The restriction in these contributions arises since the scattering cross section $\sigma(\theta)$ is defined in terms of the scattering amplitude $f(\theta)$, which makes part of the scattered wave function. Thus, the last expression of σ inherits the properties of the parity of the wavefunction. The symmetry of σ is assured when considering odd terms for ℓ, and the anti-symmetry behavior is guaranteed with the even terms for ℓ.

At low energies, the scattering cross section for bosons is dominated by the contribution with $\ell = 0$, thus (1.9) is simplified to just one term,

$$\sigma = \frac{8\pi}{k^2} \sin^2 \delta.$$

It is useful to rewrite the phase shift in terms of an s-wave scattering length a_s. The relation between them is given by,

$$k \cot \delta = -\frac{1}{a_s} + \frac{1}{2} r_0 k^2 + O(k^4),$$

where r_0 is the range interaction defined previously. Considering this relation, it is possible to express the scattering cross-section in terms of a_s, as:

$$\sigma = \frac{8\pi a_s^2}{1 + k^2 a_s^2}. \tag{1.10}$$

This relation has two important limits. For $ka_s \ll 1$, the scattering cross-section is $8\pi a_s^2$, which is equivalent to scattering obtained for a hard sphere of radius a_s. In contrast, when $ka_s \gg 1$, the scattering cross-section reaches the unitary limit, where $\sigma = 8\pi/k^2$. Thus, in the unitary limit, σ is independent of a_s.

As it will be discussed in section 1.5, the magnitude and sign of the scattering length a_s can be modulated through an external magnetic field. Therefore, experimentally, it is possible to visit different interaction regimens that are characterized by different relevant length scales. However, in this section, of special importance is the regime where the condition $ka_s \ll 1$ is satisfied and particles interact as if they were hard spheres. Due to this result, it is possible to propose an effective potential that describes interactions as contact interactions. In this sense, two interacting particles with radius a_s, mass m, and coordinates $\mathbf{r}$ and $\mathbf{r}'$ collide through the effective potential,

$$U(\mathbf{r} - \mathbf{r}') = \frac{4\pi\hbar^2 a_s}{m}\delta(\mathbf{r} - \mathbf{r}'), \tag{1.11}$$

where the constant

$$U_0 = 4\pi\hbar^2 a_s/m \tag{1.12}$$

can be defined. Therefore, in the $ka_s \ll 1$ regime and at very low energies, the interaction is a constant, which in the momentum representation is given by the value of U_0.

1.4 Gross-Pitaevskii Equation

The general Hamiltonian of a system of N-interacting bosons confined in an external potential V_{ext} is given by,

$$\hat{H} = \sum_{i=1}^{N}\left[-\frac{\hbar^2}{2m}\nabla_i^2 + V_{\text{ext}}(\mathbf{r}_i)\right] + \frac{1}{2}\sum_{i,j=1}^{N}\hat{V}\left(|\mathbf{r}_i - \mathbf{r}_j|\right), \tag{1.13}$$

where $\hat{V}\left(|\mathbf{r}_i - \mathbf{r}_j|\right)$ is the interacting potential, without any specifications, between two bosons. Due to the nature of the system, the wave function of the N-bosons, $\psi\left(\mathbf{r}_1, \mathbf{r}_2, \cdots, \mathbf{r}_N\right)$, needs to be symmetric under the interchange of two coordinates of the particles. This can be achieved by

writing $\psi(\mathbf{r}_1, \mathbf{r}_2, \cdots, \mathbf{r}_N)$ as a permanent constructed in a basis of N single particle wavefunctions $\{\phi_i(\mathbf{r}_i)\} = \{\phi_1(\mathbf{r}_1), \phi_2(\mathbf{r}_2), \cdots, \phi_N(\mathbf{r}_N)\}$. The permanent function also assures the consideration of the indistinguishable character of fundamental particles so that all the possible combinations of the states ϕ_i are considered in a symmetric wave function.

Solving for each ϕ_i by substituting the total wave function $\psi(\mathbf{r}_1, \mathbf{r}_2, \cdots, \mathbf{r}_N)$ into Hamiltonian (1.13) is not easy work, and the details of the problem would depend on the definition of the interacting potential $\hat{V}(|\mathbf{r}_i - \mathbf{r}_j|)$. However, for the description of a Bose-Einstein condensate, there is no need to seek for N single-particle wave functions since in a BEC, all the bosons occupy the same state, which will be denoted as $\phi(\mathbf{r}_i)$.

Therefore, the wave function of the condensed system can be written as a symmetrized product of the same single-particle wave function:

$$\psi(\mathbf{r}_1, \mathbf{r}_2, \cdots, \mathbf{r}_N) = \prod_{i=1}^{N} \phi(\mathbf{r}_i), \tag{1.14}$$

where the function $\phi(\mathbf{r}_i)$ satisfies the normalization condition,

$$\int d\mathbf{r}\, |\phi(\mathbf{r})|^2 = 1.$$

Wave function (1.14) is a mean-field approximation since it considers that for one particle, all the rest have the same status as they all are in the same independent state ϕ. Also, ψ is understood as a classic function describing a macroscopic field. Until now, a form for the complete wave function has been proposed, but the identity of $\phi(\mathbf{r})$ is still unknown. To solve the complete problem, the variational principle will be used, as an analytic solution cannot be obtained due to the coupling between particles introduced by the interacting potential.

The state of the Bose-Einstein condensate is the ground state of the N boson system. Thus, the state that minimizes the energy is the one associated with the ground state. However, in practice, only the true minimal ground energy is gained when the true ground state is known. The energy functional is defined by,

$$E \equiv \frac{\langle\psi|\hat{H}|\psi\rangle}{\langle\psi|\psi\rangle} = \sum_{i=1}^{N} \left\{ \langle\psi| - \frac{\hbar^2}{2m}\nabla_i^2|\psi\rangle + \langle\psi|\hat{V}_{\text{ext}}(\mathbf{r}_i)|\psi\rangle \right\} + \frac{1}{2}\sum_{i,j=1}^{N} \langle\psi|\hat{V}(|\mathbf{r}_i - \mathbf{r}_j|)|\psi\rangle \tag{1.15}$$

By substituting (1.14) into the average energy (1.15), expression (1.15) can be rewritten in term of

the single state function ϕ,

$$\begin{aligned} E &= -N\frac{\hbar^2}{2m}\int d\mathbf{r}\,\phi^*(\mathbf{r})\nabla^2\phi(\mathbf{r}) + N\int d\mathbf{r}\,\phi^*(\mathbf{r})\hat{V}_{\text{ext}}\phi(\mathbf{r}) \\ &+ \frac{N(N-1)}{2}\int\int d\mathbf{r}\,d\mathbf{r}'\,\phi^*(\mathbf{r}')\phi^*(\mathbf{r})\hat{V}(|\mathbf{r}-\mathbf{r}'|)\phi(\mathbf{r}')\phi(\mathbf{r}) \end{aligned} \tag{1.16}$$

Considering the effective interaction potential derived in the last subsection, the interacting potential converts into a constant and the energy of the system can be represented as functional of $\phi(\mathbf{r})$ and its complex conjugated $\phi^*(\mathbf{r})$,

$$E(\phi,\phi^*) = N\int d\mathbf{r}\left[\frac{\hbar^2}{2m}\left|\nabla\phi(\mathbf{r})\right|^2 + V_{\text{ext}}(\mathbf{r})\left|\phi(\mathbf{r})\right|^2 + \frac{N-1}{2}U_0\left|\phi(\mathbf{r})\right|^4\right]. \tag{1.17}$$

We want to find the ground state of the system, which is associated with the ground sate. This can be found by minimazing (1.17) subject to the constriction of the normalization condition. This is achieved by the method of the Lagrange's method of undetermined multipliers. Similitude with the free energy of Helmholtz, $F = E - \mu N$, which also consideres the restriction in the number of particles of the system is found. The minimization of (1.17) can be realized with respect to independent variations of $\phi(\mathbf{r})$ and its complex conjugate $\phi(\mathbf{r})^*$, with the restriction of the normalization condition. The minimization with respect to ϕ^*, represented as

$$\frac{\delta F}{\delta\phi^*} = N\int\left[-\frac{\hbar^2}{2m}\nabla^2\phi(\mathbf{r}) + V_{\text{ext}}(\mathbf{r})\phi(\mathbf{r}) + (N-1)U_0|\phi(\mathbf{r})|^2\phi(\mathbf{r}) - \mu\phi(\mathbf{r})\right]\delta\phi^*(\mathbf{r})\,d\mathbf{r} = 0. \tag{1.18}$$

Thus, the quantity inside the square bracket need to be zero. Since a macroscopic N number is considered to be in the same state, the approximation $N \approx N-1$ can be introduced. With these considerations the mean-field equation for the $\phi(\mathbf{r})$ single-state is found,

$$-\frac{\hbar^2}{2m}\nabla^2\phi(\mathbf{r}) + V_{\text{ext}}(\mathbf{r})\phi(\mathbf{r}) + NU_0|\phi(\mathbf{r})|^2\phi(\mathbf{r}) = \mu\phi(\mathbf{r}). \tag{1.19}$$

Equation (1.19) is known as the time independt Gross-Pitaevskii equation and takes this form when the total wave function is normalized as

$$\int|\psi(\mathbf{r})|^2\,d\mathbf{r} = 1. \tag{1.20}$$

If the normalization $\int|\psi(\mathbf{r})|^2\,d\mathbf{r} = N$ is considered, then the N constant in the interaction term of (1.19) is absorbed in the norm and do not appear explicity in the equation.

Equation (1.19) has the form of a Schrödinger equation with an effective potential defined by the sum of V_{ext} and the non-linear term $U_0\left|\psi\left(\mathbf{r}\right)\right|^2$, which take into account the average interaction

of a boson with the rest of them. By analogy, a time dependent Gross-Pitaevskii equation can be defined, for the wave function $\Psi(\mathbf{r},t)=\psi(\mathbf{r})\mathrm{e}^{i,\Phi t}$

$$\imath\hbar\frac{\partial}{\partial t}\Psi\left(\mathbf{r},t\right)=\left(-\frac{\hbar^2}{2m}\nabla^2+V_{\mathrm{ext}}\left(\mathbf{r}\right)+\frac{4\pi\hbar^2a_s}{m}\left|\Psi\left(\mathbf{r},t\right)\right|^2\right)\Psi\left(\mathbf{r},t\right). \tag{1.21}$$

Now that we have arrived to the mean field equation that describes a BEC, we are going to present a dissipative version of the GPE, given by

$$\left(\imath-\gamma_d\right)\hbar\frac{\partial}{\partial t}\Psi\left(\mathbf{r},t\right)=\left(-\frac{\hbar^2}{2m}\nabla^2+V_{\mathrm{ext}}\left(\mathbf{r}\right)+\frac{4\pi\hbar^2a_s}{m}\left|\Psi\left(\mathbf{r},t\right)\right|^2\right)\Psi\left(\mathbf{r},t\right), \tag{1.22}$$

where parameter γ_d is a phenomenological parameter that takes into account dissipation and damping in ultracold atoms. This is a method for modeling energy loss due to interactions with the environment. The coefficient γ_d modifies the standard time-dependent GPE by incorporating dissipation, which acts like a friction coefficient. This procedure can be viewed as an analogy to Fourier's heat equation by treating dissipation in quantum systems in a manner similar to diffusion in classical systems. In the dynamics of a BEC, the wave function evolves under the influence of external potentials and interactions; however, when dissipation is introduced, it behaves similarly to a diffusive system. Thus, γ_d represents a damping term, meaning that the condensate loses energy over time.

Mean field equations (1.21) and (1.22) can also describe dilute Fermi gases in the degenerate BEC limit [50]. In general, the interactions in a dilute Fermi gas are parametrized by the dimensionless interaction strength $\eta\equiv(k_Fa_s)^{-1}$, where k_F is the Fermi wavevector, $k_F=\sqrt{2mE_F}/\hbar$, E_F is the Fermi energy, m is the atomic mass, and a_s is the interatomic scattering length as previously defined. When η takes values between the interval $-1\leq\eta\leq1$, the system is in the strongly interacting regime, called the BEC-BCS crossover [51]. Moreover, regimes with $\eta\gg1$ and $\eta<-1$ correspond to the BEC and BCS limits, respectively. Thus, for equation (1.21) being appropriate to describe the BEC limit of a dilute Fermi gas, it is necessary that condition $\eta\gg1$ is satisfied. In this regime, equations (1.21) and (1.22) retain their form, but the definitions of some parameters change. As will be plenty discussed in Chapter 4, the GP equation of a molecular BEC with the dissipation terms is given by,

$$(\imath-\gamma_d)\hbar\frac{\partial}{\partial t}\Psi(\mathbf{r},t)=\left(-\frac{\hbar^2}{2M}\nabla^2+V_{\mathrm{ext}}(\mathbf{r},t)+\frac{4\pi\hbar^2a_M(t)}{M}|\Psi(\mathbf{r},t)|^2\right)\Psi(\mathbf{r},t), \tag{1.23}$$

where M accounts for the mass of the diatomic molecule and a_M is the scattering length characterizing the interaction of the bosonic molecules. This last parameter is defined as $a_M = 0.6 \times a_s$, with a_s as the scattering length between the fermionic atoms [52].

1.5 Feshbach Resonances

The interaction between particles is one of the most important features of ultracold matter systems. Cooling into an equilibrium state would not be possible if the atoms could not redistribute their momentum and energy by their interactions. Besides, and as this work demonstrates, interactions are responsible for the arising of density patterns in degenerate quantum gases. However, interactions in ultracold matter systems are important because they make the phenomena more interesting and because, experimentally, it is possible to control and tune them. The tunning of interaction between particles is experimentally achieved by Feshbach resonances [53, 54].

For any central potential that admits bound and continuum states, a resonance potential arises when the energy of the two incoming particles matches a high energy bounded state, i.e., a weak bound state. In this situation, a metastable bound state will be formed and then released since the system has a small positive energy coming from the scattered system. This phenomenon is called a resonance potential [55]. However, Feshbach resonances arise due to the presence of more complex physics. In a very brief way, Feshbach resonances are a consequence of the internal structure of the atoms and the presence of an external magnetic field.

When the internal structure of the atom is considered, there is not just one potential, but it can be as many as the electronic configuration admits. For example, the interaction of two alkali atoms in their ground state can be described by two effective potentials, depending on the total electronic spin state $S = s_1 + s_2$. If the separate atoms have anti-parallel spins, which result in a total spin momentum of $S = 0$, the interaction between both particles is given by a singlet potential (blue curve in Figure 1.1). However, if atoms have parallel spins, and thus a total spin momentum of $S = 1$, their interaction is different due to the Pauli Principle Exclusion. This interaction is described by the triplet potential (red curve in Figure 1.1). Both potentials have very different energies between them. A singlet potential is deeper and thus more stable due to the Coulomb electron-nucleus attraction, which is favorable since the electrons have different spin states and can be in the same orbital. In the triplet state, the Coulomb electron-nucleus attraction is unfavorable

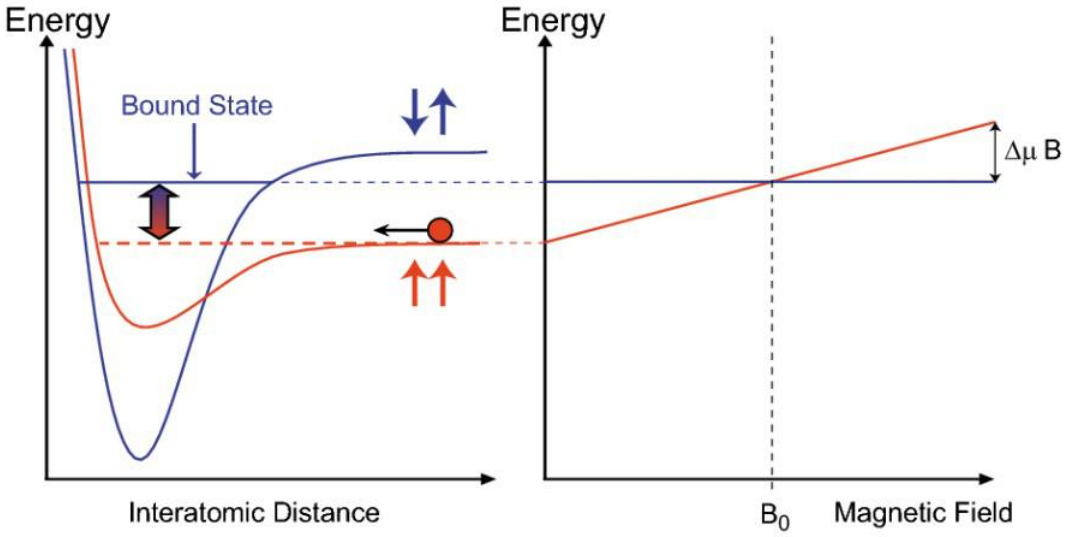

Figure 1.1: Principle of Feshbach resonances. The red curve potential describes the interaction of is particles with parallel spins, and the interaction of the particles with anti-parallel spins is given by the blue curve. Initially, it is observed that two particles with parallel spins collide with an energy corresponding to the continuum states of the red curve. By tuning the external magnetic field, the bound state admitted in the blue curve can be brought into resonance with the incoming state (at a magnitude B_0 of the magnetic field on the right graph). (Image taken from reference [56]).

since the Pauli exclusion principle prevents the electrons from being in the same space.

Modifying the energies between both potentials through an external magnetic field, which induces a Zeeman effect, is possible. When a magnetic field is introduced into the system, the degeneracy of the triplet state in the projection states $m_s = -1, 0, 1$ is broken, and it is possible to shift the triplet potential with respect to the singlet potential until the energy of the incoming particles coincides with the energy of a bounded state in the singlet potential.

For example, Figure 1.1 illustrates the case in which two incoming particles with parallel spins have energy that coincides with a continuum state of the triplet potential. When an external magnetic field is applied, this collision energy can be varied to be resonant with a bound state in the singlet potential. Thus, a diatomic molecule is formed. This is the mechanism that allows the generation of molecular Bose-Einstein Condensates that arise from a Fermi gas, which will be discussed in the next section.

The dependence of the scattering length a_s with respect to the external magnetic field B is given by:

$$a(B) = a_{bg}\left(1 - \frac{\Delta}{B - B_0}\right), \tag{1.24}$$

where a_{bg} is the scattering length associated with the interaction in the continuum of the triplet potential. The parameter B_0 denotes the value of the magnetic field where the resonance occurs, and Δ is the resonance width [49].

1.6 BEC-BCS crossover

Feshbach resonances are a very important tool in manipulating interactions in ultracold gases. One of its most important applications is the study of the BEC-BCS crossover, which is achieved in ultracold Fermi gases.

The BEC-BCS crossover is a smooth transition between different regimes of pairing and interaction between atoms in a fermionic system. The interaction strength between fermions is characterized by the dimensionless interaction parameter $(k_F a_s)^{-1}$, where k_F is the Fermi wavevector. By the simple change of a magnetic field, and thus by the shift in the scattering length, the interactions between atoms can be controlled over an enormous range.

Depending on the value of this interaction parameter, it can be distinguished three different regimes, each one with a very different physics behavior:

- BCS limit ($\eta \ll -1$): This regimen is characterized by a small and negative scattering length $a_s < 0$, which generates a weak attraction between fermions. Due to the attractive interaction, fermions pair into Cooper pairs, which are described by the BCS theory.

- Unitary ($\eta \sim 0$): This regimen is achieved when the scattering length diverges, $a_s \to \infty$, and the system exhibits a strongly correlated behavior. The system remains a fermionic superfluid but presents intermediate properties between the BCS and BEC regimes. These properties and the behavior of the system in the Unitary regime are found to be universal, since the physics is independent of the nature of the molecular state [56].

- BEC limit ($\eta \gg 1$): In this regime, the system couples to a potential that admits bound states. Thus, the system does not behave as a Fermi gas but as a diatomic molecular Bose

gas that has repulsive interactions. Since the scattering length is large and positive, $a_s > 0$, the diatomic molecules interact repulsively.

Figure 1.2 illustrates the BEC-BCS mechanism, observed in the ^{6}Li isotope, as a simplified model of two potentials that are coupled between them through a Feshbach resonance. Since ^{6}Li are fermions, for the interactions to be present, all the particles can not be in the same spin, but they need to be in a balanced 50/50 mixture of two different states in order to maintain the superfluid phase that wants to be reached. In Figure 1.2, a spin mixture of the hyperfine projections states $m_F = 1/2$ and $m_F = -1/2$ is presented. For large and positive values of scattering length and an external magnetic field with a magnitude below 80 mT, the Fermi atoms are coupled in a bosonic diatomic molecule that generates a condensate below the critical temperature T_c. Once the magnetic field is increased, a_s reaches the resonance and diverges at ~ 85 mT. This region is the Unitary regime, which, in this case, has a resonance broad of ~ 10 mT. For larger values of 90 mT in the magnetic field, the system access to the BCS regime, characterized by a small and negative scattering length, resulting in an attractive interaction between the fermion species and a Cooper pairing type.

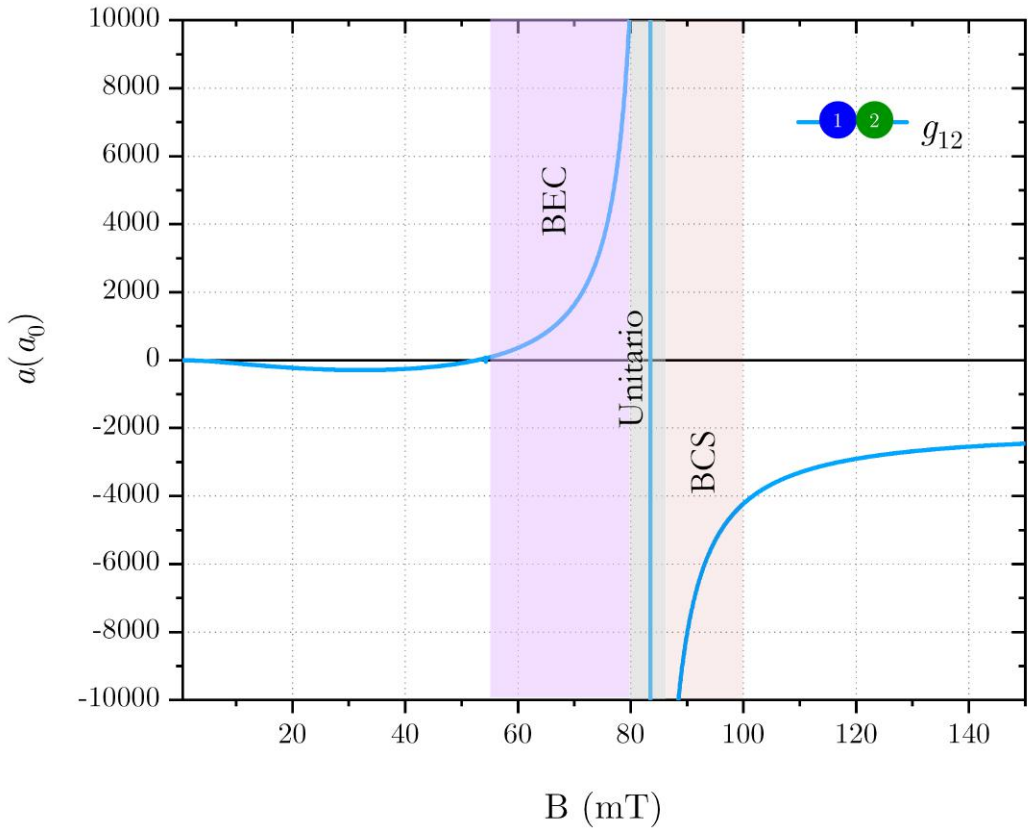

Figure 1.2: BEC-BCS crossover for a fermi gas of ^{6}Li in a balanced mixture 50/50 of the hyperfine states with $m_F = 1/2$ and $m_F = -1/2$.

Chapter 2

Parametric Excitations in a BEC and Collective Excitations

2.1 Overview

It can be said that life would not exist without interactions since there would not be the formation of molecules and complex systems. In a theoretical treatment, matrices would be diagonal, with no coupling between terms. There would be no physical phenomena that intrigue scientists, but scientists would not exist either. That is the importance of interactions: that they are responsible for life.

However, interactions make it impossible to study analytically a system of many particles. Without interactions, the system would be separable and easy to solve. That is why, in many cases, interactions are commonly ignored as a first approximation. That was the case when predicting a Bose-Einstein Condensate. An ideal gas consisting of non-interacting Bose particles can be studied in the formalism of statistical thermodynamics, and it is found that below a certain critical temperature T_C, the system undergoes a phase transition where all the bosons occupy the same energy level. Nevertheless, it is not until interactions are considered that other phenomena, such as superfluidity and collective excitations arise and characterize the system.

This chapter discusses the collective oscillation modes of a BEC, which emerge when the system is modulated at specific frequencies and are a consequence of the dissipation of energy between the interacting particles. First, the behavior of these collective excitations is described using the hydrodynamic approximation. This approximation holds because a degenerate gas can be phenomenologically described with the Navier-Stokes and diffusion equation. Subsequently, the variational method of fields is presented as an alternative method for studying the collective oscillations of

the BEC. Through this last approximation, it is evident that excitations arise as an answer to a parametric excitation, which is described by the Mathieu equation. Thus, the last section of this chapter discusses some important characteristics of this equation.

2.2 Collective Modes through an Hydrodynamic Approximation

As this section will show, a Bose-Einstein Condensate exhibits phenomenological hydrodynamic behavior. Thus, it can be described by a set of hydrodynamic equations usually defined for the density $\rho(\mathbf{r},t) = |\Psi(\mathbf{r},t)|^2$ and for the gradient of its phase which is proportional to the local velocity of the condensate [49],

$$\mathbf{v}(\mathbf{r},t) = \frac{\hbar}{2m\imath}\frac{[\Psi^*(\mathbf{r},t)\nabla\Psi(\mathbf{r},t) - \Psi(\mathbf{r},t)\nabla\Psi^*(\mathbf{r},t)]}{\Psi^*(\mathbf{r},t)\Psi(\mathbf{r},t)}. \tag{2.1}$$

As expected, this set of equations should be connected to the GPE (1.21) describing a condensed Bose gas. In order to establish this connection, it is useful to rewrite the wave function of the BEC as:

$$\Psi(\mathbf{r},t) = f(\mathbf{r},t)\mathrm{e}^{\imath S(\mathbf{r},t)}, \tag{2.2}$$

where $f(\mathbf{r},t)$ is the amplitude and $S(\mathbf{r},t)$ is a phase [57, 58]. In this way, the density is expressed as $\rho(\mathbf{r},t) = f^2(\mathbf{r},t)$ and the field velocity is only expressed in terms of the wave function phase, $\mathbf{v}(\mathbf{r},t) = \frac{\hbar}{m}\nabla S(\mathbf{r},t)$.

Substituting equation (2.2) in (1.21) gives the following equation:

$$\begin{aligned}\imath\hbar f\frac{\partial f}{\partial t} - \hbar f^2\frac{\partial S}{\partial t} = &- \frac{\hbar^2}{2m}\left[f\nabla^2 f - f^2(\nabla S)^2\right] \\ &- \frac{\imath\hbar^2}{2m}\left[2f(\nabla f)(\nabla S) + f^2(\nabla^2 S)\right] \\ &+ Vf^2 + \frac{4\pi\hbar^2 a_s}{m}f^4,\end{aligned}$$

for which it is possible to identify the terms involving the amplitude $f(\mathbf{r},t)$ and the phase $S(\mathbf{r},t)$, and thus, the terms related with the density $\rho(\mathbf{r},t)$ and the field velocity $\mathbf{v}(\mathbf{r},t)$, respectively, by the previously given relations. In this sense, the last expression can be separated into two different equations, which are referred to as the hydrodynamic equations.

The first hydrodynamic equation is defined as:

$$\frac{\partial\rho}{\partial t} + \nabla\cdot(\rho\mathbf{v}) = 0. \tag{2.3}$$

The second hydrodynamic equation for a BEC is given by,

$$m\frac{\partial \mathbf{v}}{\partial t} + \nabla\left(\delta\mu + \frac{1}{2}m\mathbf{v}^2\right) = 0, \tag{2.4}$$

where

$$\delta\mu = V_{\text{ext}} + \frac{4\pi\hbar^2 a_s}{m}\rho - \frac{\hbar^2}{2m\sqrt{\rho}}\nabla^2\sqrt{\rho} - \mu \tag{2.5}$$

is the change of the chemical potential with respect to its ground state value μ. Both equations, (2.4) and (2.5), were not obtained by any approximation in the GPE and works in the linear and nonlinear regimes.

In fluid mechanics, the analogue of equation (2.4) is a equation of mass conservation, while in quantum mechanics is for the probability conservation, i.e., for a Bose-Einstein Condensate it assures that the density of the condensate is a conserved quantity. Equation (2.5) establishes the irrotational nature of the superfluid flow and in fluid mechanics is related to the conservation of momentum.

The density ρ_0 relative to the ground state is obtained by setting $\mathrm{v} = 0$ and $\delta\mu = 0$. This gives the equation,

$$V_{\text{ext}} + \frac{4\pi\hbar^2 a_s}{m}\rho_0 - \frac{\hbar^2}{2m\sqrt{\rho_0}}\nabla^2\sqrt{\rho_0} - \mu = 0, \tag{2.6}$$

which coincides with the GPE for the order parameter $\Psi_0 = \sqrt{\rho_0}$ of the ground state. The third term of equation 2.6 is known as quantum pressure, $\frac{\nabla^2\sqrt{\rho_0}}{\sqrt{\rho_0}}$, and is a pure quantum effect. When the condensate is uniform, i.e., in the absence of an external potential, this contribution vanishes. Thus, it is a consequence of the confinement of the atoms, and it is interpreted as a force that opposes the squeezing of the condensate so that the absolute zero temperature can not be reached. When the number of atoms in the trap is sufficiently large, the density profile $\rho_0(\mathbf{r})$ becomes smooth, and the quantum pressure $\frac{\nabla^2\sqrt{\rho_0}}{\sqrt{\rho_0}}$ term can be neglected with respect to the interaction term in (2.6). As it is shown in [57], by neglecting this term in equations (2.4) and (2.5) one obtains that the change of the chemical potential is given by the simple expression

$$\delta\mu = \frac{4\pi\hbar^2 a_s}{m}(\rho - \rho_0), \tag{2.7}$$

where the ground state density takes the Thomas-Fermi form,

$$\rho_0(\mathbf{r}) = \frac{m}{4\pi\hbar^2 a_s}\left[\mu - V_{\text{ext}}(\mathbf{r})\right]. \tag{2.8}$$

Finally, assuming an isotropic harmonic oscillator potential $V_{\text{ext}} = \frac{\omega_0^2 r^2}{2m}$, it is found that the dispersion law of the normal modes for an inhomogeneous Bose-Einstein Condensate is given by [57],

$$\omega(n,l) = \omega_0(2n^2 + 2nl + 3n + l)^{\frac{1}{2}}, \tag{2.9}$$

in contrast with the prediction of the harmonic oscillator (HO) model without interparticle interactions,

$$\omega_{HO} = \omega_0(2n + l). \tag{2.10}$$

In conclusion, an analytic expression for the normal modes of a BEC can be obtained when the repulsive interaction is large enough to make the kinetic energy pressure negligible compared to the external and interparticle interactions terms. This conditions correspond to the Thomas-Fermi approximation in the calculation of the ground state, which is valid for positive and large values of the non-dimensional parameter $\frac{Na_s}{a_{HO}}$, where a_{HO} is the harmonic oscillator length characterizing the trap and defined as $a_{HO} = \sqrt{\frac{\hbar}{m\omega_o}}$, and to a large number of atoms.

2.3 Collective Modes through a Variational Approximation

In this section, the frequencies of the collective modes of a BEC are obtained through a variational method for fields, in contrast with the last section, where the system was characterized by a hydrodynamic approach. As will be discussed, the variational method allows the study of the system in different configurations. While the hydrodynamic equations for a BEC are restricted to an isotropic potential, the variational method admits any configuration of V_{ext}. In addition, with the variational method, collective excitations can be understood as small deviations of equilibrium states arising from a perturbation through some system parameters.

In this work, the perturbation in the system is introduced in two different ways: i) through one of the trap frequencies or ii) through the scattering length. Also, two different geometries for the external potential are considered: prolate and oblate. All these different configurations yield three sets of variational equations of motion, describing the system's dynamics. As will be discussed, the efficiency of the variational method depends on the appropriate selection of an ansatz for the wave function. For a BEC, a good ansatz that reproduces the experimental observations is a Gaussian function, which also takes into account the thermal contribution of the Bose gas.

The parametric modulation schemes proposed in this chapter are experimentally motivated. Specifically, the modulation of the trap frequencies is completely accessible. However, and as will be discussed in this chapter, the modulation of the scattering can not be reached for high values of magnetic fields, as is the case in the experiment of ^{6}Li. Nevertheless, we still chose to study this parametric modulation since the behavior of a BEC is independent of the atomic species and can be interesting for other experiments.

2.3.1 Method for Fields or Lagrangian Formalism

The Lagrangian formalism for a system of fields is a generalization of the formalism for a system of particles. In classical mechanics, the Lagrangian and its equations of motion are used to know the temporal evolution and, thus, the trajectory of a system of N particles. In quantum mechanics, the same idea is generalized for a field, but in this case, we do not look for trajectories but for the values that takes the wave function at different points of space and time.

Before we introduce the Lagrangian formalism for fields, lets briefly resume the theory for particles. A system of particles can be described by a finite set of generalized coordinates $q_i(t)$ with $i = 1, 2, \cdots, N$. The Lagrangian associated to the system is defined as a function of the coordinates q_i and the generalized velocities $\dot{q}_i$, $L\left(q_i(t), \dot{q}_i(t)\right) = T - V$. From this quantity it is possible to derive the equations of motion by defining the action

$$I = \int_{t_1}^{t_2} L\left(q_i(t), \dot{q}_i(t)\right)\, dt. \tag{2.11}$$

The equations of motion can be derived by requiring that the action remains stationery for infinitesimal variations of the functions $q_i(t)$,

$$\delta I = \int_{t_1}^{t_2} \sum_{i=1}^{N} \left(\frac{\partial L}{\partial q_i} - \frac{d}{dt}\frac{\partial L}{\partial \dot{q}_i} \right) \delta q_i \, dt = 0 \tag{2.12}$$

These variations are arbitrary except for the constraint that they vanish at the times t_1 and t_2. The action will be stationary for arbitrary choices of the functions δq_i if and only if all these functions have zero coefficients. This implies the restrictions,

$$\frac{d}{dt}\frac{\partial L}{\partial \dot{q}_i} - \frac{\partial L}{\partial q_i} = 0 \tag{2.13}$$

which are known as the Euler-Lagrange equations.

For the field case, the Lagrangian is defined as,

$$L = \int \mathcal{L}\left(\psi, \partial\psi/\partial t, \partial\psi/\partial x^k\right) d^3x, \tag{2.14}$$

where $\mathcal{L}\left(\psi, \partial\psi/\partial t, \partial\psi/\partial x^k\right)$ is the Lagrangian density that is a function of the field ψ and their derivatives in time $\partial\psi/\partial t$ and space $\partial\psi/\partial x^k$ with $k = 1, 2, \cdots$. The action integral is then given by,

$$I = \int_{t_1}^{t_2} L\, dt = \int_{t_1}^{t_2} \left\{ \int \mathcal{L}\left(\psi, \partial\psi/\partial t, \partial\psi/\partial x^k\right) d^3x \right\} dt. \tag{2.15}$$

The equations of motion are obtained by requiring that the action remains invariant under an infinitesimal variation of the field $\delta\psi(x,t)$, which are of the form

$$\delta\left(\frac{\partial\psi}{\partial t}\right) = \frac{\partial}{\partial t}\delta\psi, \qquad \delta\left(\frac{\partial\psi}{\partial x^k}\right) = \frac{\partial}{\partial x^k}\delta\psi.$$

Thus, the variation in the action can be written as:

$$\delta I = \int_{t_1}^{t_2} \left\{ \int \left[\frac{\partial\mathcal{L}}{\partial\psi} - \frac{\partial}{\partial t}\frac{\partial\mathcal{L}}{\partial(\partial\psi/\partial t)} - \frac{\partial}{\partial x^k}\frac{\partial L}{\partial(\partial\psi/\partial x^k)} \right] \delta\psi\, d^3x \right\} dt.$$

Since $\delta\psi$ is an arbitrary function, the action will be stationary if the term in the square bracket is zero,

$$\frac{\partial\mathcal{L}}{\partial\psi} - \frac{\partial}{\partial t}\frac{\partial\mathcal{L}}{\partial(\partial\psi/\partial t)} - \frac{\partial}{\partial x^k}\frac{\partial L}{\partial(\partial\psi/\partial x^k)} = 0. \tag{2.16}$$

Condition (2.16) is known as the Euler-Lagrangian equations for fields and resembles to equation (2.13) for the particle case.

Depending on the system of interest, the Lagrangian take an specific form and its connected to the Hamiltonian of the system by the Legendre transformation,

$$H = \int \psi\frac{\partial\mathcal{L}}{\partial\psi}\, d^3x - L = \int \left(\psi\frac{\partial\mathcal{L}}{\partial\psi} - \mathcal{L}\right) d^3x. \tag{2.17}$$

The variational approach in this field formalism is introduced when, instead of solving for a numerical solution of the system's time evolution, one assumes to know the form of the wave function describing the system through an ansatz ψ, which will depend on a set of time-dependent variational parameters $\{h(t)\}$, i.e., $\psi \equiv \psi\left(\mathbf{r}; \{h(t)\}\right)$. This ansatz is substituted in the density Lagrangian, and the equations of motion of the system are obtained by the relations,

$$\frac{\partial}{\partial h_i} L\left(t; \{h(t)\}\right) = \frac{d}{dt}\left(\frac{\partial}{\partial \dot{h}_i}\right) L\left(t; \{h(t)\}\right) \tag{2.18}$$

Thus, in the variational method of fields, instead of solving the Schrödinger equation associated with the problem of interest, one uses the equivalent Lagrangian density formalism and proposes an ansatz to the wave function so that the temporal dynamic reduces to a set of coupled algebraic equations associated to each of the variational parameter $h_i(t)$.

2.3.2 Study of a BEC in cylindrical coordinates

The Lagrangian density for a Bose-Einstein Condensate is defined as:

$$\mathcal{L}(\mathbf{r},t) = \frac{\imath\hbar}{2}\left(\Psi^*\frac{\partial\Psi}{\partial t} - \Psi\frac{\partial\Psi^*}{\partial t}\right) - \frac{\hbar^2}{2m}|\nabla\Psi|^2 - V_{\text{ext}}(\mathbf{r},t)|\Psi|^2 - \frac{1}{2}g(t)|\Psi|^4, \tag{2.19}$$

which reproduces the GPE (1.21) by the relation,

$$\frac{\partial\mathcal{L}}{\partial\Psi^*} - \frac{d}{dt}\frac{\partial\mathcal{L}}{\partial\dot{\Psi}^*} - \nabla\cdot\frac{\partial\mathcal{L}}{\partial\nabla\Psi^*} = 0. \tag{2.20}$$

Thus, the GPE (1.21) can be equivalently described as a variational equation derived from the non stationary Lagrangian density (2.19) [59].

Experimentally, the collective modes of a degenerate Bose gas are induced by an external modulation over some parameter of the system. As mentioned, this work considers the modulation of the trapping potential V_{ext} and the modulation of the interaction between particles g, thus a temporal dependence in this parameters is introduced in (2.19). The case where both quantities are simultaneously modulated is not considered; the system is excited by modulating only one of them.

The external potential considered in this work is an harmonic potential, which in cylindrical coordinates $\{r,\theta,z\}$ takes the form,

$$V_{\text{ext}}(\mathbf{r},t) = \frac{1}{2}m(r^2\omega_r^2(t) + z^2\omega_z^2(t)). \tag{2.21}$$

The temporal dependence on $\omega_r(t)$ and $\omega_z(t)$ indicates the possibility of modulating any of them. It is important to clarify that the modulation is introduced only through the most confining frequency of the trap. In the case of a prolate (also denoted as "cigar-shaped") BEC, ω_r is the frequency modulated while ω_z is kept constant. Equivalently, for an oblate (or "pancake-shaped") system, ω_z is modulated while ω_r is kept unchanged. Also, when the trap is driven, the interaction parameter g remains constant during the whole dynamics of the system.

As will be discussed in Chapter 3, in current experiments, optical dipole traps are widely employed to generate the harmonic potential in which the BEC is confined [60]. These traps are

produced by focusing a far red-detuned laser beam. The harmonic frequencies are related to the power of the said beam, P, as $\omega_k \propto \sqrt{P}$. Therefore, the modulation of the trap frequencies can be achieved by modulating the power of the optical beam confining the atoms. Since the modulation can be considered a small perturbation, the trap frequencies are correctly described as

$$\omega_k(t) = \omega_{k0}\sqrt{1+\alpha\cos\Omega(t-t_0)} \approx \omega_{k0}\left(1+\tfrac{\alpha}{2}\cos\Omega(t-t_0)\right), \quad k=r,z, \tag{2.22}$$

where ω_{k0} is the initial value of the trap frequency that is modulated, α is the amplitude of the modulation satisfying $\alpha \ll 1$, Ω is the external frequency of modulation, and $t_0 = -\pi n/(2\Omega)$ with n as an integer is a phase that ensures that a $t = 0$, the experimental modulation is zero.

For the case in which the system is excited by modulating the interaction parameter $g(t)$ while keeping the trapping potential constant, the modulation is defined as:

$$g\left(t\right) = \frac{4\pi\hbar a_s(t)}{m}, \quad a_s\left(t\right) = a_{s0}\left(1+\alpha\cos\Omega\left(t-t_0\right)\right), \tag{2.23}$$

where a_{s0} is the initial scattering length.

Now that the density Lagrangian of the system and its temporal modulation are defined, the next step is to propose an *ansatz* for the wave function describing the BEC. In this work, the *ansatz* considered is a Gaussian function of the form,

$$\Psi\left(\mathbf{r};\{\boldsymbol{q}\left(t\right)\}\right) = f(t)\exp\left[-\frac{r^2}{2\sigma_r^2(t)}+\imath\beta_r(t)r^2\right]\exp\left[-\frac{z^2}{2\sigma_z^2(t)}+\imath\beta_z(t)z^2\right], \tag{2.24}$$

where the introduced time-dependent variational parameters are the Gaussian widths of the atomic cloud in the axial $\sigma_z(t)$ and radial $\sigma_r(t)$ directions, as well as the corresponding axial $\beta_z(t)$ and radial $\beta_r(t)$ phases. This variational parameter are compactly denoted by $\{\boldsymbol{q}(t)\} = \{\sigma_r, \sigma_z, \beta_r, \beta_z\}$.

In the *ansatz* (2.24), the function $f(t)$ denotes the normalization function defined as

$$f(t) = \sqrt{\frac{N}{\pi^{3/2}\sigma_z\left(t\right)\sigma_r^2\left(t\right)}},$$

which guarantees the accomplishment of the continuity equation and the normalization of the ansatz function to a constant atom number N. This ansatz does not include the possibility of a vortex at the center, which could be incorporated through a factor of the form $\left(re^{\imath\theta}\right)^{\ell}$ and it is discussed in Chapter 5, where perspectives are described.

It is important to discuss that, although the solution to the GPE in the limit of strong interactions is given by the Thomas-Fermi approximation, a Gaussian function as an ansatz is also a very

good approximation. A Gaussian function describes a system conformed by a thermal gas; however, experimentally, the condensation of a Bose gas is always accomplished with a thermal component. So, there is never a pure Thomas-Fermi distribution. As it would be discussed in Chapter 3, the Gaussian function gives solutions that are in very good agreement with experimental observations, and also are easier to deal numerically.

Now that the density Lagrangian and the corresponding *ansatz* are presented, it is time to obtain the variational equations of motion that characterize the system's temporal evolution. The Lagrangian is obtained by substituting *ansatz* (2.24) into Eq. (2.19) and integrating over the spatial coordinates. This procedure gives the following terms:

Temporal Term

$$\int_{-\infty}^{\infty} dz \int_0^{2\pi} d\theta \int_0^{\infty} dr\, r \left[\frac{\imath\hbar}{2} \left(\Psi \frac{\partial \Psi^*}{\partial t} - \Psi^* \frac{\partial \Psi}{\partial t} \right) \right] = \frac{\hbar}{2} \left[2\sigma_r^2 \dot{\beta}_r + \sigma_z^2 \dot{\beta}_z \right]$$

Kinetic Term

$$\int_{-\infty}^{\infty} dz \int_0^{2\pi} d\theta \int_0^{\infty} dr\, r \frac{\hbar^2}{2m} |\nabla \Psi|^2 = \frac{\hbar^2}{m} \frac{\sigma_r^2 + 4\alpha^2 \sigma_r^2 \sigma_z^4 + 2\sigma_z^2 \left[4\beta^2 \sigma_r^4 + 1 \right]}{4\sigma_r^2 \sigma_z^2}$$

External Potential Term

$$\int_{-\infty}^{\infty} dz \int_0^{2\pi} d\theta \int_0^{\infty} dr\, r \frac{m}{2} \left[\omega_r^2 r^2 + \omega_z^2 z^2 \right] |\Psi|^2 = \frac{m}{4} \left(2\omega_r^2 \sigma_r^2 + \omega_z^2 \sigma_z^2 \right)$$

Interaction Term

$$\int_{-\infty}^{\infty} dz \int_0^{2\pi} d\theta \int_0^{\infty} dr\, r \frac{g(t) N}{2} |\Psi|^4 = \frac{N g\,(t)}{4\sqrt{2}\pi^{3/2} \sigma_z \sigma_r^2} \equiv \frac{\hbar N a_s(t)}{\sqrt{2\pi} m \sigma_z \sigma_r^2}$$

Thus, the Lagrangian is given by the sum of these fourth terms. As previously mentioned, the variational equations of motion for the four variational parameters are obtained by the relation (2.18). This gives a set of four algebraic equations, each for the σ_r, σ_z, β_r, and β_z parameters. After some algebra, the dynamic is reduced to two coupled equations for the Gaussian widths σ_r and σ_z since the equations for phases β_r and β_z are in terms of these Gaussian widths in the form,

$$\beta_r = \frac{\dot{\sigma}_r}{2\sigma_r} \quad \beta_z = \frac{\dot{\sigma}_z}{2\sigma_z}.$$

The obtained variational equations are given by,

$$\ddot{\sigma}_r(t) + \omega_r^2(t)\sigma_r(t) - \frac{\hbar^2}{m^2\sigma_r^3(t)} - \frac{g(t)N}{2\sqrt{2}\pi^{3/2}m}\frac{1}{\sigma_z(t)\sigma_r^3(t)} = 0 \tag{2.25a}$$

$$\ddot{\sigma}_z(t) + \omega_z^2(t)\sigma_z(t) - \frac{\hbar^2}{m^2\sigma_z^3(t)} - \frac{g(t)N}{2\sqrt{2}\pi^{3/2}m}\frac{1}{\sigma_r^2(t)\sigma_z^2(t)} = 0. \tag{2.25b}$$

It is useful to rewrite equations of motion (2.25) in terms of the non-dimensional parameters:

$$\begin{aligned} l_0 = \sqrt{\frac{\hbar}{m\omega_0}}, \quad \bar{\sigma}_r = \frac{\sigma_r}{l_0}, \quad \bar{\sigma}_z = \frac{\sigma_z}{l_0}, \quad \bar{\omega}_r = \frac{\omega_r}{\omega_0}, \\ \bar{\omega}_z = \frac{\omega_z}{\omega_0}, \quad \bar{a}_s = \frac{a_s}{l_0}, \quad \bar{\Omega} = \frac{\Omega}{\omega_0}, \quad \bar{t} = t\omega_0\,, \end{aligned} \tag{2.26}$$

where ω_0 is the highest external potential frequency. Thus, its definition depends on the geometry of the trap. In this sense, for prolate confinement, $\omega_0 = \omega_r$, and in the oblate case, $\omega_0 = \omega_z$.

Three possible cases are obtained after introducing the definition of the non-dimensional parameters and considering the modulation in the most confining trap frequency or the modulation of the interaction parameter. For simplicity, the bar notation over the non-dimensional parameters will be omitted. However, from now on, all equations will be presented in the non-dimensional form, unless otherwise clarified.

1. Trap modulation in a prolate geometry ($\omega_{r0} \gg \omega_{z0}$),

$$\ddot{\sigma}_r + \omega_{r0}^2(1 + \alpha\sin\Omega t)\sigma_r = \frac{1}{\sigma_r^3} + \sqrt{\frac{2}{\pi}}\frac{Na_s}{\sigma_r^3\sigma_z}, \tag{2.27a}$$

$$\ddot{\sigma}_z + \omega_{z0}^2\sigma_z = \frac{1}{\sigma_z^3} + \sqrt{\frac{2}{\pi}}\frac{Na_s}{\sigma_r^2\sigma_z^2}, \tag{2.27b}$$

2. Trap modulation in an oblate geometry ($\omega_{r0} \ll \omega_{z0}$),

$$\ddot{\sigma}_r(t) + \omega_{r0}^2\sigma_r = \frac{1}{\sigma_r^3} + \sqrt{\frac{2}{\pi}}\frac{Na_s}{\sigma_r^3\sigma_z}, \tag{2.28a}$$

$$\ddot{\sigma}_z + \omega_{z0}^2(1 + \alpha\sin\Omega t)\sigma_z = \frac{1}{\sigma_z^3} + \sqrt{\frac{2}{\pi}}\frac{Na_s}{\sigma_r^2\sigma_z^2}, \tag{2.28b}$$

3. Scattering length modulation in both geometries,

$$\ddot{\sigma}_r + \omega_r^2\sigma_r = \frac{1}{\sigma_r^3} + \sqrt{\frac{2}{\pi}}\frac{Na_{s0}(1 + \alpha\sin\Omega t)}{\sigma_r^3\sigma_z} \tag{2.29a}$$

$$\ddot{\sigma}_z + \omega_z^2\sigma_z = \frac{1}{\sigma_z^3} + \sqrt{\frac{2}{\pi}}\frac{Na_{s0}(1 + \alpha\sin\Omega t)}{\sigma_r^2\sigma_z^2}. \tag{2.29b}$$

Explicit solutions to equations (2.27)-(2.29) can be obtained by considering a linear response in the change of the Gaussian widths,

$$\sigma_r(t) = \sigma_{r0} + \delta_r(t), \quad \sigma_z(t) = \sigma_{z0} + \delta_z(t).$$

Thus, the initial Gaussian widths σ_{r0} and σ_{z0} only change in time by a small amount $\delta_r(t)$ and $\delta_z(t)$, respectively, that satisfy the inequality $\delta_j \ll \sigma_{j0}$ (with $j = r, z$). With these linear considerations, we arrive to the following results:

1. Prolate geometry with a modulation in the radial trap frequency.

$$\ddot{\delta}_r + [A_r - 2Q_r \cos\Omega(t - t_0)]\,\delta_r = -G\delta_z + f_{r0}\cos\Omega(t - t_0) \tag{2.30a}$$

$$\ddot{\delta}_z + A_z\delta_z = -2G\delta_r. \tag{2.30b}$$

2. Oblate geometry with a modulation in the axial trap frequency.

$$\ddot{\delta}_r + A'_r\delta_r = -G\delta_z \tag{2.31a}$$

$$\ddot{\delta}_z + [A'_z - 2Q'_z \cos\Omega(t - t_0)]\,\delta_z = -2G\delta_r + f'_{z0}\cos\Omega(t - t_0). \tag{2.31b}$$

3. Oblate and prolate geometry with a modulation in the scattering length.

$$\ddot{\delta}_r + [A''_r - 2Q''_r \cos\Omega(t - t_0)]\,\delta_r = [G + b\cos\Omega(t - t_0)]\,\delta_z + f''_{r0}\cos\Omega(t - t_0) \tag{2.32a}$$

$$\ddot{\delta}_z + [A''_z - 2Q''_z \cos\Omega(t - t_0)]\,\delta_z = -2\,[G + b\cos\Omega(t - t_0)]\,\delta_r + f''_{z0}\cos\Omega(t - t_0) \tag{2.32b}$$

The definition of the parameters in the three sets of coupled equations are given by,

1. Equations (2.30), ω_r modulation in a prolate trap :

$$A_z = \left(3\omega_{z0}^2 + \frac{1}{\sigma_{z0}^4}\right), \quad A_r = 4\omega_{r0}^2, \quad Q_r = -\frac{\alpha\omega_{r0}^2}{2}, \quad f'_{r0} = -\alpha\omega_{r0}^2\sigma_{r0}, \quad G = \sqrt{\frac{2}{\pi}}\frac{Na_s}{\sigma_{r0}^3\sigma_{z0}^2}$$

2. Equations (2.31), ω_z modulation in an oblate trap :

$$A_r' = 4\omega_{r0}^2, \quad A_z' = \left(3\omega_{z0}^2 + \frac{1}{\sigma_{z0}^4}\right), \quad Q_z' = -\frac{\alpha\omega_{z0}^2}{2}, \quad f_{z0}' = -\alpha\omega_{z0}^2\sigma_{z0}, \quad G = \sqrt{\frac{2}{\pi}}\frac{Na_s}{\sigma_{r0}^3\sigma_{z0}^2}$$

3. Equations (2.32), a_s modulation in prolate and oblate traps :

$$\begin{aligned} A_r'' &= 4\omega_{r0}^2, \quad Q_r'' = -\frac{3}{2}\sqrt{\frac{2}{\pi}}\frac{N\alpha a_s}{\sigma_{r0}^4\sigma_{z0}}, \quad b = \sqrt{\frac{2}{\pi}}\frac{N\alpha a_s}{\sigma_{r0}^3\sigma_{z0}^2}, \quad f_{r0}'' = \sqrt{\frac{2}{\pi}}\frac{N\alpha a_s}{\sigma_{r0}^3\sigma_{z0}} \\ A_z'' &= 3\omega_{z0}^2 + \frac{1}{\sigma_{z0}^4}, \quad Q_z'' = -\sqrt{\frac{2}{\pi}}\frac{N\alpha a_s}{\sigma_{r0}^2\sigma_{z0}^3}, \quad f_{z0}'' = \sqrt{\frac{2}{\pi}}\frac{N\alpha a_s}{\sigma_{r0}^2\sigma_{z0}^2}, \quad G = \sqrt{\frac{2}{\pi}}\frac{Na_s}{\sigma_{r0}^3\sigma_{z0}^2} \end{aligned}$$

When no external modulation is considered, $\Omega = 0$, the three cases are described by the same dynamical equation, which can be written in the matrix equation form,

$$\ddot{\boldsymbol{\delta}}(t) = \mathcal{W}_0\,\boldsymbol{\delta}(t) \tag{2.33}$$

where $\boldsymbol{\delta}$ is the vector with the Gaussian width variations as its components, $\boldsymbol{\delta}(t) = (\delta_r, \delta_z)^\dagger$, and $\mathcal{W}_0$ is the natural matrix defined as

$$\mathcal{W}_0 = \begin{pmatrix} 4\omega_{r0}^2 & \sqrt{\frac{2}{\pi}}\frac{Na_{s0}}{\sigma_{r_0}^3\sigma_{z_0}^2} \\ 2\sqrt{\frac{2}{\pi}}\frac{Na_{s0}}{\sigma_{r_0}^3\sigma_{z_0}^2} & 3\omega_{z0}^2 + \frac{1}{\sigma_{z_0}^4} \end{pmatrix}. \tag{2.34}$$

By applying a Fourier Transform (FT) to Eq. (2.33), we get the following matrix equation in the frequency domain,

$$(\imath\omega_N)^2\Delta = \mathcal{W}_0\Delta, \tag{2.35}$$

where Δ is the Fourier transform of vector $\boldsymbol{\delta}$. Its diagonalization gives the frequencies of the breathing (monopolar) ω_b and quadrupolar ω_q modes, as the eigenvalues of the matrix $\mathcal{W}_0$, i.e., $\omega_N = \{\omega_b, \omega_q\}$. As a note, it is important to state that other collective excitation modes of higher energy, such as the octupole, exist and are visible experimentally. However, to reproduce them analytically or numerically, other ansatz needs to be proposed. In the dimensionless form, the monopolar ω_b and quadrupolar ω_q mode frequencies are given by:

$$\omega_b = \sqrt{\frac{1}{\sigma_{z0}^4} + 4\omega_{r0}^2 + 3\omega_{z0}^2 + \sqrt{\left(\frac{1}{\sigma_{z0}^4} + 3\omega_{z0}^2 - 4\omega_{r0}^2\right)^2 + \frac{16a_{s0}^2N^2}{\pi\sigma_{r0}^6\sigma_{z0}^4}}} \tag{2.36}$$

$$\omega_q = \sqrt{\frac{1}{\sigma_{z0}^4} + 4\omega_{r0}^2 + 3\omega_{z0}^2 - \sqrt{\left(\frac{1}{\sigma_{z0}^4} + 3\omega_{z0}^2 - 4\omega_{r0}^2\right)^2 + \frac{16a_{s0}^2N^2}{\pi\sigma_{r0}^6\sigma_{z0}^4}}} \tag{2.37}$$

In matrix (2.34), it can be observed that the interaction term of the density Lagrangian (2.19), and thus, the non-linear character of the density, couples the frequency modes of the system that the diagonalization of (2.35) obtains. In addition, interactions couple the oscillations in the radial and axial directions [61], which can be observed in the term $\sim \frac{Na_s}{\sigma_{r0}^3\sigma_{z0}^2}$. This suggests that a 3D characterization of the system is important to properly describe the collective modes.

The solution to matrix (2.35) is plotted in Figure 2.1, where the values of the collective modes ω_q and ω_b are shown for different aspect ratio values. The initial scattering length is fixed to the value $a_{s0} = 1500a_0$, and the number of bosons is taken as $N = 5 \times 10^4$. These values are considered because the simulations discussed in the next chapter are based on the experimental data of the ultracold fermionic ^{6}Li gas within the BEC limit [25, 26, 62].

The collective excitation frequencies, ω_N, are analyzed as a function of the aspect ratio for both oblate and prolate trap geometries. These aspect ratios are defined as ω_{r0}/ω_{z0} for the oblate trap and ω_{z0}/ω_{r0} for the prolate trap. As anticipated, when the aspect ratio is equal to one, the excitation frequencies coincide for both geometries, confirming the consistency of our results across different trapping configurations. This indicates that any geometry derived from adjusting the ratios of a cylindrical harmonic trap adheres to the expected theoretical framework. Furthermore, the validity of defining these hydrodynamic mode frequencies is constrained to specific variations in N, ω_{r0}, ω_{z0}, and a_{s0}, ensuring that the Gross-Pitaevskii Equation (GPE) remains applicable.

Now that the values of the frequencies of the collective modes are known for different configurations of the harmonic trap, it is important to understand the behavior of the Gaussian widths of the ansatz when the condensate is modulated with these frequencies and with a variation in these values. For this, Eqs. (2.30)-(2.32) are solved numerically in two different conditions: when Ω is equal to the breathing mode ω_b (obtained with the variational analysis), making the system to oscillate in resonance, and when Ω is shifted from the breathing mode resonance by a small amount ϵ, $\Omega = \omega_b \pm \epsilon$.

Subplots (ob-a), (pr-a), (ob-c), and (pr-c) of Figure 2.2 shows the response of the system when it is modulated at a frequency equal to the breathing mode resonance, $\Omega = \omega_b$. In this case, the system oscillates with high amplitude in the direction of maximum confinement, whereas the perpendicular axis remains little affected.

Subplots (ob-b), (pr-b), (ob-d), and (pr-d) of Figure 2.2 show that a small variation in the

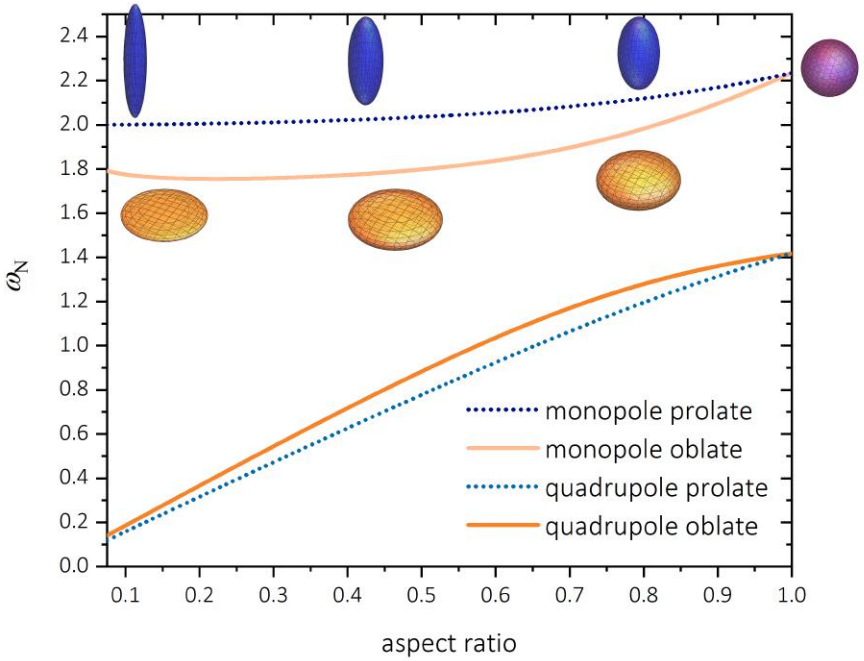

Figure 2.1: Natural frequencies ω_b and ω_q for the breathing (monopole) and quadruple modes, respectively, obtained by a variational analysis for a Bose-Einstein Condensate in oblate and prolate geometries. The solutions plotted in this figure were obtained for $a_s = 1500a_0$ and $N = 5 \times 10^4$. The higher frequencies correspond to the breathing mode, while the lower frequencies are associated with the quadrupole mode. In the left extreme of the chart, where the aspect ratio is the smallest, the prolate trap is at its maximum confinement in the radial direction, while the oblate trap is at its maximum confinement in the axial direction. As the aspect ratio increases, both traps change their configuration until they reach a spherical geometry, and thus the value of the frequencies in each configuration matches.

value of the resonance frequency (breathing mode ω_b) changes the oscillation of the widths in both directions. Thus, the correct characterization of ω_b is a relevant step for properly identifying the resonant regime. In the next chapter, it will be shown that when the system is modulated by a frequency that equals the one of the breathing mode, density patterns are formed in the plane perpendicular to the one where the modulation was introduced [63, 64]. Therefore, a small shift in the resonance frequency, $\Omega = \omega_b \pm \epsilon$, changes the conditions of the system under the density patterns are formed. This small variation in the frequency modulation is also reflected in the periodicity of the temporal patterns obtained by numerical simulations and in the time at which the patterns appear, which will be discussed in the following chapter.

Similarities and differences in cylindric and cartesian coordinates

The density Lagrangian (2.19), the variational equations of motion (2.27)-(2.29), and the frequencies of the collective modes (2.36) are invariant under a change in the coordinates, i.e., are covariant. Thus, the same results are obtained when changing to cartesian coordinates in the study of a prolate and oblate BEC. However, cartesian coordinates $\{x_1, x_2, x_3\}$ admit the center of mass of the BEC to shift. This new degree of freedom describes the collective mode associated with the oscillation of the center of mass of the atomic cloud $\{x_{0_1}, x_{0_2}, x_{0_3}\}$. This oscillation is known as dipole mode and is described by a harmonic oscillator equation in each direction,

$$\ddot{x}_{0_i} + \omega_{x_i}^2 x_i = 0, \qquad i = 1, 2, 3\,. \tag{2.38}$$

2.4 Stabilities and instabilities regions from the Mathieu equations

In section 2.3.2, the discussion on the linearized variational equations (2.30), (2.31) and (2.32) were restricted to its solution and the behavior of the Gaussian widths when a modulation is introduced to the atomic cloud. However, in this section, a further analysis will be presented based on the similarities between this set of equations and the Mathieu equation.

The Mathieu equation is a linear second-order differential equation that differs from the simple harmonic oscillator in a time-varying (periodic) forcing of the stiffness coefficient. In its standard

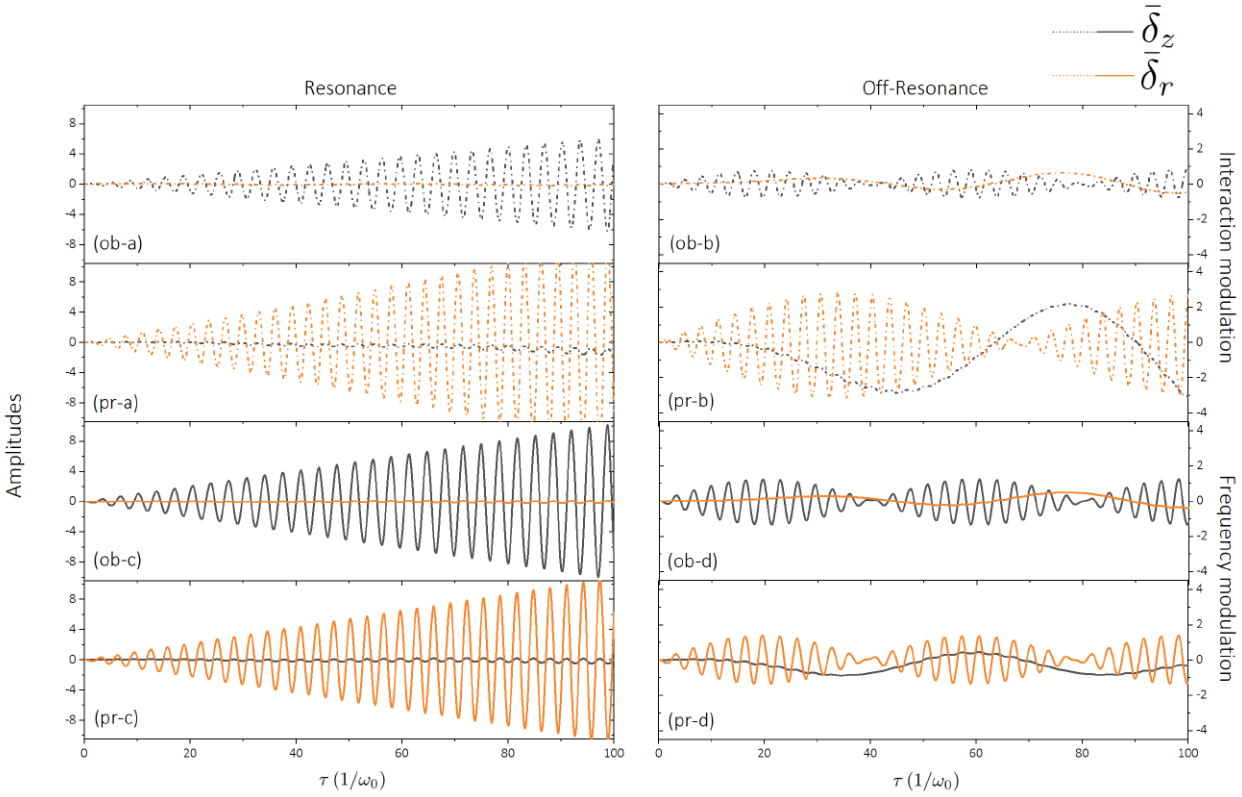

Figure 2.2: The solution to Eqs. (2.30)-(2.32) is presented for two cases: when Ω corresponds to the breathing mode frequency, as determined through variational analysis, and when it is slightly shifted off resonance. Time τ is expressed in units of $\frac{1}{\omega_0}$, where ω_0 is defined as ω_{r0} for the prolate trap and ω_{z0} for the oblate trap. Accordingly, the modulation for the prolate trap is applied at $\Omega = 2.0\omega_r$ in resonance and $\Omega = (1 + 0.1)2.0\omega_r$ slightly off resonance. For the oblate trap, the modulation frequencies are $\Omega = 1.80\omega_z$ in resonance and $\Omega = (1 + 0.1)1.8\omega_z$ off resonance. Subfigure notation (ob-) and (pr-) is used to distinguish between the two trap geometries, with (ob-) referring to the oblate trap and (pr-) to the prolate trap. Subfigures (ob-a), (ob-b), (pr-a), and (pr-b) illustrate the solutions to Eqs.(2.31) and (2.30), corresponding to parametric modulation applied to the axial or radial trap frequency, respectively.

parametric form, it is defined as,

$$\frac{d^2x}{dt^2} + (a - 2q\cos 2t)x = 0, \tag{2.39}$$

where a and q are constant parameters. If $q = 0$ the simple harmonic oscillator equation is recovered, where the oscillator performs free vibrations around the stable equilibrium position $x = 0$. In this sense, the parameter q is interpreted as the amplitude of the parametric modulation.

When $q \neq 0$, and thus, the parametric modulation is present, the behavior of the system can be characterized in two cases: i) if the motion stays bounded, it is said that it is a stable solution, ii) if the motion becomes unbounded, it is an unstable solution. The occurrence of one of these two possibilities depends on the values of the parameters a and q. Both kinds of solutions can be represented graphically in the known stability chart with regions of stability and regions of instability, also known as *tongues*. The called transition curves separate both regions.

By comparing the variational equations (2.30), (2.31), where the parametric modulation is introduced through the radial trap frequency for the prolate trap and through the axial trap frequency for the oblate trap, it is evident that both equations resemble some similarities with the Mathieu equation. In both cases, the equation associated with the direction where the parametric modulation is introduced has the form of a *forced Mathieu equation*, since the right side of the equation is not equal to zero but to a periodic forcing that also introduces the coupling with the other direction.

For the case of the set of variational equations (2.32), where the parametric modulation is introduced through the scattering length, for both axial and radial directions, the expressions have the form of a forced Mathieu equation.

Due to the similarities, a stability chart can be obtained for these cases. Figures 2.3 and 2.4 show the stability chart for the prolate and oblate geometries, respectively. Interestingly, for both types, the frequency of breathing mode modulation exhibits instability after reaching a certain magnitude of amplitude. Thus, as stated, this thesis examines the pattern formation in the density of a BEC. As it will be stated in Chapter 4, the conditions of a and q introduced in the numerical simulation correspond to an unstable solution.

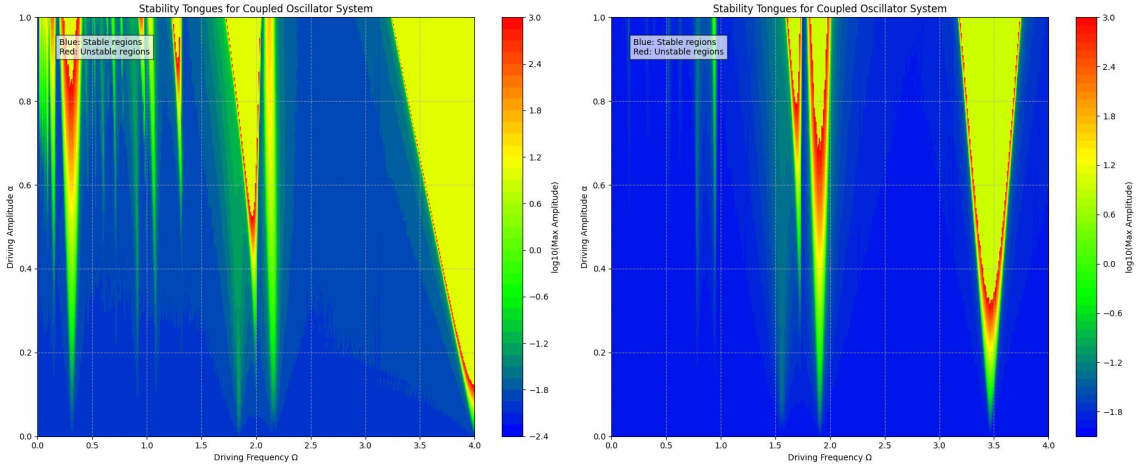

Figure 2.3: Stability chart for a parametric modulated BEC in a prolate trap with a driven frequency Ω in units of ω_r. The left Figure plots the stability chart obtained when the parametric modulation is introduced through the radial trap frequency. The right figure plots the stability chart when the parametric modulation is introduced through the scattering length. As discussed in the text, the variational method demonstrates that the breathing mode has a frequency of $2\omega_r$ for the prolate trap. In these figures, it is demonstrated that for this frequency and beyond a certain value of the amplitude, the solution corresponds to instability.

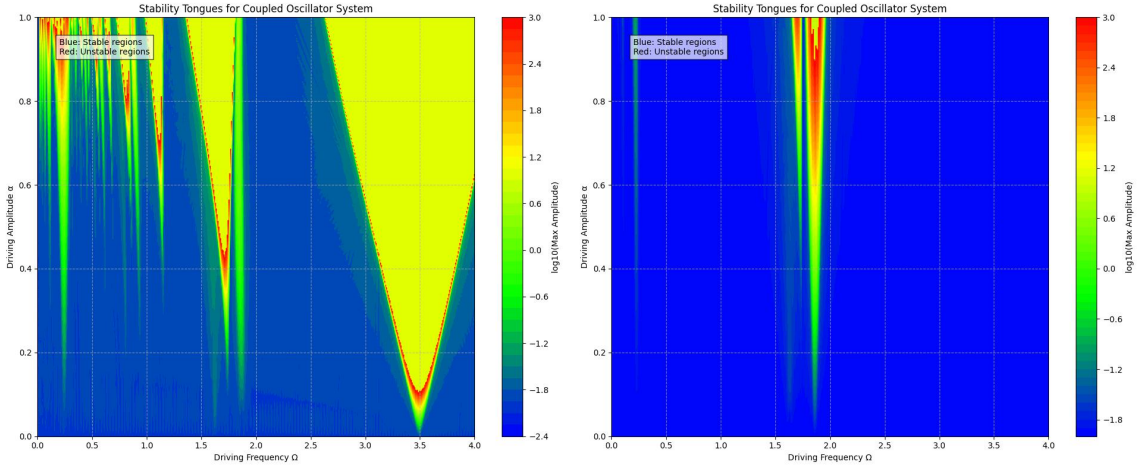

Figure 2.4: Stability chart for a parametric modulated BEC in an oblate trap with a driven frequency Ω in units of ω_z. The left Figure plots the stability chart obtained when the parametric modulation is introduced through the axial trap frequency. The right figure plots the stability chart when the parametric modulation is introduced through the scattering length. As discussed in the text, the variational method demonstrates that the breathing mode has a frequency of $1.80\omega_r$ for the oblate trap. In these figures, it is demonstrated that for this frequency and beyond a certain value of the amplitude, the solution corresponds to instability.

Chapter 3

Experimental Results

3.1 Overview

This chapter discusses the experimental molecular Bose-Einstein Condensate produced in the Ultra-Cold Matter Laboratory (LMU) of the Physics Institute, UNAM. The first section presents the experimental setup that allows the cooling of fermionic ^{6}Li particles up to 100 nK and how parametric modulation can be introduced through the frequencies of the external trap confining the degenerate gas. The second and last sections show how the system responds to external modulation with a collective oscillation that can be measured in the variation of the widths of the atomic cloud.

3.2 Internal Structure

It is important to begin by discussing the fine and hyperfine atomic states to present the techniques employed for cooling atoms. Fine atomic structure arises due to relativistic effects, which are not considered in the non-relativistic quantum mechanics approach. Thus, the analysis is realized using the Dirac equation, which provides the correct relativistic wave equation for electrons.

The fine atomic levels are obtained when the Dirac equation is solved with a Hamiltonian considering three hydrogen atom corrections. The complete Hamiltonian is defined as:

$$\hat{H}_F = \hat{H}_0 + \hat{H}'_1 + \hat{H}'_2 + \hat{H}'_3, \tag{3.1}$$

where $\hat{H}_0$ is the known Hamiltonian for the hydrogen atom given by the kinetic energy of the electron and the Coulomb interaction potential,

$$\hat{H}_0 = \frac{\hat{p}^2}{2m} - \frac{Ze^2}{4\pi\epsilon_0 r}.$$

The corrections are introduced through the terms $\hat{H}_i'$. $\hat{H}_1'$ is a relativistic correction to the kinetic energy, $\hat{H}_2'$ represents the spin-orbit interaction and $\hat{H}_3'$ is known as the Darwin term. They are defined as follows:

$$\hat{H}_1' = -\frac{\hat{p}^4}{8m^3c^2}, \qquad \hat{H}_2' = \frac{1}{2m^2c^2}\frac{1}{r}\frac{dV}{dr}\mathbf{L}\cdot\mathbf{S}, \qquad \hat{H}_3' = \frac{\pi\hbar^2}{2m^2c^2}\left(\frac{Ze^2}{4\pi\epsilon_0}\right)\delta(r)$$

The energy correction due to the presence of these interactions is given by,

$$\Delta E_F = E_n\frac{(Z\alpha)^2}{n^2}\left(\frac{n}{j+1/2}-\frac{3}{4}\right), \tag{3.2}$$

where it can be observed that the correction depends on both the principal quantum number n and the total angular momentum quantum number j, which is obtained by the sum of the orbital angular momentum ℓ and the spin angular momentum s. Additionally, it is in terms of the eigenvalues E_n of the Hamiltonian $\hat{H}_0$.

The fine energy correction (3.2) is of the order of $\sim (Z\alpha)^2$, where α is the fine-structure constant which takes a value of $\sim \frac{1}{137} \approx 0.007$. Thus, this correction is nearly ten thousand smaller than the non-relativistic energy E_n. Although one could think that ΔE_F is too small to be considered, the development of cold-temperature physics ($\sim 100\,\mu K$) requires these high-precision experiments.

Furthermore, for ultracold-temperature experiments ($\sim 100\,nK$) carried out in atomic physics, it is found that the approximation of considering the nuclei as a positive point charge of infinite mass does not explain the observation of the splitting of the electronic levels with an energy usually much smaller than those corresponding to the fine structure. These splittings result from the fact that the nucleus possess an electromagnetic multipole moment which can interact with the electromagnetic field produced at the nucleus by the electrons.

The most important contribution to this multipole moment is given by the magnetic dipole moment, associated with the nuclear angular momentum spin $\mathbf{I}$. This nuclear dipole moment is defined as:

$$\mu_I = g_I\mu_N\mathbf{I}, \tag{3.3}$$

where g_I is a dimensionless number called the nuclear g factor or nuclear Lande factor, and the quantity μ_N is called the nuclear magneton.

The consideration of the nuclear spin $\mathbf{I}$, obliges to define a new operator for the total angular momentum of the system. This is defined as the sum of the orbital angular momentum $\mathbf{L}$, the

electronic spin **S** and the nuclear spin **I**,

$$\mathbf{F} = \mathbf{I} + \mathbf{J} = \mathbf{I} + \mathbf{L} + \mathbf{S}.$$

The eigenvalues of the operator $\mathbf{F}^2$ are given by $F(F+1)\hbar^2$, where F is the new quantum number of the total angular momentum and can take values of

$$F = |I - j|, |I - j| + 1, \cdots, I + j - 1, I + j.$$

Additionally, m_F is defined as the eigenvalue for the projection in F_z. The modification to the electronic levels caused by the presence of the nuclear spin **I** is known as *hyperfine structure* and can be described by a new Hamiltonian:

$$\hat{H}_{HF} = \hat{H}_F + \hat{H}_{MD}.$$

The term $\hat{H}_F$ is the Hamiltonian of the fine structure defined in (3.1) and $\hat{H}_{MD}$ is the correction that considers the interaction of the magnetic dipole moment of the nucleus μ_I with both the orbital angular momentum **L** and the spin **S** of the atomic electron. These corrections can be written as,

$$\hat{H}_{MD} = \frac{\mu_0}{4\pi}\frac{2}{\hbar^2} g_I \mu_B \mu_N \frac{1}{r^3}\left[\mathbf{L}\cdot\mathbf{I} - \mathbf{S}\cdot\mathbf{I} + 3\frac{(\mathbf{S}\cdot\mathbf{r})(\mathbf{I}\cdot\mathbf{r})}{r^2}\right],$$

where μ_B is the Bohr magneton. The energy correction to the electronic states due to this nuclear coupling is of the form:

$$\Delta E_{HF} = \frac{1}{2}\frac{m}{m_p} g_I \frac{Z^3\alpha^2}{n^3}\left(\frac{\mu}{m}\right)^3 \frac{F(F+1) - I(I-1) - j(j+1)}{j(j+1)(2\ell+1)}, \tag{3.4}$$

with m_p as the proton mass and μ being the reduced mass of the electron with respect to the nucleus.

As a brief example of the fine and hyperfine energies, it is found that for the ground state of alkali atoms, these corrections are proportional to:

$$E_F \sim \frac{Z^2}{n^3}\alpha^2 hcE_n, \qquad E_{HF} \sim \frac{Z}{n^3}\frac{m}{m_p}\alpha^2 hcE_n. \tag{3.5}$$

Thus, since E_{HF} scales in terms of $\sim \frac{Z}{m_p}$, the variation in the hyperfine energies are much more smaller than the fine energies.

The importance of considering and understanding these small corrections lies in the fact that transitions between these states are experimentally accessible due to the enhancement in generating

lasers, which have a frequency that matches the fine transitions of the alkali atoms. For example, the fine transitions of the ^{6}Li isotope have a wave-length value of 670 nm or 440 THz in frequency units. These atomic transitions are accessed by a laser with $\lambda = 671$ nm. Subsequently, to match the exact frequencies and to separate into the hyperfine states, special devices known as acousto optic modulators (AOM) are used so that a beam of light with frequency ν is shifted by $\nu \pm f$, with f in the order of hundreds of MHz.

During the cooling process, an external magnetic field is introduced into the atomic cloud. Thus, it is also important to discuss how atomic states are modified due to the presence of a magnetic field, a phenomenon known as the Zeeman Effect. Figure 3.1 shows how the two ground hyperfine states of ^{6}Li split into their m_F projections due to an external magnetic field. The splitting of the energy of the hyperfine levels is given by the Breit-Rabi formula. An analytical expression can be obtained just for the case when the J angular momentum is $J = 1/2$. For higher values of spin, a numerical diagonalization is needed. For the case of the isotope ^{6}Li, $J = 1/2$ and thus, the analytic expression describing the shifting of the energy of the hyperfine values due to the presence of a B magnetic field is given by,

$$E = -\frac{\Delta E_{HF}}{2(2\ell+1)} - g_I \mu_B m_F B \pm \frac{1}{2}\sqrt{\Delta E_{HF}^2 + \frac{4m_F}{2\ell+1}(g_J - g_I)\mu_B B \Delta E_{HF} + (g_J - g_I)^2 \mu_B^2 B^2}$$

For weak magnetic fields, this expression reduces to the pure Zeeman effect, where the splitting of the atomic levels is the same and has a linear behavior. When increasing the magnitude of the magnetic field, the strength of the coupling between **J** and **B** becomes comparable to the strength of the coupling between **L** and **S**, and at some point the coupling between **L** and **S** breaks down, so that the system is no longer characterized by the quantum number J. This regime is known as the Paschen-Back effect and describes the experimental interval where the ^{6}Li experiment is performed.

3.3 Experimental setup

Now the fine and hyperfine corrections have been briefly defined, it is time to discuss the setup of the LMU experiment. The accessible atomic transitions of ^{6}Li used during the cooling process are presented in Figure 3.2. The fine transition D_2 ($2^2S_{1/2} \rightarrow 2^2P_{3/2}$) is employed during several cooling processes. In contrast, the fine transition D_1 ($2^2S_{1/2} \rightarrow 2^2P_{1/2}$) is only used during the

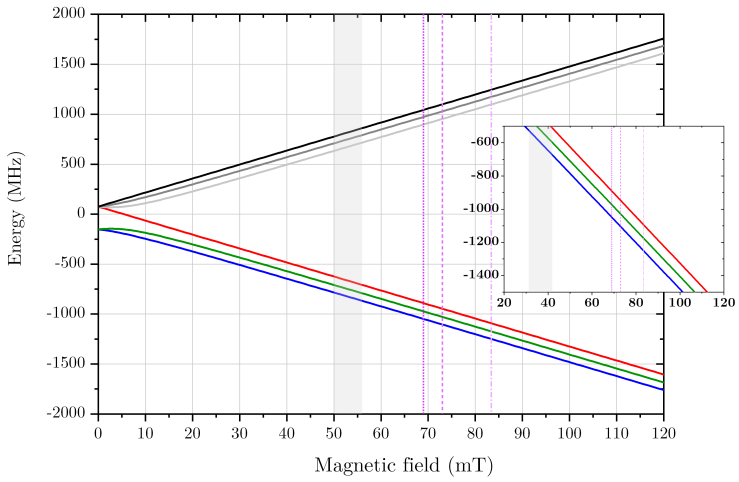

Figure 3.1: Splitting and shifting of the two ground states $2^2S_{1/2}$ of ^{6}Li, with $F = 1/2$ and $F = 3/2$, when an external magnetic field is present. The figure shows how the hyperfine states split in their m_F projections when an external field is present. The hyperfine state with $F = 1/2$ splits into two different states with $m_F = 1/2$ and $m_F = -1/2$ marked as $|1\rangle$ and $|2\rangle$, respectively. The hyperfine ground state with $F = 3/2$ splits into four different states characterized by the projections $m_F = 3/2, 1/2, -1/2, -3/2$ and marked with the $|3\rangle, |4\rangle, |5\rangle$ and $|6\rangle$ states. The energy of each of these projections depends on the magnitude of the external magnetic field. A zoom of the behavior of the first three energy states is plotted on the right side. This zoom enables visualization of the linear behavior of the energy states at higher values of magnetic effects, which is known as the Paschen-Bach effect.

Gray-Molasses process, as will be discussed.

Due to the presence of an external magnetic field, and thus, to the Zeeman effect, it is possible to generate a spin mixture of fermions by splitting the ground hyperfine level, as shown in Figure 3.1. The importance of breaking the degeneration of each of the two hyperfine ground states relies on the fact that a spin mixture is generated. Since ^{6}Li is a fermion, it is necessary for the atoms to be distributed into different states so that interactions can be allowed between them. By splitting the hyperfine state $F = 1/2$ into $m_F = 1/2$ and $m_F = -1/2$, the atomic cloud is naturally populated around 50% on each projected state. The now-allowed interaction will not only be crucial for the last step of the cooling process up to the degenerate gas but also is responsible for forming

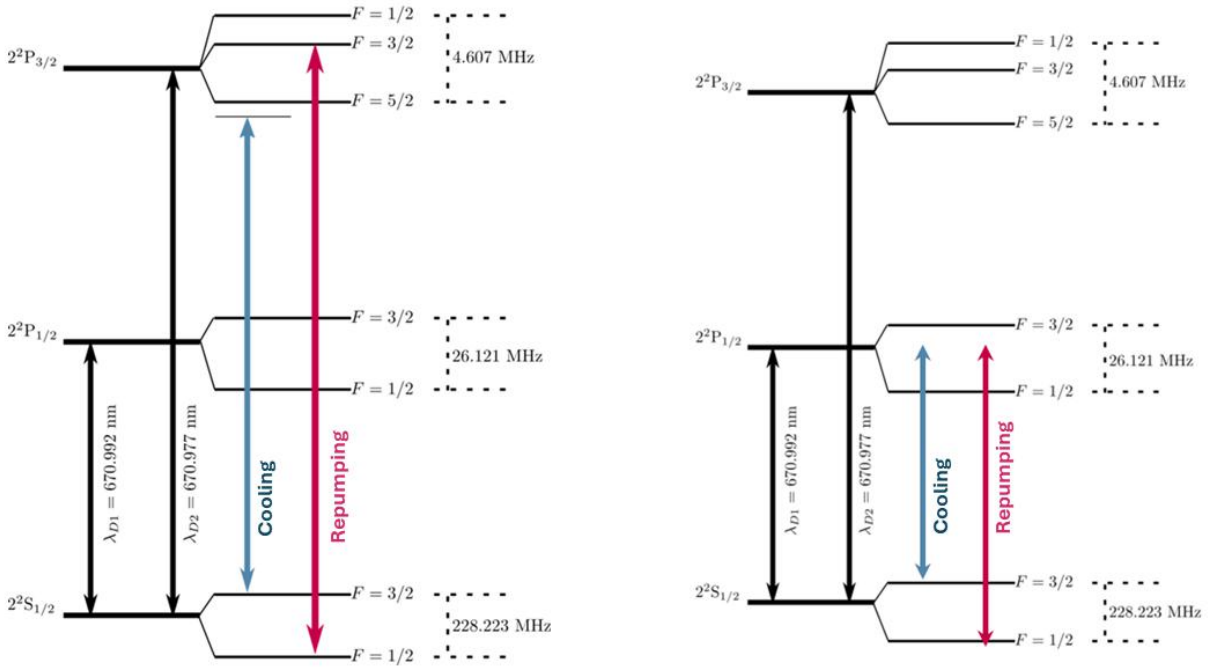

Figure 3.2: Experimentally accessible fine and hyperfine transition of ^{6}Li isotope. The D_1 fine transition is defined between the energetic levels $2^2S_{1/2}$ and $2^2P_{1/2}$. The D_2 fine transition occurs between $2^2S_{1/2}$ and $2^2P_{3/2}$ energetic states. When the presence of the nuclear spin correction is considered, the hyperfine states denoted by the total angular momentum F arise. The figure at the left represents the allowed transitions between the $F = 1/2$ and $F = 3/2$ states of the fine state $2^2S_{1/2}$ and a F state of the excited fine state $2^2P_{1/2}$. Similarly, the right figure represents the allowed hyperfine transitions between the two F ground states and a F excited state of $2^2P_{3/2}$.

bosonic diatomic molecules that are the ones that are carried into condensation. Furthermore, as discussed in Chapter 1, interactions can be controlled via a Feschbach resonance. Precisely, in the ^{6}Li degenerate gas, interactions between $m_F = 1/2$ and $m_F = -1/2$ states are the ones that are controlled and allow to generate a Bose-Einstein Condensate, a Unitary gas or a BCS type system depending on the interaction tunned between particles.

Now that the atomic states of ^{6}Li have been discussed, each of the different cooling processes employed to achieve the quantum degeneration of an atomic gas will be briefly presented.

Zeeman Slower

The Zeeman Slower (Figure 3.3) is the first cooling step realized in the laboratory. During this process, a collimated beam of Li atoms is incident inside a tube 56 cm long. At the same time, but in the opposite direction, a counterpropagating beam of light with a frequency that matches the frequencies of the cooling and repumping processes of the D2 line transition is incident in the same tube. Through an absorption-spontaneous emission process, the photons incident in the tube transmit their momentum to the atoms, causing them to reduce their velocity. In order to maintain the resonance between the atoms and the incident counterpropagating beam of light, it is important to take into account that the atoms are in movement. Thus, the Doppler effect needs to be considered. Experimentally, this can be achieved by an external magnetic field. Furthermore, since the velocity of the atoms is reduced constantly, the magnitude of the magnetic field can not be constant, but it also needs to be modified through the length of the tube. Therefore, a set of coils of different sizes are rolled through the tube so that a gradient in the magnetic field ensures that the resonant condition is satisfied. This resonance condition is established as,

$$\hbar\delta_{\text{Zeeman}} + \hbar k v(z) = \mu_B B_z(z),$$

where δ_{Zeeman} is the detuning of the counterpropagating beam of light to the atoms, $B_z(z)$ is the magnitude of the magnetic field, which is dependent on position z, and $v(z)$ is the velocity of the atoms also depends on position. The Zeeman Slower process reduces the atom's velocity from $\sim$1000 m/s to $\sim$15 m/s, equivalently, from $\sim$670 K to $\sim$150 mK. This huge change in the gas temperature permits the efficient confinement of the atoms in the following processes.

Magneto Optical Trap

Once the atoms leave the Zeeman Slower, they are confined in a magneto-optical trap (MOT) formed by a magnetic field gradient and three counterpropagating beams of light (Figure3.4). The magnetic field gradient is generated with two coils in an anti-Helmholtz configuration, forming a quadrupolar magnetic field. The counterpropagating light beams contain the cooling and repumping frequencies of the D2 fine transition, such as the Zeeman Slower process. In the same absorption-spontaneous emission also presented in the Zeeman Slower, the average velocity of the atoms decreases, as does the temperature of the gas. This process has a duration of a few seconds and is able to reduce the

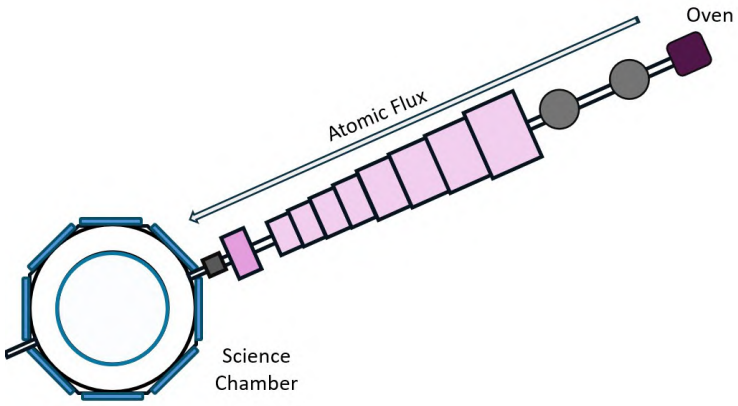

Figure 3.3: Zeeman slower scheme. A collimated atomic beam is introduced through a tube rolled with a set of coils of different sizes in order to create a magnetic field gradient. In the opposite direction, a counterpropagating beam of light with a frequency equal to the D_2 transition line is incident through the same tube. This light-atom interaction, plus the presence of an external magnetic field, generates a cooling mechanism based on the momentum exchange between the photons and the atoms.

temperature to $T \sim 5$ mK.

Optical Molasses

In the optical molasses process, the intensities of the light beams of the MOT are decreased to avoid heating by scattering, and the frequency values of the cooling and repumping transitions are modified until the transition is reached. At the same time, the external magnetic field is turned off abruptly. Through this mechanism, it is possible to reach a temperature of 500μk.

Gray Molasses

The cooling mechanism based on the absorption-spontaneous emission of photons is known as laser cooling and has a limit in the temperature that can be achieved. This limit is known as the Doppler limit and is defined by $T_D = \hbar\Gamma/2k_B = 140.9\mu K$ for the ^{6}Li case. A temperature below this limit can be achieved using a mechanism known as Gray molasses.

In the Gray Molasses method, the counterpropagating light beams with the hyperfine transitions of the D_2 are turned off, and three new counterpropagating beam lights are incident, but this time

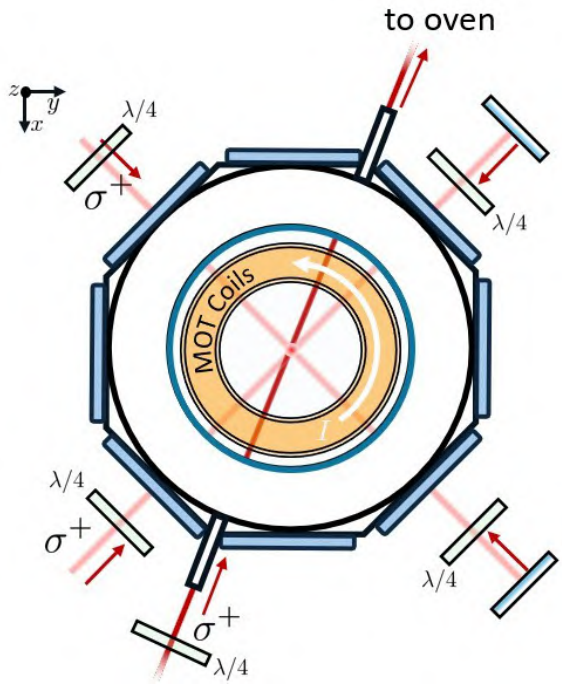

Figure 3.4: Magneto Optical Trap scheme. Three counterpropagating beams are incident in the x, y, and z directions, each one with cooling and repumping frequencies of the D_2 fine transition. The interaction of the atomic cloud, coming from the Zeeman slower, with the three beam lights plus a magnetic field in an anti-Helmholtz configuration decreases the velocity of the atoms and confines them inside the science chamber.

with the cooling and repumping frequencies of the D_1 transition. The cooling of the gas in this process is not achieved by the laser cooling mechanism discussed in the previous steps, where the atoms reduce their velocity by an interchange of momentum with the photons. In contrast, a two-photon process in Λ configuration occurs.

Hyperfine levels of alkali atoms, such as ^{6}Li, can be considered as an effective atom of three levels in Λ configuration. Chapter 6 presents the theoretical treatment of this problem. In this chapter, it is discussed that when diagonalizing the Hamiltonian associated with an effective atom of three levels interacting with a field, three dressed states characterize the system, which are the ones that define the basis where the system is diagonal. Within the dressed states are found dark and bright states. Dark states are characterized because of the lack of interaction with the field and because of having a higher energy. Bright states interact with the field and have less energy.

Transitions between dark and bright states are responsible for the cooling mechanism of gray molasses. The probability of transition between a dark and a bright state depends on the square of the linear momentum of the atoms. Thus, the transition probability from a dark state (higher energy) to a bright state (lower energy) will be lower at higher temperatures. Additionally, the counterpropagating beam laser of the D1 transitions needs to have a circular polarization to create a polarization gradient that allows the generation of a mechanism known as *Sisyphus*. In this, atoms go from the dark to the bright state, reducing their momentum and probability of being excited again to the dark state.

Once the atoms reach the sub-Doppler temperature ($\sim 50\,\mu$K) with this mechanism, a procedure known as *optical pumping* is performed where the final states of the atoms are chosen. In the LMU experiment, the ^{6}Li atoms end in the hyperfine state with F=1/2 at the end of the gray molasses. The low temperature achieved in this step allows the transfer of the atomic cloud to a conservative trap.

Conservative Trap (ODT)

Evaporative cooling, the last step for achieving the degeneration temperature, is performed in a conservative trap (Figure 3.5). There are different types of conservative traps, but in the LMU experiment, it is formed by an Optical Dipole Trap (ODT) and a magnetic curvature. The ODT confines the atom in the radial direction, while the magnetic curvature confines it in the axial direction.

Transferring the atoms to the conservative trap is a very important step that needs to be optimized to reduce the loss of atoms during the transfer. This process consists of turning on a laser beam of 1069 nm, which is very far from the atomic frequencies involved during the experiment. Since the detuning of the laser beam is shifted to the red in comparison with the frequencies of the atomic transitions, the interactions of the atomic cloud with this electromagnetic field are reduced to attractive interactions that confine the atoms in the focus of the laser beam.

The laser is turned on up to 180 W in 11 ms, looking that the beam is aligned with the center of the atomic cloud. Once the power of the laser beam is at its maximum, a magnetic field (Feshbach field) is switched on at 832 G. The magnitude of the introduced Feshbach field corresponds to the unitary limit, where the dispersion length diverges, implying that the rate collision between atoms

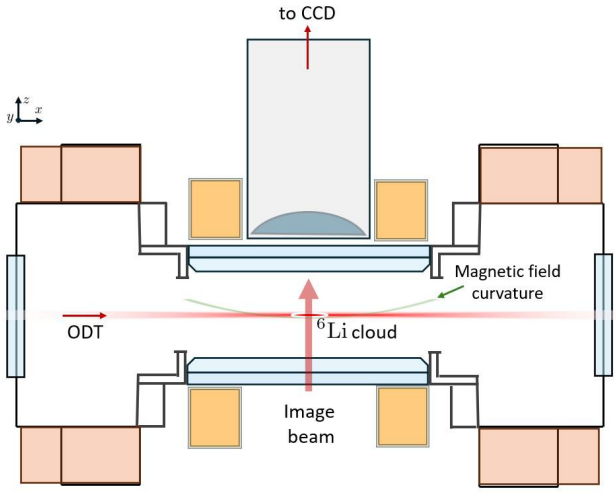

Figure 3.5: Conservative trap scheme. An Optical Dipole Trap (ODT) confines the atoms in the radial direction, and a magnetic curvature confines them in the axial direction. The ODT is formed by a laser beam of 1069 nm, which is very far from the atomic frequencies involved in the experiment. This far-red detuning induces an attractive dipole force to the atoms that confine them in the focus of the laser beam.

is maximum. These collisions make efficient the process of rethermalization during the evaporative cooling step.

Moreover, due to the presence of the Feshbach field, the hyperfine atomic levels break their degeneracy and are split in their projections characterized by the quantum number m_F. As mentioned before, at this point, the atoms populate the hyperfine state $F = 1/2$. Thus, when the Feshbach magnetic field is switched on, the atoms redistribute into the projected states $m_F = 1/2$ and $m_F = -1/2$. If this process is realized adiabatically, both m_F states are populated almost equally, creating a balanced spin mixture that allows the interaction between fermions, which eventually will generate a superfluid when the critical temperature is reached.

Evaporative Cooling

The evaporative cooling process consists of reducing the power of the ODT at a magnitude of 832 G for the Feshbach magnetic field. By decreasing the ODT's power, the potential depth decreases as well, causing the loss of the atoms at higher temperatures (Figure 3.6). The collision between atoms allows the process of thermalization, decreasing the temperature of the system.

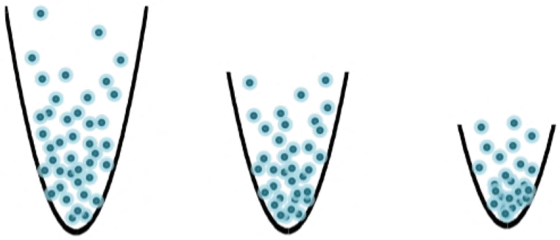

Figure 3.6: Evaporative cooling process. The intensity of the ODT is reduced, decreasing the depth of the potential causing the lost of the atoms with higher energy. As a consequence the temperature of the atomic cloud decreases.

Finally, a diagram of the complete experimental sequence is presented in Figure 3.7. In it, it is possible to visualize the cooling processes that are carried out, as well as the optical and magnetic fields present in each step. Additionally, the temperature of the system and the number of pairs are represented at each step to visualize how they change throughout the experimental sequence.

3.4 Experimental Observation of Collective Excitations

As previously discussed, the harmonic frequencies of the optical dipole trap are related to the beam's power by the relation $\omega_k \sim \sqrt{P}$. Thus, by any power modifications, it is possible to introduce a modulation in the system and study how it responds.

Figure 3.8 shows how the radial width of the atomic cloud oscillates with a frequency equal to $2 \cdot \omega_r$, where ω_r is the radial frequency of the trap. This collective response is called breathing mode. Figure 3.9 shows how when the system is modulated by the breathing mode, a fringe pattern is created over the BEC density confined in a cigar-shaped trap. This observation, characterized at the LMU and completely reported in reference [41], motivated the study of the modulation of a BEC confined in an oblate trap. The results are presented in the following chapter.

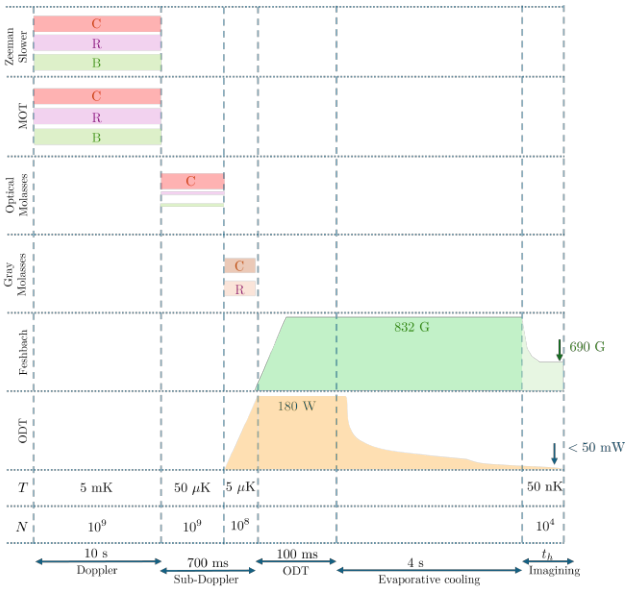

Figure 3.7: The experimental sequence of the cooling process is represented in this diagram, as well as the change in the T temperature of the system and the number of pairs N. The sequence begins with the Zeeman Slower and ends with the ODT. The red fringe with the "C" letter denotes the presence of the cooling optical beam. Similarly, the pink fringe with the "R" letter represents the presence of the repumping optical beam, and the green fringe with the "B" letter denotes a magnetic field used to compensate for the Doppler effect during the Zeeman Slower and to confine the atoms in the MOT. Additionally, it is demonstrated when the Feshnach field is turned on and off, as well as at what magnitude. Finally, the power of the ODT is represented in the final steps.

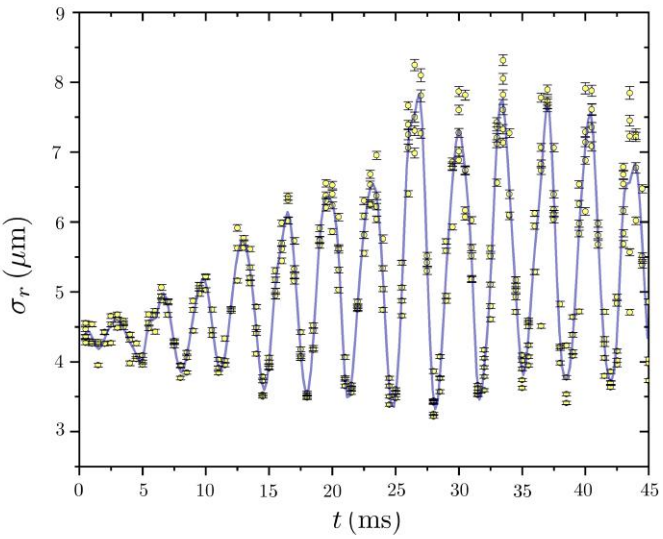

Figure 3.8: Oscillations of the radial width of the atomic cloud characterizing the breathing mode are shown for a cylindrical symmetric harmonic trap with frequencies $\omega_r = 2\pi \times 163$ Hz and $\omega_z = 2\pi \times 11$ Hz. The oscillating atomic sample contains 5×10^4 pairs.

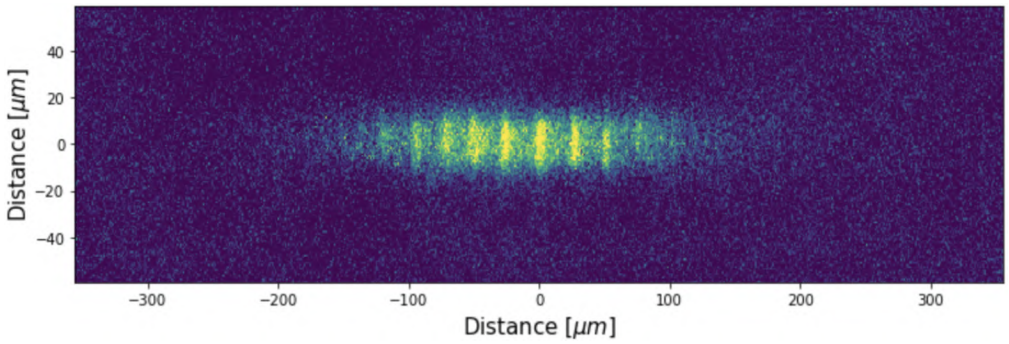

Figure 3.9: A fringe pattern is generated over a cigar-shaped BEC's density when modulated in the axial direction with the breathing mode frequency at a field of 690 G. The reached temperature corresponds to $T/T_F = 0.1$, where T_F is the Fermi temperature. The sample contains 5×10^4 pairs in a cylindrical symmetric harmonic trap with frequencies $\omega_r = 2\pi \times 163$ Hz and $\omega_z = 2\pi \times 11$ Hz.

Chapter 4

Numerical Simulation of the GPE

4.1 Overview

In this chapter, the results obtained by the variational method are used in the numerical simulation of a parametrically driven Bose-Einstein condensate confined in a cylindrical harmonic trap. The simulation is carried out under two different geometries: i) prolate (cigar-shaped) trap and ii) oblate (pancake-shaped) trap. The parametric excitation is introduced in two different forms to study the difference in the system evolution: i) by the modulation of one of the harmonic frequencies and ii) by the modulation of the interatomic interaction strength. The modulation frequency matches the system's breathing mode frequency (obtained by the variational method).

As a result, the formation of dynamical density patterns that depend on the geometry of the trap are observed. For the prolate system, fringe patterns arise, and for the oblate geometry, ring patterns are observed. By decomposing the total energy into its kinetic, potential, and interaction terms, it is found that the onset of these patterns coincides with the redistribution of kinetic energy along the weakly trapped directions of the sample, indicating the three-dimensional nature of the studied phenomena. Finally, the analysis shows that the difference between the two excitation mechanisms lies in the stability of the system. Modulating the trap destabilizes the system quicker than modulating the interactions, leading to the earlier formation of the patterns.

This chapter is divided into two sections: i) Numerical Simulation, where the details of the numerical simulation and the implemented method are discussed, and ii) Analysis of Results, where the density and wave functions obtained by the numerical simulation are analyzed through different functions.

The results presented in this chapter have been reported on reference [43].

4.2 Numerical Simulation

The three-dimensional GPE discussed in Chapter 2 is solved numerically for a molecular Bose-Einstein Condensate of ^{6}Li by considering a parametric modulation through one trap frequency or the molecular scattering length $a_M(t)$. Therefore, the external potential and the interaction term are time-dependent,

$$(\imath - \gamma_d)\hbar\frac{\partial}{\partial t}\Psi(\mathbf{r},t) = \left(-\frac{\hbar^2}{2M}\nabla^2 + V_{\text{ext}}(\mathbf{r},t) + \frac{4\pi\hbar^2 a_M(t)}{M}|\Psi(\mathbf{r},t)|^2\right)\Psi(\mathbf{r},t), \tag{4.1}$$

where the trapping potential $V_{\text{ext}}(\mathbf{r},t)$ is defined in (2.21). The temporal periodical dependence of $V_{\text{ext}}(\mathbf{r},t)$ is introduced through one of the trap frequencies as presented in (2.22). For a prolate trap, the radial frequency $\omega_r(t)$ is modulated, while for the oblate trap, the axial frequency $\omega_z(t)$ is modulated. Similarly, the temporal dependence of the scattering length is defined in (2.23). However, instead of considering the scattering length $a_s(t)$ defined for a single atom, in equation (4.1), this quantity is replaced by $a_M(t)$, which refers to the scattering length between the diatomic molecules. The case in which both quantities are modulated simultaneously, V_{ext} and a_M, is not considered; the system is excited by modulating only one of them.

The trap frequencies in each geometry configuration (prolate and oblate) are settled close to experimental values or within the ranges of technical accessibility. At $t = 0$, when no modulation is applied, the oblate trap frequencies are given by $\omega_{r0} = 2\pi \times 10$ Hz and $\omega_{z0} = 2\pi \times 150$ Hz. For the prolate trap, the frequencies of the initial configuration are $\omega_{r0} = 2\pi \times 150$ Hz and $\omega_{z0} = 2\pi \times 15$ Hz. The effective scattering length between the bosonic molecules is given by $a_{M0} = 0.6 \times a_{s0}$ [52], where $a_{s0} = 1500a_0$ is the scattering length between the fermionic isotopes of ^{6}Li. The number of pairs is fixed to $N = 5 \times 10^4$.

For these experimental parameters, the dimensionless interaction strength η, discussed in Chapter 1, is given by $\eta = 1.38$ for the prolate trap and $\eta = 2.32$ for the oblate trap. The excitation frequency Ω is $\Omega = 2\omega_r$ for the prolate trap and $\Omega = 1.80\omega_z$ for the oblate trap, as it was found by the variational method in Chapter 2.

The dimensionless variables introduced for solving the GPE are defined in the same way as in Chapter 2 in equations (2.26), where the harmonic oscillator length l_0 is defined through the most confining trap frequency ω_0, equal to ω_z (ω_r) in the oblate (prolate) geometry.

All the simulations were performed using Google's Colab Pro cloud GPU in CUDA language.

Equation (4.1) was solved through the *Time Split Step Fourier Method* (TSSF) [65–67], which decomposes the Hamiltonian of the GP equation into two parts. One which is only in terms of the momentum operator and the other which depends only on the position operator. Therefore, equation (4.1) can be rewritten as,

$$\imath\frac{\partial\Psi}{\partial t} = (\hat{A}+\hat{B})\Psi, \tag{4.2}$$

where the γ_d parameter has been omitted just for simplicity, and operators $\hat{A}$ and $\hat{B}$ are defined as follows:

$$\hat{A} = -\frac{\hbar}{2M}\nabla^2\,, \qquad \hat{B} = \frac{1}{\hbar}\left(V_{\text{ext}}(\mathbf{r},t) + \frac{4\pi\hbar^2 a_M(t)}{M}|\Psi(\mathbf{r},t)|^2\right).$$

As will be shown, by separating the operators of momentum and position, the wave function can evolve alternately in momentum and real space.

The action of the unitary time evolution operator gives the time evolution of the wave function of the system,

$$\Psi(\mathbf{r},t+dt) = \hat{U}(t+dt,t)\Psi(\mathbf{r},t), \qquad \hat{U}(t+dt,t) = \exp\left[-\imath\int_t^{t+dt}(\hat{A}(\tau)+\hat{B}(\tau))d\tau\right]. \tag{4.3}$$

Given the definition of $\hat{A}$ and $\hat{B}$, the last expression simplifies to

$$\Psi(\mathbf{r},t+dt) = \mathrm{e}^{-\imath\hat{A}dt-\imath\int_t^{t+dt}\hat{B}(\tau)d\tau}\Psi(\mathbf{r},t) = \mathrm{e}^{-\imath\hat{A}dt-\imath\tilde{\hat{B}}(t)}. \tag{4.4}$$

Operators $\hat{A}$ and $\tilde{\hat{B}}$ do not commute, however for evaluating their action over the initial wave function, the exponential can be approximated as,

$$\mathrm{e}^{-\imath\hat{A}dt-\imath\tilde{\hat{B}}(t)} \approx \exp\left(-\frac{\imath}{2}\tilde{\hat{B}}(t)\right)\exp\left(-\imath\hat{A}dt\right)\exp\left(-\frac{\imath}{2}\tilde{\hat{B}}(t)\right). \tag{4.5}$$

Now, it is possible to evaluate the separate action of $\hat{A}$ and $\hat{B}$ on the initial wave function. The action of operator $\hat{B}$ is given by the integral,

$$\exp\left[-\frac{\imath}{2}\tilde{\hat{B}}(t_m)\right]\Psi(\mathbf{r},t_m) = \exp\left[-\frac{\imath}{2}\int_{t_m}^{t_m+dt}\left(V_{\text{ext}}(\mathbf{r},\tau)+\frac{4\pi\hbar^2 a_M(\tau)}{M}|\Psi(\mathbf{r},\tau)|^2\right)d\tau\right]\Psi(\mathbf{r},t_m).$$

However, equation (4.2) leaves invariant $|\Psi|$ in t, for t in $[t_m, t_m+dt]$. Thus, the integral can be rewritten as,

$$\exp\left[-\frac{\imath}{2}\tilde{\hat{B}}(t_m)\right]\Psi(\mathbf{r},t_m) = \exp\left[-\frac{\imath}{2}\int_{t_m}^{t_m+dt}\left(V_{\text{ext}}(\mathbf{r},\tau)+\frac{4\pi\hbar^2 a_M(\tau)}{M}|\Psi(\mathbf{r},t_m)|^2\right)d\tau\right]\Psi(\mathbf{r},t_m),$$

with V_{ext} and a_M as only the time-dependent terms.

Finally, the action of the operator $\hat{A}$ over the initial wave function is better understood in the momentum space since $\hat{A}$ is diagonal on this basis. Thus, it is convenient to act $\hat{A}$, as

$$\exp\left[-\imath\hat{A}dt\right]\Psi(\mathbf{r},t_m)=\mathcal{F}^{-1}\left\{\mathrm{e}^{\frac{-\imath\hbar}{2m}(k_x^2+k_y^2+k_z^2)dt}\mathcal{F}\left\{\Psi(\mathbf{r},t_m)\right\}\right\},$$

where $\mathcal{F}\{\Psi(\mathbf{r},t_m)\}$ is the Fourier Transform of the wave function and the notation $\mathcal{F}^{-1}$ stands for the Inverse Fourier Transform so that the final results stay in the real space.

For solving the differential equation and due to the cylindrical geometry of the system, the simulations for the prolate trap were performed with a $256\times256\times1024$ grid with a resolution of $h=0.5\times10^{-6}$ m and steps of $dr=0.5\cdot h$ and $dz=h$. For the oblate trap, a $512\times512\times256$ grid was implemented with a space resolution of $dr=h$ and $dz=0.5\cdot h$. These parameters guaranteed a good spatial resolution for the problem once it was normalized with the length of the oscillator corresponding to each of the considered geometries.

The temporal resolution was defined in terms of the excitation frequency Ω. For this, the simulation time is considered proportional to the number of cycles N_Ω where the parametric excitation is introduced. In this form, the total excitation time is given by $T_{\text{exc}}=2\cdot\pi N_\Omega/\Omega$. The time step is taken as $dt=T_{\text{exc}}/2^{13}$ and excitation times around 250 ms and 200 ms were considered for the prolate and oblate traps, respectively, both with time steps in the order of $dt=0.4\mu s$. The excitation times T_{exc} were chosen to be long enough to allow the system to evolve and study the dynamics of interest, for short enough so that the condition $\delta_h\ll\sigma_{h0}$, used in the linearization of the system, remains valid.

4.3 Analysis of Results

This subsection discusses the numerical results obtained by solving (4.1). The data analyzed is obtained by solving the system in four different configurations: i) prolate trap parametrically modulated through the radial trap frequency, ii) prolate trap parametrically modulated through the scattering length, iii) oblate trap parametrically modulated through the axial trap frequency, and iv) oblate trap parametrically modulated through the scattering length. To understand the pattern arising, the total energy is decomposed in its kinetic, potential, and interaction contributions. In addition, these energy terms are separated into the radial and axial components. The behavior of the energy terms is matched with the patterns observed over the 2D integrated density of the

condensate. Also, the density current is computed to observe the changes that the system presents when the parametric modulation is introduced. Finally, through the definition of a fidelity function, the temporal periodicity of the patterns and their lifetimes are obtained.

4.3.1 Energy Distributions

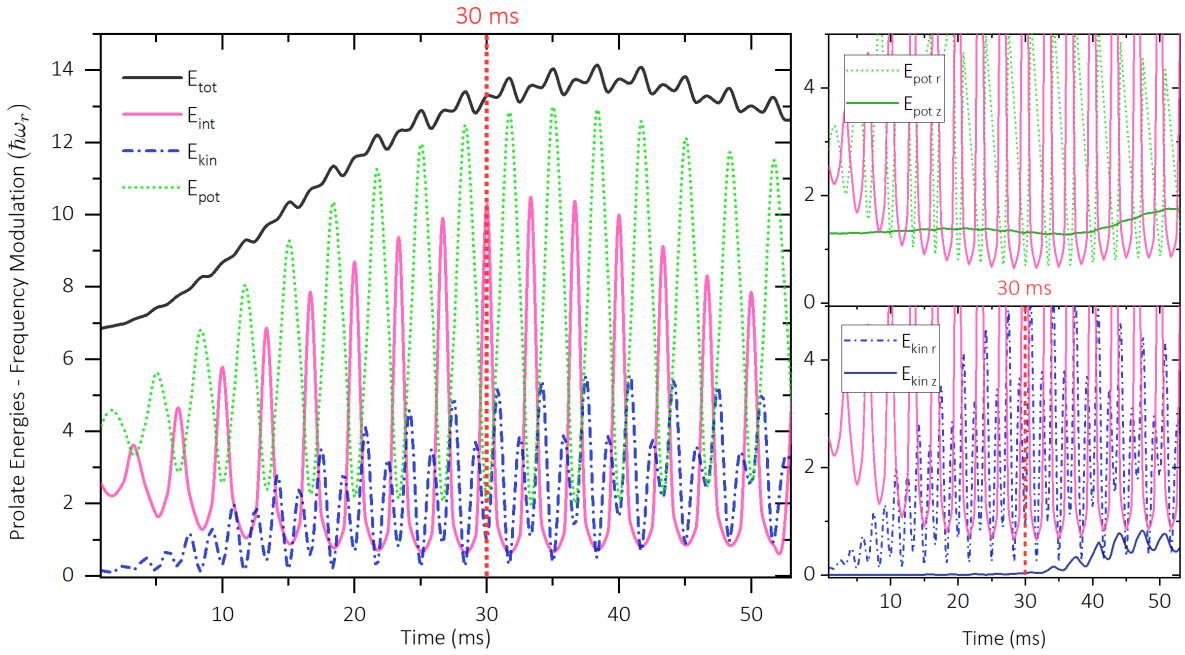

Figure 4.1: The evolution of system energies in a prolate trap is analyzed under radial trap frequency modulation at $\Omega = 2.0, \omega_r$. The plotted energies are expressed in units of $\hbar\omega_r$. As the system undergoes modulation, the total energy increases, with the dominant contributions arising from Epot and Eint. The decomposition into axial and radial components reveals that Ekin, z remains nearly zero at the onset of modulation but begins to rise after 30 ms. This increase coincides with a decline in Etot, leading to system stabilization, as indicated by the vertical dashed line. Consequently, the redistribution of energy between axial and radial modes serves as a mechanism for stabilizing the system.

The total energy of the system is given by

$$\mathcal{E}(t) = \int d^3r \, \{ \underbrace{\frac{\hbar}{2M} |\nabla\Psi(\mathbf{r},t)|^2}_{\mathrm{E_{kin}}} + \underbrace{V_{\mathrm{ext}}(\mathbf{r},t)\,|\Psi(\mathbf{r},t)|^2}_{\mathrm{E_{pot}}} + \underbrace{\frac{1}{2}g(t)\,|\Psi(\mathbf{r},t)|^4}_{\mathrm{E_{int}}} \}\,, \tag{4.6}$$

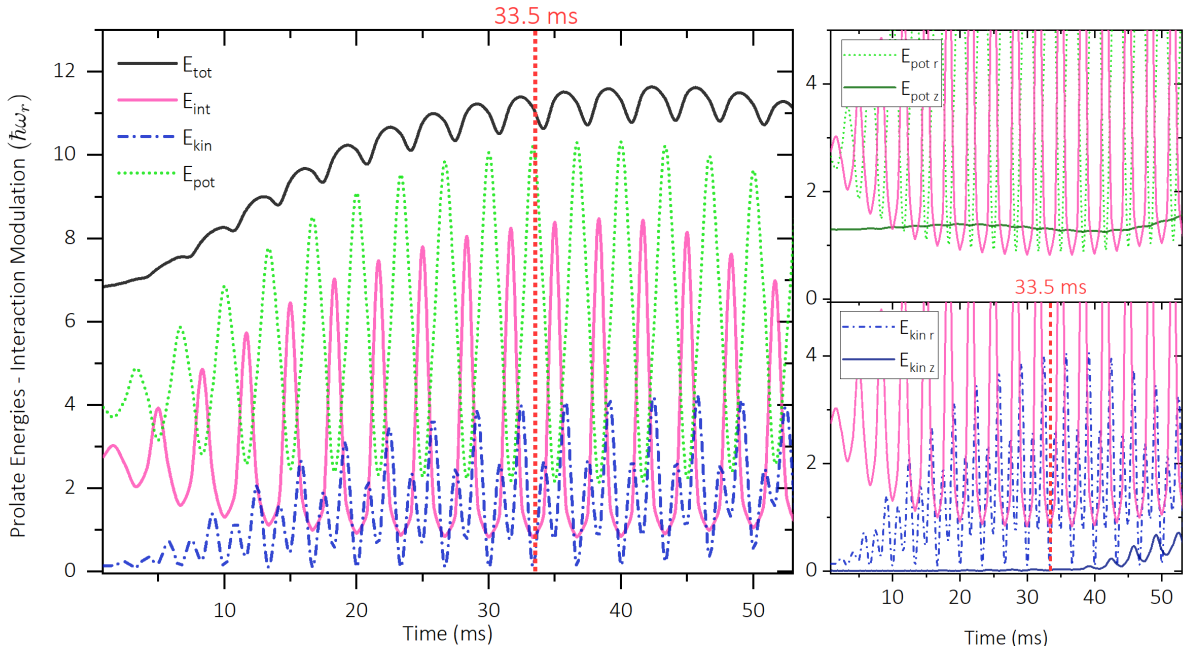

Figure 4.2: The evolution of system energies in a prolate trap is analyzed under scattering length modulation with frequency $\Omega = 2.0, \omega_r$. The plotted energies are expressed in units of $\hbar\omega_r$. As a result of parametric modulation, an overall increase in total energy is observed, primarily driven by contributions from Epot. Unlike modulation through radial frequency, where distinct energy variations occur, Ekin and Eint maintain similar values. The decomposition into axial and radial components reveals that Ekin, z begins to rise after 40 ms, at which point E_{tot} stabilizes, ceasing further growth, as indicated by the vertical dashed line.

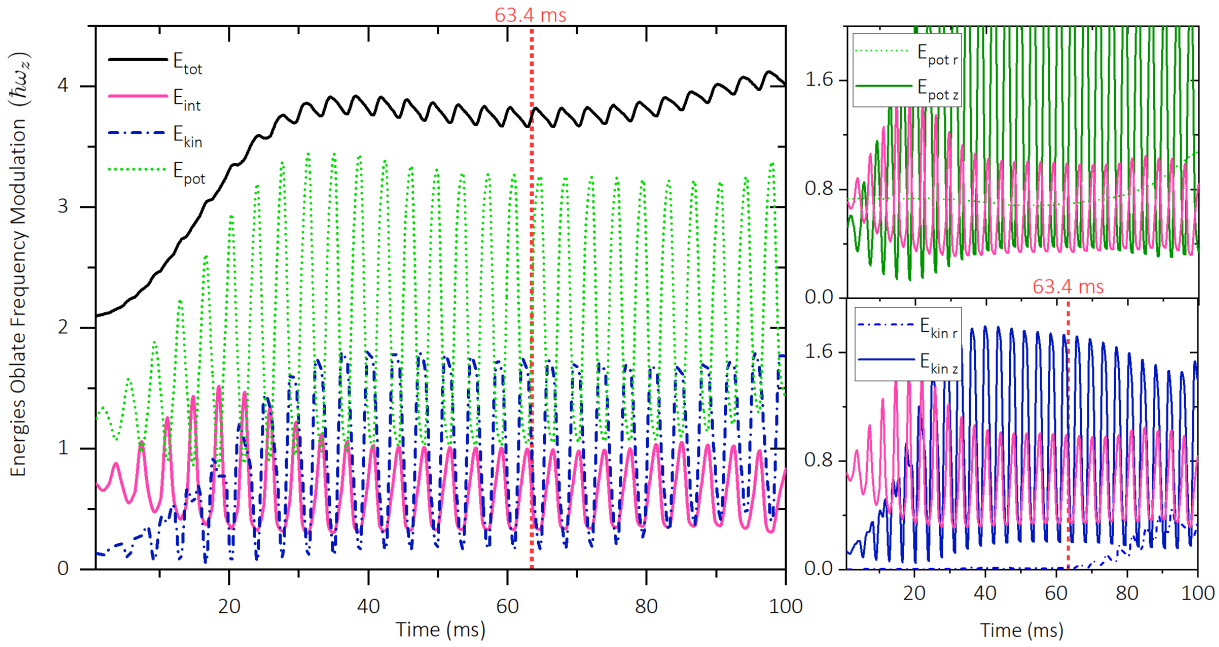

Figure 4.3: The evolution of system energies in an oblate trap is examined under axial trap frequency modulation at $\Omega = 1.80, \omega_z$. The plotted energies are expressed in units of $\hbar\omega_z$. As a result of parametric modulation, the total energy of the system increases, with Epot being the dominant contributing factor. The decomposition into axial and radial components reveals that Ekin, r remains nearly zero at the onset of modulation but begins to rise after 60 ms, as marked by the vertical dashed line. Unlike the case of a prolate trap with radial modulation, where energy redistribution leads to stabilization, here the total energy continues to rise without decreasing.

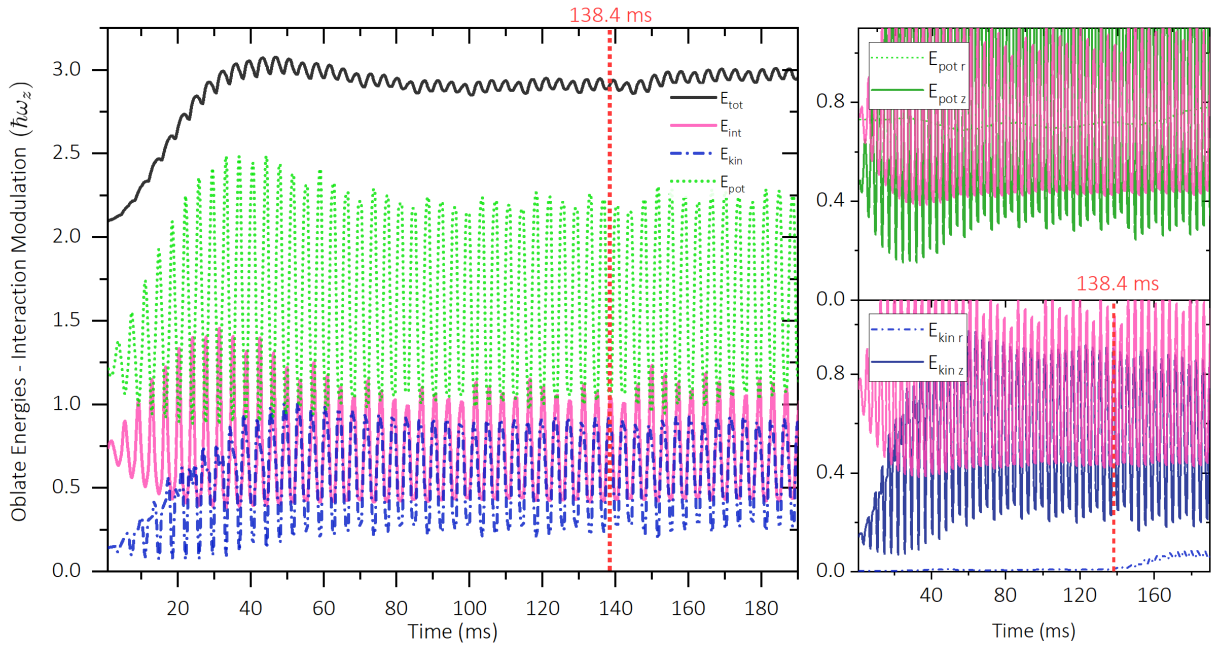

Figure 4.4: The evolution of system energies in an oblate trap is examined under the scattering length modulation at $\Omega = 1.80, \omega_z$. The plotted energies are expressed in units of $\hbar\omega_z$. As a result of parametric modulation, the total energy of the system increases, with Epot being the primary contributing factor. Unlike modulation through radial frequency, Ekin and Eint exhibit similar values throughout the process. The decomposition into axial and radial components reveals that Ekin, r begins to rise after 140 ms, while E_{tot} continues to increase without decreasing, as marked by the vertical dashed line.

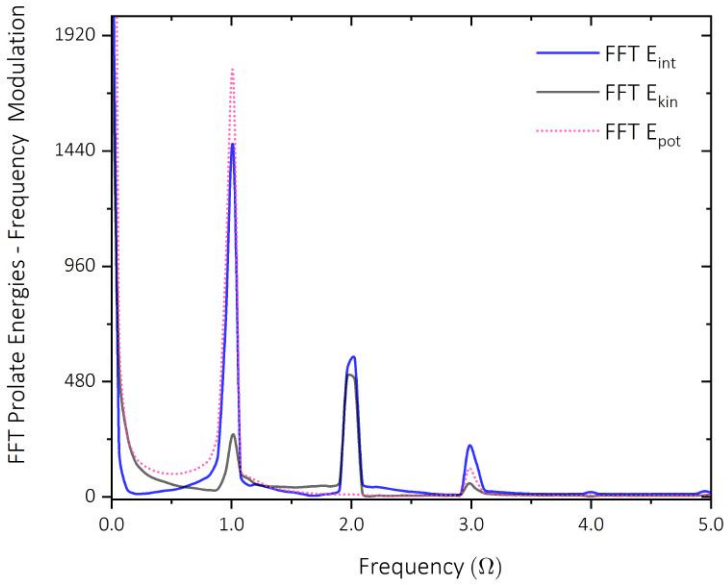

Figure 4.5: The Fast Fourier Transform (FFT) of the energy terms in (4.6) is computed for a prolate trap subjected to parametric modulation via the radial trap frequency. The x-axis represents the modulation frequency, given in units of $\Omega = 2.0, \omega_r$. The results indicate that Eint and Epot primarily oscillate at a frequency equal to Ω, whereas $\mathrm{E_{kin}}$ exhibits dominant oscillations at 2Ω.

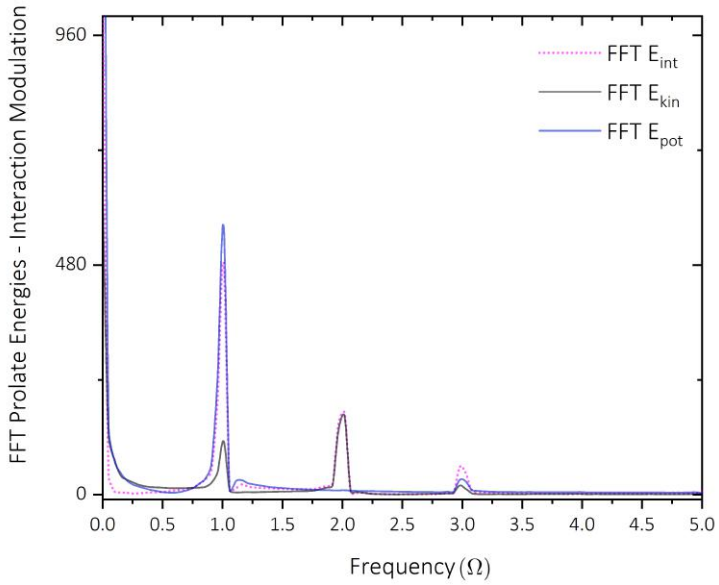

Figure 4.6: The Fast Fourier Transform (FFT) of the energy terms in (4.6) is computed for a prolate trap subjected to parametric modulation via the scattering length. The x-axis represents the modulation frequency, expressed in units of $\Omega = 2.0, \omega_r$. In this case, all energy terms predominantly oscillate at a frequency equal to Ω.

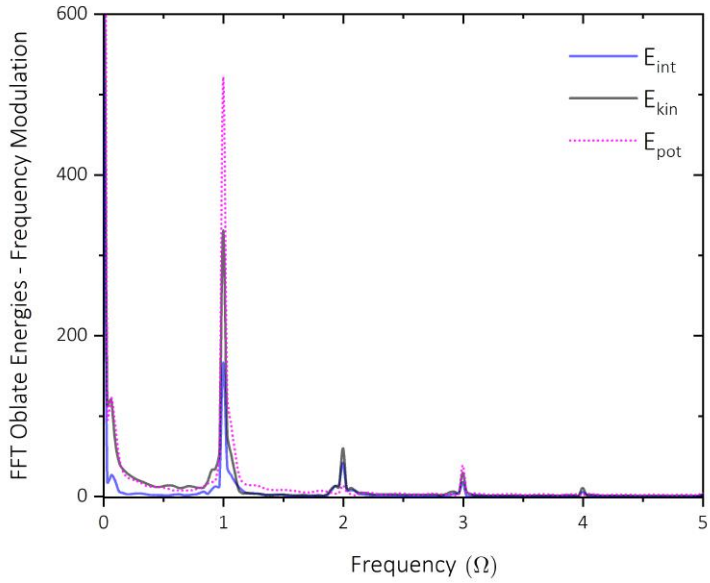

Figure 4.7: The Fast Fourier Transform (FFT) of the energy terms in (4.6) is computed for an oblate trap subjected to parametric modulation via the axial trap frequency. The x-axis represents the modulation frequency, expressed in units of $\Omega = 1.80, \omega_z$. The results indicate that $\mathrm{E_{int}}$, $\mathrm{E_{pot}}$, and $\mathrm{E_{kin}}$ predominantly oscillate at a frequency equal to Ω.

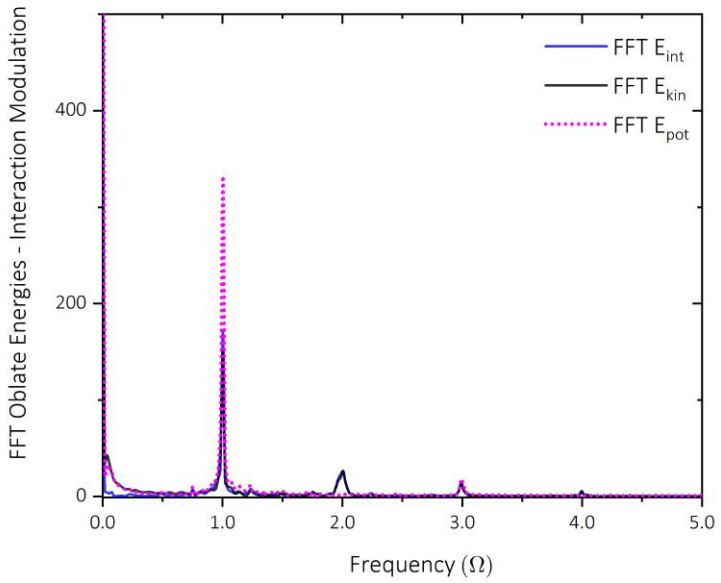

Figure 4.8: The Fast Fourier Transform (FFT) of the energy terms in (4.6) is computed for an oblate trap subjected to parametric modulation via the scattering length. The x-axis represents the modulation frequency, expressed in units of $\Omega = 1.80, \omega_z$. The results indicate that $\mathrm{E_{int}}$, $\mathrm{E_{pot}}$, and $\mathrm{E_{kin}}$ predominantly oscillate at a frequency equal to Ω.

where the time-dependent functions $V_{\text{ext}}(\mathbf{r}, t)$ and $g(t)$ are defined in (2.22) and (2.23), and represent the parametric modulation in one of the trap frequencies (radial frequency $\omega_r(t)$ for the prolate trap or axial frequency $\omega_z(t)$ for the oblate trap) or in the interaction.

The analysis begins with a comparison of the relative contributions of kinetic energy (E_{kin}), potential energy (E_{pot}), and interaction energy (E_{int}). Figures 4.1 and 4.2 illustrate the decomposition of the total energy for a prolate geometry under parametric driving applied via radial frequency and scattering length, respectively. Similarly, Figures 4.3 and 4.4 present the corresponding energy decomposition for an oblate trap with parametric modulation in the axial trap frequency and scattering length, respectively. In all these four cases, the dominant contribution to the total energy is given by the external potential energy term, which is determined by the trap frequencies that confine the quantum gas. At $t = 0$, this contribution reflects the energy range imposed by the confinement, i.e., a more confining trap results in a higher potential energy contribution.

Furthermore, in the absence of parametric modulation ($t = 0$), the system satisfies the Thomas-Fermi approximation, wherein the interaction energy exceeds the kinetic energy. However, this regime is disrupted once the modulation is initiated, leading to a comparable magnitude between the kinetic and interaction energies.

A common feature observed across the four configurations (geometries and parametric modulations) lies in the axial and radial decomposition of the energy terms. Specifically, the potential and kinetic energy associated with the most confined direction (the radial direction in prolate traps and the axial direction in oblate traps) exhibit higher magnitudes than those in the perpendicular directions. Conversely, the energy components along the less confined directions (the axial direction for the prolate trap and the radial direction for the oblate trap) remain nearly unchanged. For example, the kinetic energy E_{kin} along the elongated axis is nearly negligible in both geometries. However, since the parametric modulation continuously introduces energy to the atomic cloud, the system gets saturated at some point, inducing an energy redistribution mechanism to stabilize the system. This stabilization involves transferring energy to the less confining directions. Therefore, an increase in the kinetic and potential energies is observed along the axial direction in the prolate trap (Figures 4.1 and 4.2) and along the radial direction in the oblate trap (Figures 4.3 and 4.4). Notably, in the case of the prolate trap, this energy redistribution is accompanied by a reduction in the total energy. However, for the oblate trap, no such decrease in total energy E_{tot} is observed;

instead, the total energy stabilizes.

The parametric modulation type and the trap geometry influence the time at which this redistribution occurs. For the same geometry (prolate or oblate), the increase of the kinetic component in the less confined direction appears sooner when the parametric modulation is introduced through one of the trap frequencies. In the energy decomposition of the prolate trap, we observe that for the frequency modulation (right subfigures in Figure 4.1), the kinetic energy in the axial coordinate increases after 30 ms, while for the scattering modulation (right subfigures in Figure 4.2), this increase is observed after 40 ms. For the oblate trap, the kinetic energy in the radial trap increases after 70 ms for the axial modulation (Figure 4.3) and after 140 ms for the scattering length modulation (Figure 4.4).

Another distinction between the two parametric modulation types lies in the total energy transferred to the system. Modulation applied through a single trap frequency results in higher energy values within the system. This phenomenon can be attributed to the direct introduction of excitations along the most confined direction, making the modulation through a single trap frequency inherently anisotropic. In contrast, scattering length modulation exhibits an isotropic nature, as it generates excitations uniformly across all directions. Consequently, systems subjected to anisotropic modulation acquire significant energy, which is rapidly redistributed to attain a stable regime.

By the fast Fourier Transform (FFT) of the energy decomposition, it is possible to discuss the periodicity of the energy oscillations. Figures 4.5 and 4.6 show the FFT of the energy decomposition for the prolate trap with a parametric modulation through the radial frequency and the scattering length, respectively. Similarly, the FFT of the energies of the oblate trap with a parametric modulation via the axial frequency and the scattering length are plotted in Figures 4.7 and 4.8, respectively. In all the cases, the plotted frequencies are in units of the excitation frequency Ω, which is $\Omega = 2\omega_r$ for the prolate trap and $\Omega = 1.80\omega_z$ for the oblate trap.

Notable differences are observed in the Fourier Transform (FFT) of the energy components for the prolate trap. When the parametric modulation is applied through ω_r (Figure 4.5), the interaction $\mathrm{E_{int}}$ and potential energy $\mathrm{E_{pot}}$ predominantly oscillate at a frequency equal to Ω, whereas the kinetic energy E_{kin} primarily oscillates at 2Ω. This behavior differs from the case where the parametric drive is introduced via the scattering length (Figure 4.6). All energy components oscillate at the same frequency Ω in this case.

The FFT of the energies of the oblate trap with a parametric modulation through ω_z, shown in Figure 4.7, makes visible that all the energy terms oscillate mainly with the modulation frequency Ω. The same behavior is observed in the FFT of the energy terms for the oblate trap with a modulation in the scattering length, plotted in Figure 4.8.

4.3.2 Density Patterns

The increase in kinetic energy in the less confined directions, as discussed in Section 4.3.1, should be manifested in some way in the local density of the fluid. The 2D integrated density over the most confined directions can reflect how the energy redistribution affects the system. Thus, for the oblate trap, the z-axis of the density is integrated, and the xy plane is plotted. For the prolate trap, the y-axis is integrated so that the xz plane of the density is plotted. These integrated densities are presented since this information can be obtained experimentally through a typical absorption image.

Figure 4.9 illustrates the formation of fringe patterns in the xz plane density when a prolate trap undergoes parametric modulation via the radial trap frequency or the scattering length; in both types of modulation, the same pattern is observed. As discussed in Section 4.3.1, the kinetic energy in the axial direction begins to increase after $30 - 35$ ms of excitation when the radial frequency is modulated, and after 40 ms when the scattering length is modulated. Before these times, both cases exhibit breathing mode oscillations induced by the parametric modulation at a frequency $\Omega = 2.0\,\omega_r$. When the axial kinetic energy increases at the mentioned times, a disruption in the prolate density distribution is observed, marked by the initial emergence of faint pattern formations. These patterns become more pronounced as the kinetic energy rises further, resulting in the density distribution developing a temporally and spatially periodic fringe pattern.

Figure 4.10 shows the formation of patterns in the xy plane density for an oblate trap under modulation of the axial trap frequency and the scattering length. Due to the geometry of the trap, a ring-shaped pattern emerges in both cases. Similar to the prolate configuration, before the increase in radial kinetic energy, the atomic cloud undergoes expansion and contraction in the xy plane radius due to breathing mode oscillations induced by parametric modulation at a frequency of $\omega = 1.80\,\omega_z$. During this phase, a faint ring pattern begins to appear, which becomes more pronounced as the radial kinetic energy increases at $t \sim 70$ ms for axial trap frequency modulation

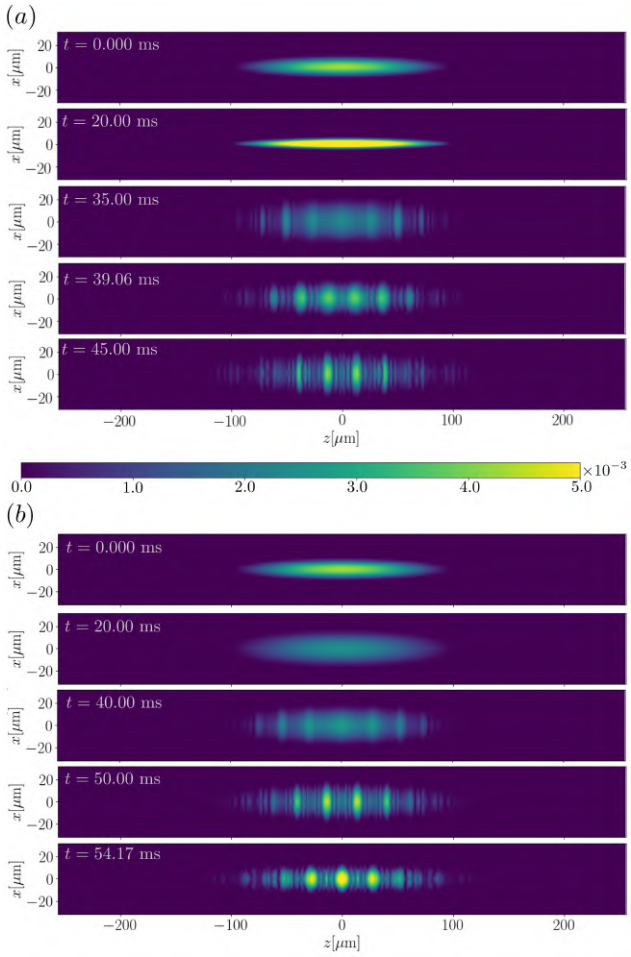

Figure 4.9: The time evolution of the two-dimensional integrated density in a prolate trap is examined under parametric modulation applied to (a) the radial trap frequency and (b) the scattering length. The total density is integrated along the y-axis, yielding values comparable to the experimentally obtained image density via absorption imaging. The emergence of density patterns aligns with the increase in axial kinetic energy $\mathrm{Ekin,z}$. This rise is detected after 30 ms for radial trap modulation and after 40 ms for scattering length modulation. Prior to this increase, the initial density distribution remains unaltered, exhibiting breathing mode oscillations characterized by the contraction and expansion of the atomic cloud. Following the rise in axial kinetic energy, density patterns become visible and are distinctly defined at the peak values of $\mathrm{Ekin,z}$. These patterns disrupt the initial Thomas-Fermi density distribution, resulting in maximum-density fringe structures.

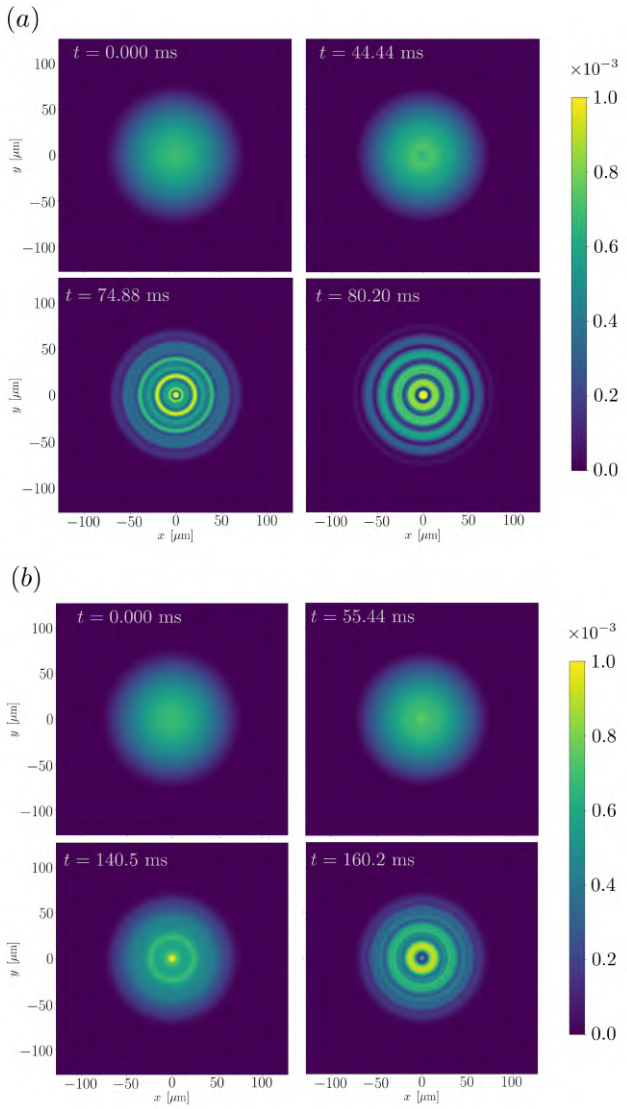

Figure 4.10: The time evolution of the two-dimensional integrated density in an oblate trap is studied under parametric modulation applied to (a) the axial trap frequency and (b) the scattering length. The total density is integrated along the z-axis, yielding values comparable to the image density obtained experimentally via absorption imaging. The emergence of density patterns corresponds to the moment when the radial kinetic energy $E_{\mathrm{kin,r}}$ increases. For axial trap modulation, this rise in kinetic energy is observed after 65 ms, whereas for scattering length modulation, it occurs after 140 ms. In both scenarios, faint ring patterns are noticeable before the kinetic energy increases, and these patterns become more defined following the rise in $E_{\mathrm{kin,r}}$. The formation of density patterns disrupts the initial Thomas-Fermi density distribution, giving rise to ring structures with maximum density.

and $t \sim 140$ ms for scattering length modulation. Once the ring patterns are fully developed, the characteristic Thomas-Fermi density profile, where maximum density is concentrated at the center and decreases radially outward, is disrupted. Instead, multiple density maxima are localized along the rings.

Furthermore, simulations for both the prolate and oblate traps indicate that the density maxima are dynamic, shifting to different positions over time. As discussed in the following subsection, the current density provides insight into the displacement of these density maxima.

An important feature to be emphasized is that the formation of fringe and ring patterns in the prolate and oblate traps matches the time of the energy redistribution between the radial and axial components. This mechanism shows the importance of considering a 3D system for studying the pattern formations since the collective modes in radial and axial directions are correlated.

A potential trap much more elongated in the axial or radial direction should be needed to study the pattern formation in fewer dimensions. For freezing the collective modes in a specific direction (dimensional reduction), the following condition needs to be satisfied [68]:

$$\frac{Na_s}{l_0} \ll \left(\frac{R_{TF}}{l_0}\right)^2, \tag{4.7}$$

where l_0 is defined in (2.26) and R_{TF} is the Thomas-Fermi radius of the plane of interest, i.e., the plane where the collective modes are not frozen. In dimensional reduction, the redistribution mechanism of the total energy that generates the emergence of the density patterns should be different and is an interesting phenomenon to study.

4.3.3 Current Density

The 2D integrated density plots (Figures 4.9 and 4.10) reveal that parametric modulation induces a density flow, disrupting the characteristic Thomas-Fermi profile of the condensate. This results in the formation of periodic patterns, with density maxima localized at varying positions within the atomic cloud. To gain insight into this process, the condensate current density is computed, which serves as a mechanism for energy redistribution in an ultracold sample with periodic modulation. The current density $\mathbf{J}$ of a system with a wave function $\Psi = \sqrt{\rho}e^{\imath S(\mathbf{r})}$ gives information about the phonon propagation [69]. Recalling its definition, $\mathbf{J} = \rho\mathbf{v}$, where ρ is the density of the system and $\mathbf{v}$ the field of velocities of the superfluid given by $\mathbf{v} = \boldsymbol{\nabla} S(\mathbf{r})$, it can rewritten as $\mathbf{J} = \frac{\rho}{m}\mathbf{p} = \frac{\hbar\rho}{m}\mathbf{k}$, where $\mathbf{k}$ is the local wave vector of the phonon excitations.

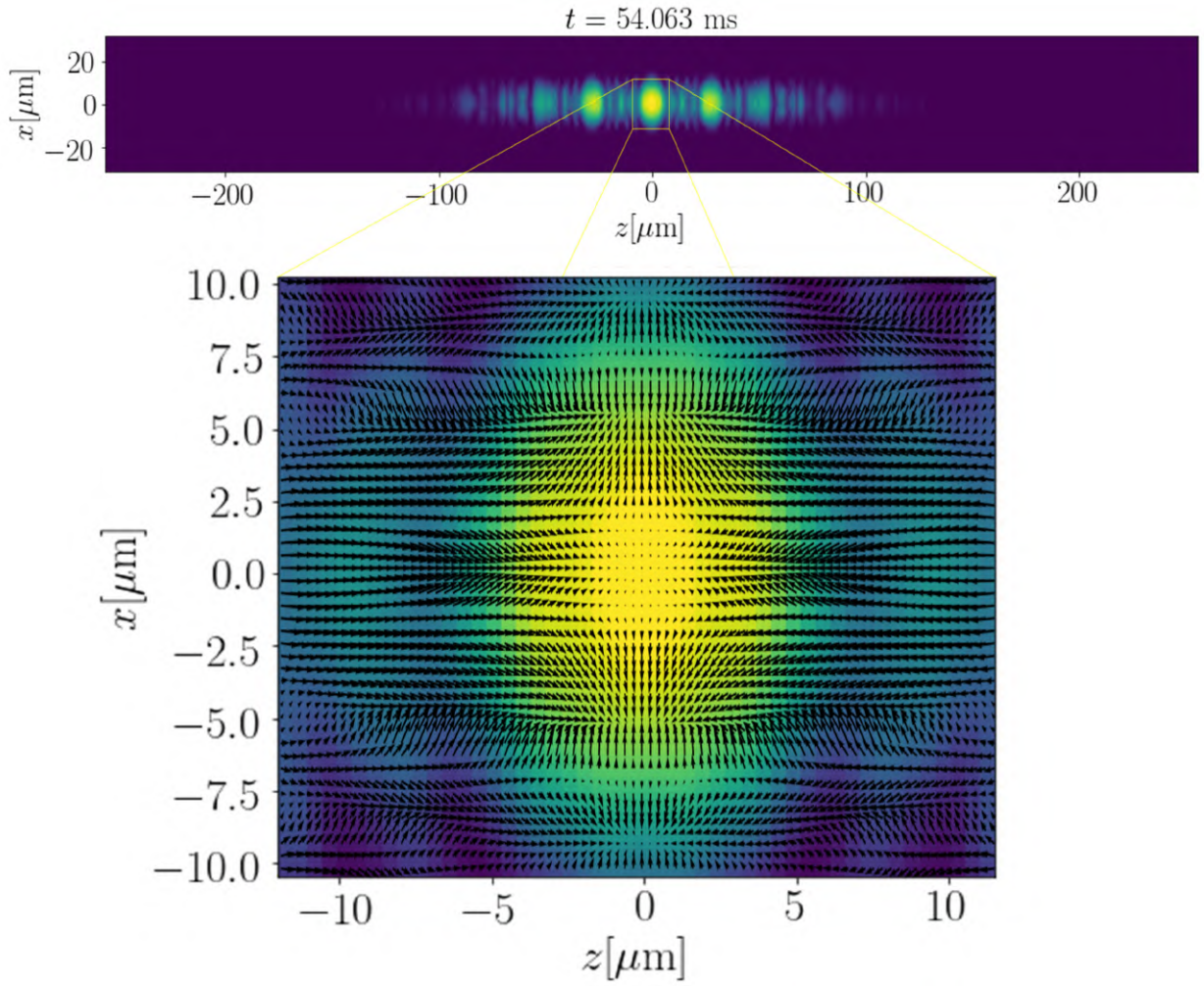

Figure 4.11: The current density in a prolate trap is analyzed under parametric modulation of the scattering length. The vector field is calculated for the xz-plane, which intersects the center of the atomic cloud. The formation of fringe patterns, characterized by regions of maximum density within the atomic cloud, arises from the interference of phonons propagating toward the boundaries of the trap.

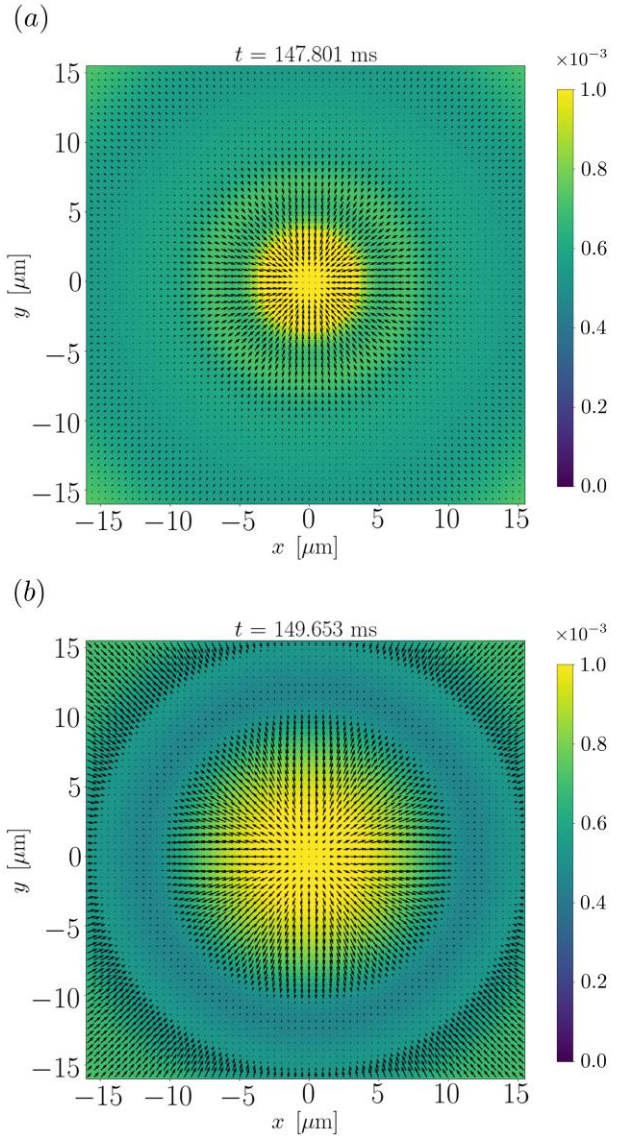

Figure 4.12: The current density in an oblate trap is examined under parametric modulation of the scattering length. The vector field is computed for the xy-plane, which passes through the center of the atomic cloud. The emergence of ring patterns is attributed to the interference of phonons propagating radially toward the boundaries of the trap.

The density currents analyzed in this section are calculated for the xy plane intersecting the midpoint of the atomic cloud in the oblate trap and the xz plane intersecting the midpoint of the atomic cloud in the prolate geometry.

Figure 4.11 illustrates the behavior of the current density in a prolate trap. During the expansion of the trap, driven by the breathing mode collective oscillation, the vector field indicates that the density is displaced from the trap's center toward the extremities along the z axis. Conversely, during the contraction of the atomic cloud, the current density vector field directs the density back toward the trap center. This cyclic mechanism of expansion and contraction, which displaces density away from and back toward the trap center, leads to the formation of fringe patterns through the interference of density regions moving in opposite directions. Interestingly, the geometry of the trap defines the main direction in which the current density travels.

Figure 4.12 shows the propagation of the current density in the oblate trap. Similar to the prolate case, when the atomic cloud contracts due to breathing mode oscillations, the density displacement occurs radially toward the trap center (Fig. 4.12(a)). In contrast, during the expansion of the atomic cloud, the density is displaced radially outward, away from the trap center (Fig. 4.12(b)). These radial density displacements are responsible for the formation of the ring patterns.

It is important to note that the local density of angular momenta is null in either of the cases. Therefore, no vortex or other associated topological defect is present in the condensate density. This is to be expected since the ansatz (2.24) of the ground state was considered with $l = 0$. However, when the parametric modulation is introduced, the system propagates excitations that travel in directions that minimize energy but respect the symmetry of $l = 0$. In this sense, and due to the trap geometry, in the oblate trap, the phonons propagate in the radial direction, generating ring patterns. The phonons propagate along the z-axis in the prolate trap, generating the fringe patterns. Thus, the external potential imposes the symmetry of the generated patterns. Since the harmonic trap has cylindrical symmetry, the reflection of the excitations preserves the same configuration.

A natural squared symmetry is expected when there is no external potential. This is observed in reference [38] where, by imposing a square symmetry through the ansatz of the wave function, they generate stable squared patterns in an infinitely extended BEC without trapping potential and with the scattering length modulated. In contrast, in the system presented in this thesis, and due to the symmetry imposed by the external potential, the generated patterns (rings in the oblate

trap and fringes in the prolate trap) arise naturally and are the reflection of the excitations over the boundaries of the potential.

4.3.4 Fidelity

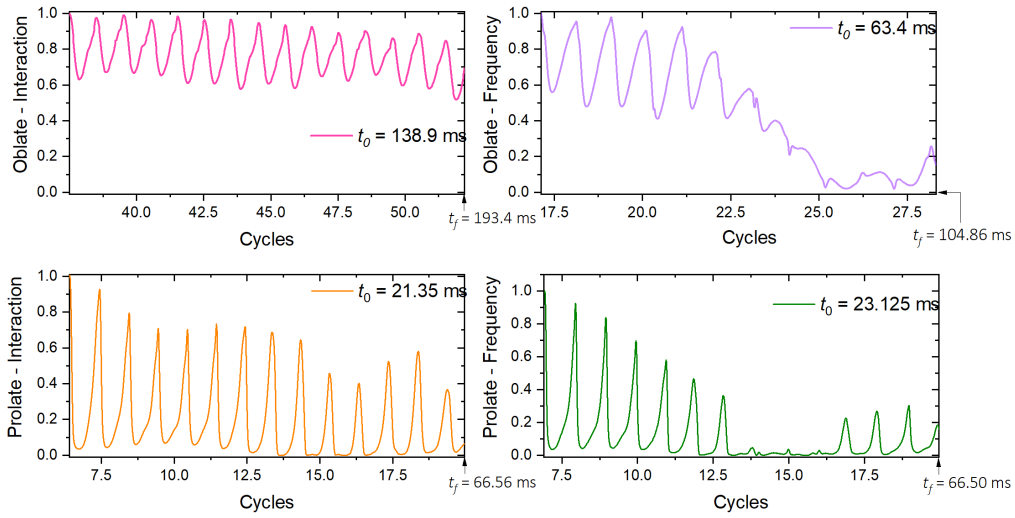

Figure 4.13: The fidelity function is analyzed for both parametric modulations in oblate and prolate traps. Function (4.8) is employed to investigate the evolution of the density patterns formed in the system. The initial wave function, $\Psi_{ab}(t)$, which serves as a reference for comparisons with subsequent wave functions $\Psi_{ab}(t+dt)$, is chosen such that the initial time t corresponds to the point where the kinetic energy begins to increase. For modulation via scattering length, it is observed that the patterns in both geometries exhibit greater stability over an extended time interval compared to the patterns' behavior under modulation introduced through a single trap frequency.

The temporal periodicity of the patterns and their lifetimes (the interval of time at which they can be experimentally observed) can be studied by a fidelity function. For simplicity, and similar to the current density discussed in Subsection 4.3.3, the fidelity function is defined over a plane and not in all the atomic cloud space. Thus, for the prolate trap, the xz plane at $y = 0$ is considered. In the same way, the xy plane at $z = 0$ is taken for the oblate trap.

The definition of the fidelity function is:

$$F[t] = \frac{\left|\left\langle \Psi_{ab}^{*}(t+dt)\,\Psi_{ab}(t)\right\rangle\right|^{2}}{\left\langle \Psi_{ab}^{*}(t+dt)\,\Psi_{ab}(t+dt)\right\rangle\left\langle \Psi_{ab}^{*}(t)\,\Psi_{ab}(t)\right\rangle} \tag{4.8}$$

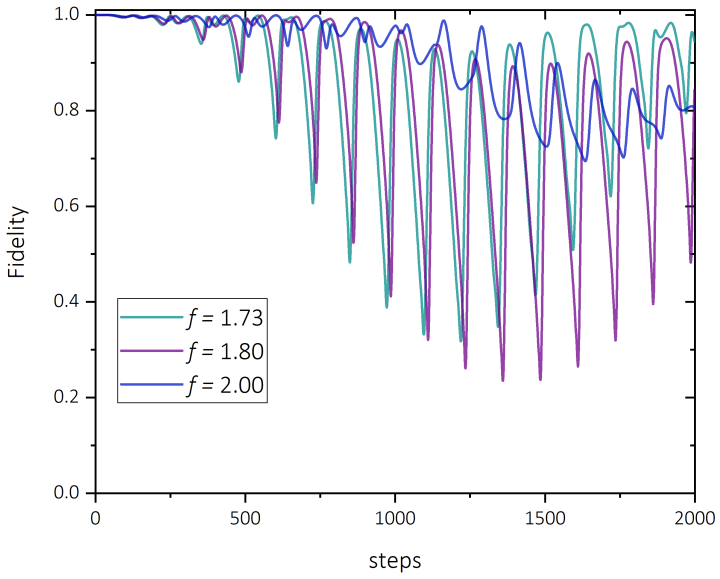

Figure 4.14: Comparison of fidelity for different modulation frequencies applied to the system. For an oblate trap with fixed frequencies $\omega_r 0 = 2\pi \times 150$ Hz, the variational method predicts that the breathing mode frequency is $\Omega = f\omega_z$, where $f = 1.80$. When the system is modulated at frequencies near this value, the resulting oscillations are smaller and decay more rapidly. The x-axis represents the numerical simulation steps, which are related to time by $t = (\text{steps} \times dt)\omega_z$, with dt defined as $dt = \frac{T_{\text{exc}}}{2^{13}}$, where $T_{\text{exc}} = \frac{2\pi N_\Omega}{\Omega}$.

where Ψ_{ab} denotes the wave function of the plane of interest, i.e., xz plane for the prolate and xy for the oblate trap. The function is normalized just for the considered plane, therefore, brackets $\langle\rangle$ denote the integration just over the plane.

To study the time behavior of the generated patterns, the fidelity function is computed with the wave functions at the plane of interest, Ψ_{xz} and Ψ_{xy}, and evaluated at the times at which the kinetic energy in the less confined direction increases. These times are reported in Figures 4.1, 4.2, 4.3, and 4.4. The fidelity function is better presented not in units of time but in cycles of excitation, given by $\frac{t}{T_{\text{exc}}}$.

Figure 4.13 compares the evolution of the xz-plane wave function for the prolate trap in the seventh excitation cycle for the radial trap and scattering length modulations. For the oblate trap, the wave function at the 37th excitation cycle is taken for comparison when the modulation is through the axial trap frequency. For the scattering length modulation, the wave function for comparison is chosen in the 17th excitation cycle. Those times were chosen because they are close to the time at which the increasing of the kinetic energy is observed.

In the prolate trap, the system exhibits oscillatory behavior, transitioning from a nearly orthogonal state, characterized by a zero inner product, to a state closely resembling the initial configuration. Over time, the similarity between these states diminishes. However, the temporal interval over which these oscillations occur is sufficiently broad to allow for experimental observation.

The dynamics of the oblate trap differ between the two types of parametric modulation. When modulation is applied through the scattering length, the system remains similar with its initial state, as evidenced by the fidelity function maintaining values above 0.5. In contrast, for modulation via the axial frequency, the system oscillates between similar states over a short time interval, during which the wave function exhibits a recurring density pattern. However, after the 22nd excitation cycle, the system transitions to a distinct state. Notably, ring patterns are observable between the 17th and 22nd excitation cycles.

In summary, for an oblate trap, the fidelity function reveals a distinction between axial frequency and scattering length modulations, particularly in terms of the stability and lifetime of the resulting density patterns. In contrast, the behavior of both types of parametric modulation in the prolate trap is largely similar. These findings are consistent with the results reported in [70] and extend their analysis by providing additional insights specific to the oblate trap.

Finally, the fidelity function can be used to compare the system's behavior when it is modulated with different frequencies. As presented in Figure 2.2, the frequency Ω at which the system is modulated affects the oscillations of the widths of the Gaussian wave function in the variational approach. These modifications are also reflected in the formation of the density patterns. In Figure 4.14, the Fidelity function shows that when an oblate trap is modulated with a frequency different from the resonance frequency $1.80\,\omega_z$, but with values similar to it, as $\Omega = 1.73\,\omega_z$ and $\Omega = 2.0\,\omega_z$, the system responds oscillating to the perturbation. However, these oscillations are smaller and decay faster than those observed in the resonance. These theoretical expectations mean that patterns will appear sooner, and it would be more feasible to observe experimentally when the system is modulated near the resonance frequency. As the excitation frequency gets far from the resonance, patterns will take longer to appear.

4.4 Special cases

This subsection studies the oblate and prolate traps under two different new conditions. First, the case when the parametric modulation is introduced without interactions between the particles is presented. Subsequently, the possibility of modulating the system through the less confined direction is taken into account to study if the system presents a different behavior in comparison when the modulation is introduced through the trap frequencies of the most confined directions.

Modulation without interactions

Until now, it has been observed that the geometry of the external potential strongly influences the generated density patterns. However, the scattering length also affects the dynamic of the patterns. Equation (4.1) makes evident that the nonlinearity term characterizing the system is affected by modifying the interactions. In fact, if the interactions are suppressed, this nonlinearity term is suppressed, changing the dynamics and behavior of the system.

The variational equations obtained in Chapter (2) illustrate that the collective modes of the system are influenced by the interaction between particles. Thus, a change in the collective oscillations is expected when the scattering length a_s is modified. Particularly, matrix (2.34), which determines the frequencies associated with the quadrupolar and monopolar modes of the system, shows that the presence of interactions couples both modes since they are the non-diagonal terms

that are proportional to the scattering length. Thus, without interactions, the coupling between the radial and axial modes is lost:

$$\mathcal{W}_0 = \begin{pmatrix} 4\omega_{r0}^2 & 0 \\ 0 & 3\omega_{z0}^2 + \frac{1}{\sigma_{z_0}^4} \end{pmatrix}. \tag{4.9}$$

The variational equations of motion for the Gaussian widths σ_{r0} and σ_{z0} are also affected in the absence of interactions. Considering $a_{s0} = 0$, the following linear equations for the prolate trap are obtained,

$$\ddot{\delta}_r(t) = \left[4\omega_{r0}^2 + \alpha\omega_{r0}^2 \cos\Omega(t - t_0)\right] \delta_r = -\alpha\omega_{r0}^2\sigma_{r0} \tag{4.10a}$$

$$\ddot{\delta}_z(t) + \left(3\omega_{z0}^2 + \frac{1}{\sigma_{z0}^4}\right) \delta_z = 0 \tag{4.10b}$$

In an analog form, for the oblate trap without interactions, the variational equations of motion are:

$$\ddot{\delta}_r + 4\omega_{r0}^2\delta_r = 0 \tag{4.11a}$$

$$\ddot{\delta}_z + \left[3\omega_{z0}^2 + \frac{1}{\sigma_{z0}^4} + \alpha\omega_{z0}^2 \cos\Omega(t - t_0)\right] = -\alpha\omega_{z0}^2\sigma_{z0} \tag{4.11b}$$

From equations (4.10) and (4.11), it can be observed that when the interactions are taken out, the dynamics in the axial and radial directions are decoupled. As a consequence, the system reduces to a harmonic oscillator in the direction where no modulation is introduced, and to a forced Mathieu equation in the perpendicular direction.

The suppression of the interaction can also be observed in the numerical simulations. Figure 4.15 plots the Fidelity function of a BEC confined in an oblate trap with a value of the scattering length a_{s0} that tends to zero and is parametrically modulated through the trap frequency ω_z. It is noticed that the fidelity function only oscillates between 0.98 and 1.0, which manifests that there is no evident change in the system compared with the initial state. This means that when there is no interaction between particles, the atomic cloud does not have how to dissipate the introduced excitations. Thus, the system does not respond to external modulation.

Finally, the decomposition of the energy terms shows the consequences of the lack of coupling between the radial and axial modes. Figure 4.16 demonstrates that there is no correlation between the behavior of the axial and radial energy terms. They oscillate with a different frequency, and no energy redistribution is observed.

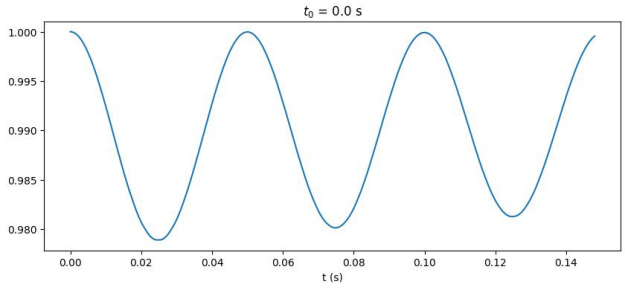

Figure 4.15: Fidelity function for an oblate trap with no interactions.

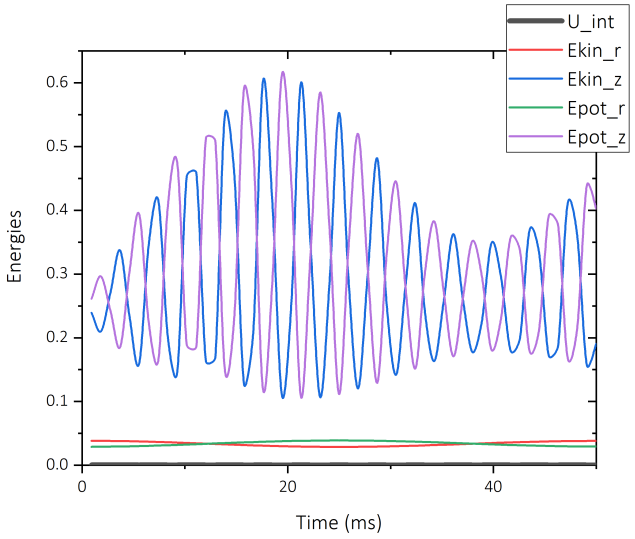

Figure 4.16: Decomposition of the total energy for an oblate trap with no interactions.

Modulation in the perpendicular direction

If the parametric modulation is introduced via the trap frequency of the loosely confined direction, some differences arise with respect to the previous reported collective motion. To analyse some of these differences, the variational approximation can be used. For the prolate configuration, the resulting equations of motion are given by,

$$\begin{aligned} \ddot{\sigma}_r + \omega_{r0}^2 \sigma_r &= \frac{1}{\sigma_r^3} + \sqrt{\frac{2}{\pi}} \frac{N a_s}{\sigma_r^3 \sigma_z} \\ \ddot{\sigma}_z + \omega_{z0}^2 \left(1 + \alpha \sin\left(\Omega t\right)\right) \sigma_z &= \frac{1}{\sigma_z^3} + \sqrt{\frac{2}{\pi}} \frac{N a_s}{\sigma_r^2 \sigma_z^2}. \end{aligned}$$

For the oblate trap, the modified equations of motion are:

$$\begin{aligned} \ddot{\sigma}_r + \omega_{r0}^2 \left(1 + \alpha \cos \Omega \left(t - t_0\right)\right) \sigma_r &= \frac{1}{\sigma_r^3} + \sqrt{\frac{2}{\pi}} \frac{N a_s}{\sigma_r^3 \sigma_z} \\ \ddot{\sigma}_z + \omega_{z0}^2 \sigma_z &= \frac{1}{\sigma_z^3} + \sqrt{\frac{2}{\pi}} \frac{N a_s}{\sigma_r^2 \sigma_z^2}. \end{aligned}$$

As discussed in Chapter 2, these sets of differential equations can be solved by considering a linearization, this is, by approximating the change in the Gaussian widths σ_r and σ_z as a small variation around their initial value,

$$\sigma_r\left(t\right) = \sigma_{r0} + \delta_r\left(t\right), \qquad \sigma_z\left(t\right) = \sigma_{z0} + \delta_z\left(t\right).$$

After introducing this linear consideration, the following equations of motion are found for the prolate and oblate trap:

- Prolate Trap

$$\ddot{\delta}_r + 4\omega_{r0}^2 \delta_r + \sqrt{\frac{2}{\pi}} \frac{N a_s}{\sigma_{r0}^3 \sigma_{z0}^2} \delta_z = 0 \tag{4.12a}$$

$$\ddot{\delta}_z + \left\{ 3\omega_{z0}^2 + \frac{1}{\sigma_{z0}^4} + \omega_{z0}^2 \alpha \sin\left(\Omega t\right) \right\} \delta_z + 2\sqrt{\frac{2}{\pi}} \frac{N a_s}{\sigma_{r0}^3 \sigma_{z0}^2} \delta_r = -\omega_{z0}^2 \alpha \sin\left(\Omega t\right) \sigma_{z0} \tag{4.12b}$$

- Oblate Trap

$$\ddot{\delta}_r + \left[4\omega_{r0}^2 + \alpha \omega_{r0}^2 \cos \Omega \left(t - t_0\right) \right] \delta_r + \sqrt{\frac{2}{\pi}} \frac{N a_s}{\sigma_{r0}^3 \sigma_{z0}^2} \delta_z = -\omega_{r0}^2 \alpha \sin\left(\Omega\, t\right) \sigma_{r0} \tag{4.13a}$$

$$\ddot{\delta}_z + \left[3\omega_{z0}^2 + \frac{1}{\sigma_{z0}^4} \right] \delta_z + 2\sqrt{\frac{2}{\pi}} \frac{N a_s}{\sigma_{r0}^3 \sigma_{z0}^2} \delta_r = 0 \tag{4.13b}$$

Figure 4.17 plots the solutions to (4.12) and (4.13) when the frequency modulation Ω is equal to the breathing mode frequency, i.e., $\Omega = 2.0\omega_r$ for the elongated geometry and $\Omega = 1.80\omega_z$ for the oblate geometry. It can be observed that the atomic cloud oscillates with a smaller amplitude in the weakly confined direction and with a lower frequency in comparison with the case of the parametric excitation in the tightly confined direction (Figure 2.2). Due to the coupling between the axial and radial modes introduced by the interaction, we can see that the tightly confined direction also oscillates but with a very small amplitude, requiring longer time units for this oscillation to be representative. Thus, experimentally, it would be difficult to observe the formation of any density pattern due to the lower response of the system. A numerical simulation of the GPE for an oblate

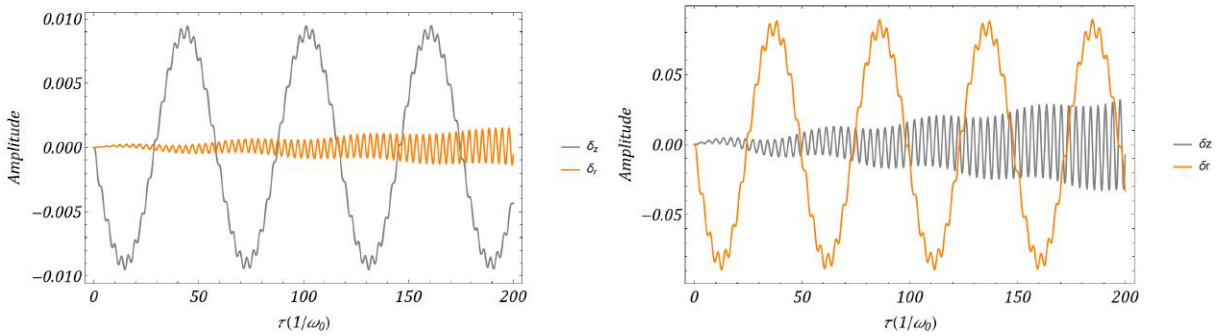

Figure 4.17: Amplitude behavior of the widht variations δ_r and δ_z for the (Left) prolate and (Right) oblate trap when the parametric modulation is introduced through the loosely confined frequency.

trap with parametric modulation through the radial (loosely confined) direction was performed to confirm that no density pattern is observed within an appropriate experimental interval of time. Figure 4.18 shows the fidelity function where the initial wave function at $t = 0$ is compared with the system's state at later times. Since the fidelity function oscillates between values of ~ 0.98 and 1.0, it is evident that no significant change is generated in the system with this direction of the parametric modulation. As no significant effect was observed upon introducing the breathing mode frequency in the loosely confined direction, a new numerical simulation was performed, but this time considering the quadrupolar frequency. The solution to equations (4.12) and (4.13) where $\Omega = 0.10\omega_r$ for the prolate trap and $\Omega = 0.12\omega_z$ for the oblate trap is shown in Figure 4.19. In contrast with the breathing mode, in this collective mode and due to the geometry of the traps, the principal oscillation is observed in the loosely confined direction. However, the frequency of

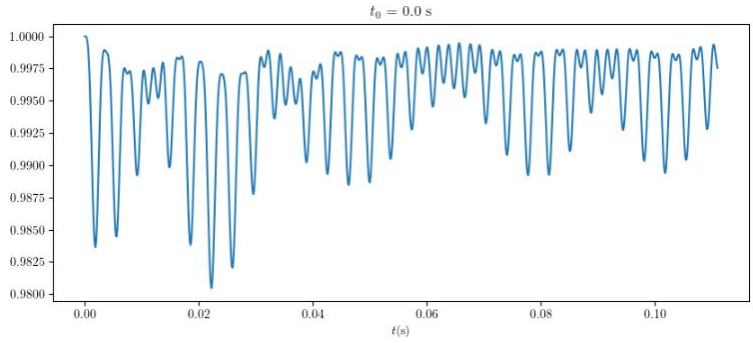

Figure 4.18: Fidelity function when a parametric modulation with a frequency equal to the breathing mode is introduced in the loosely confined direction (radial direction) of the oblate trap.

the system's response is still very low. In conclusion, introducing a parametric modulation through

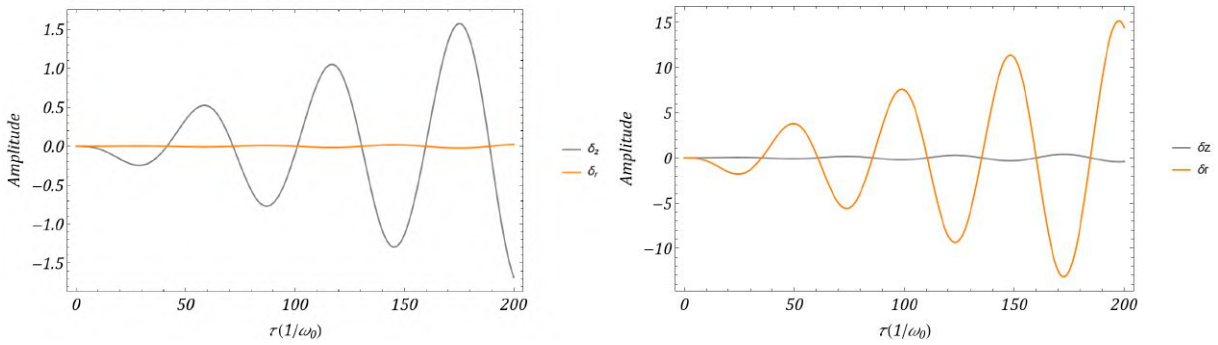

Figure 4.19: Amplitude behavior of the widht variations δ_r and δ_z for the prolate (left) and oblate (right) trap when the parametric modulation is introduced through the loosely confined frequency with a frequency equal to the quadrupolar mode.

the trap frequency of the less confined directions does not generate an important perturbation to the system that could allow the arising of density patterns in plausible experimental times. This behavior is observed with both possible collective frequencies: breathing and quadrupolar modes.

Chapter 5

Perspectives and Conclusions

This thesis presents a study of the pattern formation over a density of a Bose-Einstein Condensate when the system is parametrically modulated through one of the trap frequencies or the scattering length describing the interaction between particles.

The thesis can be divided into two parts. In the first part, the collective modes of the BEC are obtained by a variational approach, where different configurations and parametric modulations are considered. In the second part, the frequencies of the collective modes are introduced in a numerical simulation of the Gross-Pitaevskii equation to parametrically modulate the system and study the emergence of density patterns.

The variational method is important because it allows a semi-analytic solution to the collective mode frequencies that can be completely solved in an easy numerical way. Once an ansatz for the wave function is proposed, the problem is reduced to a set of differential equations associated with the variational parameters that can be solved by a linearization procedure. This approximation decreases the numerical analysis and allows the characterization of the system's natural frequencies for any external potential, in contrast to the method of solving the non-linear differential equations associated with the hydrodynamic behavior, where the solution is restricted to the consideration of an isotropic potential and the Thomas-Fermi approximation. Although the variation method allows the study of a BEC in different configurations, it is important to mention that the precision of the solution depends on the proposed ansatz.

The frequencies that characterize the collective response of the system correspond to the breathing mode and the quadrupolar mode. Through the variational method, it is observed that they depend on the external potential and particle interaction. Thus, for different geometries of confinement, the system oscillates distinctly. However, for any configuration, it is observed that the quadrupolar mode has a lower frequency compared with the breathing mode. Thus, the atomic

cloud oscillates at a lower frequency, as shown in Figure 4.19.

An analysis of the system's time evolution through the Gross-Pitaevskii equation shows that due to the difference in the frequency values, the system's response is different when the parametric modulation is introduced with each one. When the system is modulated with the breathing mode, density patterns arise over the BEC, which are not observed with the quadrupolar mode during plausible experimental times.

The computation of the current density allows to explain the arising of the density patterns as a consequence of the phonon propagation. Due to the ratio trap frequencies, the phonons have a preferential direction of propagation, which correlates with the more elongated direction. Therefore, the phonons propagate preferentially in the axial direction for the prolate trap, creating a fringe pattern by the interference of the counterpropagating phonons in this direction. In the oblate trap, the phonons can propagate radially in a plane corresponding to the radial direction. The interference of these phonons creates ring patterns.

Further, by decomposing the total energy into its components and its axial and radial contributions, it is observed that the arising density patterns coincide with the increase of kinetic energy in the more elongated direction. Thus, an increase in the axial kinetic energy and an increase in the radial kinetic energy are observed for the prolate and oblate trap, respectively.

By comparing the times at which the kinetic energy increases in both geometries, it is possible to predict at what time, experimentally, it would be feasible to observe the patterns. In this sense, creating ring patterns in an oblate trap is expected to be more difficult since the system dissipates the introduced energy better, delaying the time at which the kinetic energy increases. Therefore, this work can be used as a guide in the experimental realization of the ring patterns.

An extension to this work could be the study of the generated patterns in different values of the scattering length since, in the analysis performed in this thesis, the scattering length is kept constant. However, this proposal has a limitation since the Gross-Pitaevski equation is not valid for stronger interaction systems where the condition $\eta > 1$ describing a BEC limit of a dilute Fermi gas is not satisfied. In this sense, the results obtained in this work invite us to expand the analysis to the unitary regime and remind us that a universal theory for this Fermi system is still missing.

Finally, introducing an angular momentum to the variational ansatz for the wavefunction could allow the phonons to propagate not only in a radial direction but also in angular directions, which

could give the formation of more complex structures that can have an associated angular momentum. Eventually, this process could create turbulence. Two types of turbulence could be created and studied through the modulation of these systems: vortex and wave turbulence.

Chapter 6

Supplementary Research Contributions

6.1 Overview

This chapter discusses the supplementary work performed during the PhD, which is unrelated to the main theme presented in this thesis and has been discussed plenty in the previous chapters.

Section 6.2 provides a concise overview of the dynamics of a three-level effective atom in a Λ configuration, interacting with a two-mode quantum field within a cavity. The analysis is conducted using the rotating wave approximation and incorporates experimentally accessible hyperfine levels of alkali atoms.

Section 6.3 discusses the theoretical and numerical study of the evaporative cooling procedure for a Fermi and a Bose gas.

6.2 Three level atom interacting with a quantum field

The study of this system was realized due to the similarities presented with the Gray Molasses mechanism discussed in Chapter 3. One of the principal differences between the cooling procedure and the case presented in this section is that here, there are considered quantized fields and no kinetic energy on the atoms is taken in account. However, the problem is demonstrated to be experimentally accessible, and one could find interesting dynamics. The complete report on this system has been published and can be found at reference [44].

The Hamiltonian describing the system of an atom of three-levels in Λ configuration interacting with an electromagnetic field of two-modes, which are coupled by a dipole interaction and within

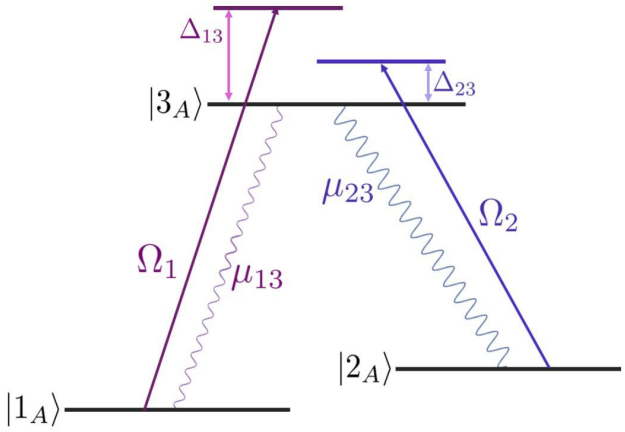

Figure 6.1: Scheme of an atom of three levels. Since dipolar transitions are considered, transition $|1\rangle \to |2\rangle$ is forbidden. Finally, transitions $|1\rangle \to |3\rangle$ and $|2\rangle \to |3\rangle$ are realized due to the photons with frequencies Ω_1 and Ω_2, respectively.

the rotating wave approximation is given by,

$$\begin{aligned} \hat{H} &= \sum_{k=1}^{3} E_k \hat{A}_{kk} + \sum_{s=1}^{2} \hbar\Omega_s \hat{n}_s - \hbar\mu_{13}\left(\hat{a}_1^\dagger \hat{A}_{13} + \hat{a}_1 \hat{A}_{31}\right) \\ &- \hbar\mu_{23}\left(\hat{a}_2^\dagger \hat{A}_{23} + \hat{a}_2 \hat{A}_{32}\right), \end{aligned} \tag{6.1}$$

where the first term corresponds to the energies of the effective three-level system $E_k \equiv \hbar\omega_k$ with $k = 1, 2, 3$. The one-atom states are denoted by the ket $|k_A\rangle$ with $k = 1, 2, 3$, and the action of the operators $\hat{A}_{ij}$ is defined as,

$$\hat{A}_{ij}|k_A\rangle = \delta_{j,k}|i_A\rangle.$$

Since dipole interactions govern the transitions between atomic levels, the transition between states $|1_A\rangle$ and $|2_A\rangle$ is forbidden since both possess the same parity. The allowed transitions in the system are $|1_A\rangle \longleftrightarrow |3_A\rangle$ and $|2_A\rangle \longleftrightarrow |3_A\rangle$. For each one of the allowed transitions, photons with frequencies Ω_1 and Ω_2 are considered (Figure 6.1).

The Hamiltonian (6.1) is rewritten in a basis formed by the direct product of the atomic states with Fock states of light. In this way, it is possible to generalize the state of light to any quantum field. Besides, the interaction term of the Hamiltonian restricts the system to a 3D Hilbert space.

Through the analysis of the system's time evolution, it is observed that the system shows similarities with the effective two-level system, such as collapses and revivals and atom-field entanglement.

Finally, the statistical analysis of photons demonstrates that, when a three-level atom interacts with a two-mode coherent field, the statistical properties of the field can be experimentally manipulated to exhibit either super-Poissonian or sub-Poissonian behavior, depending on the selection of the atom's initial state.

6.3 Evaporative Cooling

A study is presented on the thermodynamics of a classical and quantum gas confined by an atomic trap, utilizing generalized variables that enable the proposal of new thermodynamic quantities, including gas density, particle number, and energy. The approach introduces an evaporative cooling protocol, which describes the cooling process of an atomic gas within classical or quantum distributions. By applying this protocol to different confining potentials, recurrence relations are derived to calculate the gas density, particle number, and energy after the removal of the most energetic particles and the re-establishment of equilibrium. This methodology allows for the characterization of the system's thermodynamic properties at each stage of the cooling procedure. The theoretical framework is subsequently applied to atomic gases governed by Maxwell-Boltzmann, Bose-Einstein, and Fermi-Dirac statistics.

Bibliography

[1] E. H. Lieb, R. Seiringer, J. P. Solovej, and J. Yngvason, "The mathematics of the bose gas and its condensation," 2006.

[2] B. Keimer, S. A. Kivelson, M. R. Norman, S. Uchida, and J. Zaanen, "From quantum matter to high-temperature superconductivity in copper oxides," *Nature*, vol. 518, no. 7538, pp. 179–186, 2015.

[3] L. Skrbek and Y. A. Sergeev, "Critical velocities in flows of superfluid 4he," *Physics of Fluids*, vol. 37, p. 031305, 03 2025.

[4] P. Ball, *The Self-made Tapestry: Pattern Formation in Nature*. Oxford University Press, 1999.

[5] A. M. Turing, "The chemical basis of morphogenesis," *Philosophical Transactions of the Royal Society of London. Series B, Biological Sciences*, vol. 237, pp. 37–72, Aug. 1952.

[6] K. Lindgren, *Pattern Formation in Chemical Systems*, pp. 115–132. Berlin, Heidelberg: Springer Berlin Heidelberg, 2024.

[7] M. C. Cross and P. C. Hohenberg, "Pattern formation outside of equilibrium," *Rev. Mod. Phys.*, vol. 65, pp. 851–1112, Jul 1993.

[8] A. Getling, *Rayleigh-Bénard Convection: Structures and Dynamics*. Advanced series in nonlinear dynamics, World Scientific, 1998.

[9] G. I. Taylor, "Viii. stability of a viscous liquid contained between two rotating cylinders," *Philosophical Transactions of the Royal Society of London. Series A, Containing Papers of a Mathematical or Physical Character*, vol. 223, no. 605-615, pp. 289–343, 1923.

[10] A. Champneys, "Dynamics of parametric excitation," in *Encyclopedia of Complexity and Systems Science* (R. A. Meyers, ed.), pp. 2323–2345, New York, NY: Springer New York, 2009.

[11] N. McLachlan, *Theory and Application of Mathieu Functions*. Clarendon Press, 1947.

[12] F. Arscott, I. Sneddon, M. Stark, and S. Ulam, *Periodic Differential Equations: An Introduction to Mathieu, Lamé, and Allied Functions*. International series of monographs in pure and applied mathematics, Elsevier Science, 2014.

[13] J. Miles and D. Henderson, "Parametrically forced surface waves," *Annual Review of Fluid Mechanics,*, vol. 22, no. Volume 22, 1990, pp. 143–165, 1990.

[14] K. Kumar, "Linear theory of faraday instability in viscous liquids," *Proceedings of the Royal Society of London. Series A: Mathematical, Physical and Engineering Sciences*, vol. 452, pp. 1113–1126, Jan. 1997.

[15] S. Kumar, "Mechanism for the faraday instability in viscous liquids," *Phys. Rev. E*, vol. 62, pp. 1416–1419, Jul 2000.

[16] E. Cerda and E. Tirapegui, "Faraday's instability for viscous fluids," *Phys. Rev. Lett.*, vol. 78, pp. 859–862, Feb 1997.

[17] R. A. Barrio, J. L. Aragón, C. Varea, M. Torres, I. Jiménez, and F. Montero de Espinosa, "Robust symmetric patterns in the faraday experiment," *Phys. Rev. E*, vol. 56, pp. 4222–4230, Oct 1997.

[18] Y. Guo, H. Yao, S. Ramanjanappa, S. Dhar, M. Horvath, L. Pizzino, T. Giamarchi, M. Landini, and H.-C. Nägerl, "Observation of the 2d-1d crossover in strongly interacting ultracold bosons," *Nat. Phys.*, vol. 20, no. 6, pp. 934–938, 2024.

[19] C. Chin, R. Grimm, P. Julienne, and E. Tiesinga, "Feshbach resonances in ultracold gases," *Rev. Mod. Phys.*, vol. 82, pp. 1225–1286, 2010.

[20] C. H. Schunck, M. W. Zwierlein, C. A. Stan, S. M. F. Raupach, W. Ketterle, A. Simoni, E. Tiesinga, C. J. Williams, and P. S. Julienne, "Feshbach resonances in fermionic ^{6}Li," *Phys. Rev. A*, vol. 71, p. 045601, Apr 2005.

[21] R. G. Hulet, J. H. V. Nguyen, and R. Senaratne, "Methods for preparing quantum gases of lithium," *Rev. Sci. Instrum.*, vol. 91, p. 011101, 01 2020.

[22] D. M. Stamper-Kurn, H.-J. Miesner, S. Inouye, M. R. Andrews, and W. Ketterle, "Collisionless and hydrodynamic excitations of a bose-einstein condensate," *Phys. Rev. Lett.*, vol. 81, pp. 500–503, Jul 1998.

[23] C. Buggle, P. Pedri, W. von Klitzing, and J. T. M. Walraven, "Shape oscillations in nondegenerate bose gases: Transition from the collisionless to the hydrodynamic regime," *Phys. Rev. A*, vol. 72, p. 043610, Oct 2005.

[24] M. J. Wright, S. Riedl, A. Altmeyer, C. Kohstall, E. R. S. Guajardo, J. H. Denschlag, and R. Grimm, "Finite-temperature collective dynamics of a fermi gas in the bec-bcs crossover," *Phys. Rev. Lett.*, vol. 99, p. 150403, Oct 2007.

[25] M. Bartenstein, A. Altmeyer, S. Riedl, S. Jochim, C. Chin, J. H. Denschlag, and R. Grimm, "Collective excitations of a degenerate gas at the bec-bcs crossover," *Phys. Rev. Lett.*, vol. 92, p. 203201, May 2004.

[26] M. K. Tey, L. A. Sidorenkov, E. R. S. Guajardo, R. Grimm, M. J. H. Ku, M. W. Zwierlein, Y.-H. Hou, L. Pitaevskii, and S. Stringari, "Collective modes in a unitary fermi gas across the superfluid phase transition," *Phys. Rev. Lett.*, vol. 110, p. 055303, Jan 2013.

[27] B. Huang, I. Fritsche, R. S. Lous, C. Baroni, J. T. M. Walraven, E. Kirilov, and R. Grimm, "Breathing mode of a bose-einstein condensate repulsively interacting with a fermionic reservoir," *Phys. Rev. A*, vol. 99, p. 041602, Apr 2019.

[28] J. Kronjäger, C. Becker, P. Soltan-Panahi, K. Bongs, and K. Sengstock, "Spontaneous pattern formation in an antiferromagnetic quantum gas," *Phys. Rev. Lett.*, vol. 105, p. 090402, Aug 2010.

[29] Z. Zhang, K.-X. Yao, L. Feng, J. Hu, and C. Chin, "Pattern formation in a driven bose-einstein condensate," *Nature Physics*, vol. 16, no. 6, pp. 652–656, 2020.

[30] K. Staliunas, S. Longhi, and G. J. de Valcárcel, "Faraday patterns in bose-einstein condensates," *Phys. Rev. Lett.*, vol. 89, p. 210406, Nov 2002.

[31] A. I. Nicolin, R. Carretero-González, and P. G. Kevrekidis, "Faraday waves in bose-einstein condensates," *Phys. Rev. A*, vol. 76, p. 063609, Dec 2007.

[32] K. Staliunas, S. Longhi, and G. J. de Valcárcel, "Faraday patterns in low-dimensional bose-einstein condensates," *Phys. Rev. A*, vol. 70, p. 011601, Jul 2004.

[33] L. Brito, L. Tomio, and A. Gammal, "Faraday waves on a bubble-trapped bose-einstein-condensed binary mixture," *Phys. Rev. A*, vol. 108, p. 053315, Nov 2023.

[34] D. K. Maity, K. Mukherjee, S. I. Mistakidis, S. Das, P. G. Kevrekidis, S. Majumder, and P. Schmelcher, "Parametrically excited star-shaped patterns at the interface of binary bose-einstein condensates," *Phys. Rev. A*, vol. 102, p. 033320, Sep 2020.

[35] P. Engels, C. Atherton, and M. A. Hoefer, "Observation of faraday waves in a bose-einstein condensate," *Phys. Rev. Lett.*, vol. 98, p. 095301, Feb 2007.

[36] J. Smits, L. Liao, H. T. C. Stoof, and P. van der Straten, "Observation of a space-time crystal in a superfluid quantum gas," *Phys. Rev. Lett.*, vol. 121, p. 185301, 2018.

[37] J. H. V. Nguyen, M. C. Tsatsos, D. Luo, A. U. J. Lode, G. D. Telles, V. S. Bagnato, and R. G. Hulet, "Parametric excitation of a bose-einstein condensate: From faraday waves to granulation," *Phys. Rev. X*, vol. 9, p. 011052, 2019.

[38] K. Fujii, S. L. Görlitz, N. Liebster, M. Sparn, E. Kath, H. Strobel, M. K. Oberthaler, and T. Enss, "Stable-fixed-point description of square-pattern formation in driven two-dimensional bose-einstein condensates," *Phys. Rev. A*, vol. 109, p. L051301, May 2024.

[39] N. Liebster, M. Sparn, E. Kath, K. Fujii, S. L. Görlitz, T. Enss, H. Strobel, and M. K. Oberthaler, "Emergence of crystalline steady state in a driven superfluid," 2023.

[40] K. Kwon, K. Mukherjee, S. J. Huh, K. Kim, S. I. Mistakidis, D. K. Maity, P. G. Kevrekidis, S. Majumder, P. Schmelcher, and J.-y. Choi, "Spontaneous formation of star-shaped surface patterns in a driven bose-einstein condensate," *Phys. Rev. Lett.*, vol. 127, p. 113001, Sep 2021.

[41] D. Hernández-Rajkov, J. E. Padilla-Castillo, A. del Río-Lima, A. Gutiérrez-Valdés, F. J. Poveda-Cuevas, and J. A. Seman, "Faraday waves in strongly interacting superfluids," *New J. Phys.*, vol. 23, no. 10, p. 103038, 2021.

[42] F. Michael, "On a peculiar class of acoustical figures; and on certain forms assumed by groups of particles upon vibrating elastic surfaces," *Phil. Trans. R. Soc.*, 1831.

[43] A. del Río-Lima, J. A. Seman, R. Jáuregui, and F. J. Poveda-Cuevas, "Spatial and temporal periodic density patterns in driven bose-einstein condensates," *Phys. Rev. A*, vol. 110, p. 053318, Nov 2024.

[44] A. del Rio-Lima, F. J. Poveda-Cuevas, and O. Castanos, "Entanglement of a three level atom interacting with two modes field in a cavity," *Journal of Physics B: Atomic, Molecular and Optical Physics*, vol. 57, p. 185001, aug 2024.

[45] A. del Río-Lima, A. Gutiérrez-Valdés, C. Mojica-Casique, F. Ballesteros-Flores, I. A. Villanueva-Reyes, R. Colín-Rodríguez, C. A. Gardea-Flores, F. J. Poveda-Cuevas, and J. A. Seman, "Homemade open-source full-stokes polarimeter based on division of amplitude," *Appl. Opt.*, vol. 63, pp. 7177–7187, Sep 2024.

[46] De Broglie, Louis, "Recherches sur la thÃ©orie des quanta," *Ann. Phys.*, vol. 10, no. 3, pp. 22–128, 1925.

[47] Z. Yan, "General thermal wavelength and its applications," *European Journal of Physics*, vol. 21, p. 625, nov 2000.

[48] J. Pérez-Ríos, *An Introduction to Cold and Ultracold Chemistry: Atoms, Molecules, Ions and Rydbergs*. Cham: Springer, 2020.

[49] C. Pethick and H. Smith, *Bose-Einstein condensation in dilute gases*. Cambridge University Press, 2002.

[50] P. Pieri and G. C. Strinati, "Derivation of the gross-pitaevskii equation for condensed bosons from the bogoliubov–de gennes equations for superfluid fermions," *Phys. Rev. Lett.*, vol. 91, p. 030401, Jul 2003.

[51] S. Simonucci and G. C. Strinati, "Equation for the superfluid gap obtained by coarse graining the bogoliubov–de gennes equations throughout the bcs-bec crossover," *Phys. Rev. B*, vol. 89, p. 054511, Feb 2014.

[52] D. S. Petrov, C. Salomon, and G. V. Shlyapnikov, "Weakly bound dimers of fermionic atoms," *Phys. Rev. Lett.*, vol. 93, p. 090404, Aug 2004.

[53] H. Feshbach, "A unified theory of nuclear reactions. ii," *Annals of Physics*, vol. 19, no. 2, pp. 287–313, 1962.

[54] C. Chin, R. Grimm, P. Julienne, and E. Tiesinga, "Feshbach resonances in ultracold gases," *Rev. Mod. Phys.*, vol. 82, pp. 1225–1286, Apr 2010.

[55] H. T. C. Stoof, K. B. Gubbels, and D. B. M. Dickerscheid, *Ultracold Quantum Fields*. Theoretical and Mathematical Physics, Berlin, Germany: Springer, 2009.

[56] W. Ketterle and M. W. Zwierlein, "Making, probing and understanding ultracold fermi gases," *Riv. Nuovo Cimento*, vol. 31, no. 5, pp. 247–422, 2008.

[57] S. Stringari, "Collective excitations of a trapped bose-condensed gas," *Phys. Rev. Lett.*, vol. 77, pp. 2360–2363, Sep 1996.

[58] R. P. Teles, V. S. Bagnato, and F. E. A. dos Santos, "Coupling vortex dynamics with collective excitations in bose-einstein condensates," *Phys. Rev. A*, vol. 88, p. 053613, Nov 2013.

[59] V. M. Pérez-García, H. Michinel, J. I. Cirac, M. Lewenstein, and P. Zoller, "Dynamics of bose-einstein condensates: Variational solutions of the gross-pitaevskii equations," *Phys. Rev. A*, vol. 56, pp. 1424–1432, Aug 1997.

[60] R. Grimm, M. WeidemÃŒller, and Y. B. Ovchinnikov, *Optical Dipole Traps for Neutral Atoms*, vol. 42 of *Advances In Atomic, Molecular, and Optical Physics*. Academic Press, 2000.

[61] A. I. Nicolin and M. C. Raportaru, "Faraday waves in high-density cigar-shaped bose-einstein condensates," *Physica A*, vol. 389, no. 21, pp. 4663–4667, 2010.

[62] U. Toniolo, B. C. Mulkerin, X.-J. Liu, and H. Hu, "Breathing-mode frequency of a strongly interacting fermi gas across the two- to three-dimensional crossover," *Phys. Rev. A*, vol. 97, p. 063622, Jun 2018.

[63] B. Jackson and E. Zaremba, "Quadrupole collective modes in trapped finite temperature bose-einstein condensates," *Phys. Rev. Lett.*, vol. 88, p. 180402, Apr 2002.

[64] V. M. Pérez-García, H. Michinel, J. I. Cirac, M. Lewenstein, and P. Zoller, "Low energy excitations of a bose-einstein condensate: A time-dependent variational analysis," *Phys. Rev. Lett.*, vol. 77, pp. 5320–5323, Dec 1996.

[65] M. L. Chiofalo, S. Succi, and M. P. Tosi, "Ground state of trapped interacting bose-einstein condensates by an explicit imaginary-time algorithm," *Phys. Rev. E*, vol. 62, pp. 7438–7444, Nov 2000.

[66] W. Bao, S. Jin, and P. A. Markowich, "Numerical study of time-splitting spectral discretizations of nonlinear schrödinger equations in the semiclassical regimes," *SIAM J. Sci. Comput.*, vol. 25, no. 1, pp. 27–64, 2003.

[67] W. Bao, D. Jaksch, and P. A. Markowich, "Numerical solution of the gross–pitaevskii equation for bose–einstein condensation," *J. Comput. Phys.*, vol. 187, no. 1, pp. 318–342, 2003.

[68] A. M. Kamchatnov, "Expansion of bose-einstein condensates confined in quasi-one-dimensional or quasi-two-dimensional traps," *Journal of Experimental and Theoretical Physics*, vol. 98, p. 908, May 2004.

[69] P. Capuzzi and P. Vignolo, "Faraday waves in elongated superfluid fermionic clouds," *Phys. Rev. A*, vol. 78, p. 043613, Oct 2008.

[70] N. Shukuno, Y. Sano, and M. Tsubota, "Faraday waves in bose–einstein condensates - the excitation by the modulation of the interaction and the potential," *J. Phys. Soc. Jpn.*, vol. 92, p. 064602, jun 2023.